Pore-scale studies of CO_2-hydrate sealing mechanisms - effect of salinity

Alicia Eigeland Bang

Master's Thesis in Energy

Integrated Master's Program in Energy at Geophysical Institute

Specialization in Chemical Energy Solutions

Supervised by Prof. Geir Ersland and Prof. Tanja Barth

Department of Chemistry

University of Bergen

August 2023

Abstract

Despite the growth of renewable energy production, the largest increase in emissions is attributed to CO_2 from fossil fuels and industry. The implementation of Carbon Capture and Storage can remove 90-99% of both energy and process-related CO_2 emissions. A proposed concept involves storing CO_2 in the form of gas hydrates in shallow geological formations, enhancing storage capacity and mobility control, while reducing CO_2 leakage risks by serving as an artificial cap rock below the gas hydrate stability zone (GHSZ). However, the knowledge of formation mechanisms and kinetics of CO_2 hydrates in porous media is limited. The primary objective of this work was to investigate the effect of water and brine chemistry on the formation mechanisms of CO_2 hydrates in porous media.

In this thesis, CO_2 hydrates were visually investigated using a high-pressure micromodel based on the pore network of Berea sandstone. A total of nineteen hydrate formation experiments were conducted, seven of which utilized deionized water at different temperatures to study the effect of initial water saturation and temperature on hydrate formation. Additionally, twelve experiments were performed with varying concentrations of NaCl (1-5wt%) and $CaCl_2$ (1-5wt%) under constant pressure and temperature conditions (75 bar and 3.5 °C, respectively) to investigate the effect of salinity on hydrate formation and growth mechanisms.

The hydrate formation resulted in two different hydrate configurations: hydrate films with encapsulated CO_2 and crystalline hydrate with complete CO_2 consumption. Hydrate film formation initiated at the water-CO_2 interface along the pore walls and the interface of large water droplets residing underneath the continuous CO_2 phase. The hydrate film propagation into the continuous CO_2 phase was rapid and no hydrate front was observed. Initial water saturations above 0.33 resulted in pore-filling hydrate film and, over time, a stable crystalline hydrate configuration. Crystalline hydrate initially only formed in the water phase and massive crystalline hydrate growth was achieved for $S_W > 0.4$. The growth of crystalline hydrates was further affected by salinity, with low salt concentrations promoting faster growth and shorter induction times, while higher salt concentrations resulted in a more pronounced hydrate front and longer induction times. The correlation between salinity and crystalline hydrate growth was more evident for $CaCl_2$ brine, which exhibited larger variations in hydrate saturation compared to NaCl brine.

Initial water saturation and salinity are crucial variables in predicting hydrate composition and assessing hydrate seal integrity. However, due to multiple variables and limited data, further investigations are necessary for a comprehensive understanding of CO_2 hydrate formation in porous media.

Acknowledgments

I would like to extend my heartfelt gratitude to all those who have supported and motivated me during my pursuit of the Integrated Master's Degree in Energy over the last five years. Without their unwavering support, this work would not have been possible.

First and foremost, I want to thank my supervisors Professor Geir Ersland and Professor Tanja Barth, for their invaluable guidance, support and dedication throughout this process. Their insightful feedback and expertise have played a crucial role in shaping this thesis, and I am especially grateful for the opportunity to work independently on such an interesting topic. I would also like to thank PhD candidate Maksim Lysyy for his guidance in the laboratory, introduction to image processing software, and valuable advice. My sincere appreciation goes to Dr. Na Liu for her expertise and willingness to address my questions. A special thanks to the Reservoir Physics group at the Institute for Physics and Technology for providing a supportive and resourceful environment.

To my fellow students in the Integrated Master's Program in Energy, I am grateful for the memories and the incredible journey we have shared together. A special thanks to my friends in Sal 526, Kelly N. Nguyen and Marte B. Nåmdal, for their constant support, encouragement, and enjoyable company during the completion of this thesis.

Lastly, I would like to thank my boyfriend, Sander, for making this process easier with his endless encouragement, positive outlook, and unwavering belief in me. I am forever grateful for his presence in my life.

Alicia Eigeland Bang
Bergen, August 2023

Nomenclature

A_i	Area of the particular fluid (i)	$[\mu m^2]$
A_{tot}	Total area	$[\mu m^2]$
A_v	Area of void space	$[\mu m^2]$
C	Concentration	wt%
ΔG_{crit}	Critical excess free energy	[J]
$\Delta G'_{crit}$	Critical excess free energy for heterogeneous nucleation	[J]
ΔG_S	Surface excess free energy	[J]
ΔG_V	Volume excess free energy	[J]
Δg^{exp}	Total molar change in Gibbs free energy of hydrate formation	[J/mol]
$\Delta g^{\text{product}}$	Molar change in Gibbs free energy for products (hydrate)	[J/mol]
$\Delta g^{\text{reactant}}$	Molar change in Gibbs free energy for reactants (gas and water)	[J/mol]
Δg_v	Free energy change per unit volume	[J/mol]
ΔG	Gibbs free energy	[J]
N_i	Number of pixels of the particular phase (i)	-
N_t	Total number of pixels	-
N_v	Number of pixels of the void space	-
p	Pressure	[bar]
ϕ	Fraction related to $\Delta G'_{crit}$ and ΔG_{crit}	-
ϕ_p	Porosity	[fraction]
r	Particle radius	[m]
r_c	Radius of the critical nulcei	[m]
S_i	Saturation of respective fluid (i)	[fraction]
σ_{hs}	Surface tension between the hydrate phase and the solid surface	$[\text{J/m}^2]$
σ_{ws}	Surface tension between the water phase and the solid surface	$[\text{J/m}^2]$
σ_{hw}	Surface tension between the hydrate phase and the water phase	$[\text{J/m}^2]$
T	Temperature	[°C]
t	Time	[s]
θ	Contact angle	[dregrees]

Abbreviations

CCS	Carbon Capture and Storage
$CCUS$	Carbon Capture, Utilization, and Storage
$CaCl_2$	Calcium Chloride
CH_4	Methane
CO_2	Carbon dioxide
DAC	Direct Air Capture
$DRIE$	Deep reactive Ionic etching
GHG	Greenhouse gas
$GHSZ$	Gas hydrate stability zone
GtC	Gigatonne carbon
HEN	Heterogeneous nucleation
H	Crystalline hydrate
HF	Hydrate film
HON	Homogeneous nucleation
$IPCC$	The Intergovernmental Panel on Climate Change
$IMPs$	Illustrative Mitigation Pathways
L	Liquid CO_2
N_2O	Nitrous oxide
NaCl	Sodium chloride
SDG	Sustainable development goals
SO_2	Sulfur dioxide
STP	Standard temperature and pressure
sH	Structure H
sI	Structure I
sII	Structure II
tCO_2-eq	Tonne carbon dioxide equivalent
TWh	Terawatt hour
$WGIII$	Working Group III
W	Aqueous water/brine phase
$wt\%$	Weight percent
$2D$	Two dimensional
$frac.$	fraction

Contents

1. Introduction

1.1 Background

In 2021 the global mean temperature reached 1.12°C above preindustrial levels and is projected to reach 1.50°C within the next 20 years [1]. This temperature increase is primarily due to anthropogenic emissions, making climate change one of the most pressing issues facing humanity today. As a result, implementation of measures to mitigate climate change and its impacts has become increasingly important. The Paris Agreement (2015) [2], is a legally binding treaty aiming to reduce greenhouse gas (GHG) emissions and limit the global temperature rise to 2°C above pre-industrial levels [3]. The main GHG emissions that result from human activity are carbon dioxide (CO_2), nitrous oxide (N_2O), and methane (CH_4). Since 1750, atmospheric CO_2 concentrations have increased by 47%, CH_4 concentrations have increased by 156% and N_2O have increased by 23% [1].

The world is currently facing both a climate and an energy crisis, as highlighted by the Working Group III (WGIII) report included in the Intergovernmental Panel on Climate Change's (IPCC) Sixth Assessment Report (AR6) [4, 5]. The report states that approximately 48% of the global population lives in countries emitting over 6 tCO_2-eq per capita, while 35% lives in countries emitting over 9 tCO_2-eq per capita. Conversely, 41% of the global population lives in countries emitting less than 3 tCO_2-eq per capita. Access to electricity and clean cooking fuels remains a challenge, particularly for those in low-emitting countries [6]. The UN's Sustainable Development Goals (SDGs) aim to end poverty, including energy poverty, while taking action to combat climate change and its impacts (SDG 13) [7]. However, energy systems are interconnected with issues such as pollution, health, energy access and security, food security, education, and economic prosperity [5]. Therefore, as developing countries prosper and their population grows, their emissions are expected to increase [5, 8].

Despite the growth of renewable energy production in recent years, the largest growth in emissions has come from CO_2 produced by fossil fuels and industry [5]. The IPCC Summary for Policy Makers report [4] acknowledges that "Most scenarios project that the supply of primary energy will continue to be dominated by fossil fuels until at least the middle of the century". This is evident in the current global energy mix (Figure 1.1), where fossil fuels still dominate (84%). Thus, until renewable energy production can be scaled up while ensuring global access to clean and safe energy, fossil fuels will continue to play a significant role in the global energy mix.

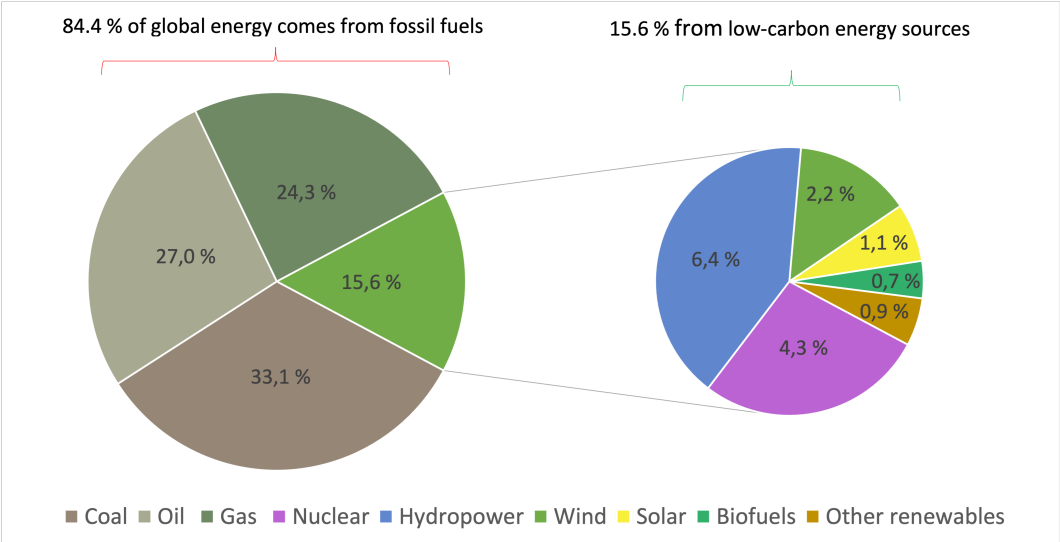

Figure 1.1: Pie charts of the global primary energy consumption by source. The data is retrieved from Our World in Data (2020) [6].

While the Paris Agreement relies on a shift towards renewable energy, the decarbonization of the energy production sector must be achieved through other means that permit the presence of fossil fuels in the global energy mix. In addition, some sectors are considered especially hard to decarbonize. Such sectors are called "hard-to-abate sectors" which include heavy industry such as steel, cement, chemical industry, and aluminum production [9]. These sectors either rely on extremely high-temperature processes that can only be achieved by burning fossil fuels, or processes that produce emissions. As a result, even if the energy sector is decarbonized, hard-to-abate sectors are still responsible for 33% of the global emissions.

Industrial Carbon Capture and Storage (CCS) can remove 90-99% of both energy and process related CO_2 emissions [9]. The role of CCS in achieving the objectives outlined in the Paris Agreement is crucial according to in the WGIII report. The report presents seven pathways (scenarios) to explore various strategies for mitigating climate change (Figure 1.2). The IMPs analyze different strategies to achieve the climate goals and almost all scenarios are based on a strong reduction of fossil fuels and considerable implementation of CCS. Only one pathway does not include CCS (IMP-LD) but this scenario requires a 50% reduction in global primary energy consumption by 2050. Given the increasing energy demand due to the electrification across multiple sectors and communities, and the growth of the world's population, a decrease in global energy demand is unlikely. The report makes it clear that CCS is a vital part of the decarbonization strategy to reach the climate goals of the Paris Agreement.

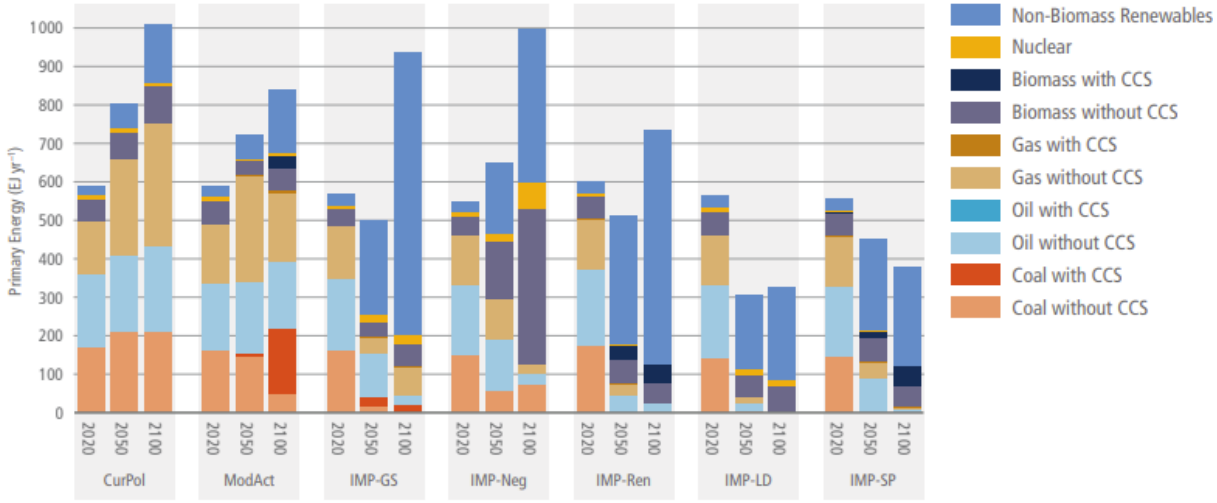

Figure 1.2: Bar chart of the hypothetical primary energy mix of the five illustrative pathways (IMPs) and the reference pathways (CurPol and ModAct) [1].

1.2 Motivation

CCUS stands for Carbon Capture, Utilization, and Storage and refers to the removal and disposal or utilization of anthropogenic CO_2 to prevent the gas from reaching the atmosphere. CO_2 can be captured either from an emission source, such as industrial plants, or directly from the atmosphere, which is called direct air capture (DAC). The captured carbon can either be stored for a geologically significant amount of time, or utilized in chemical and industrial processes [10]. The focus of this thesis is the potential of utilizing CO_2 clathrate gas hydrate, hereby denoted CO_2 hydrate, as a sealing mechanism for CO_2-storage and therefore a review of carbon capture will not be included.

Geological sequestration of carbon dioxide is the process of storing CO_2 deep underground in sedimentary formations. The geological formations must meet certain criteria, such as having sufficient porosity and permeability, and an impermeable cap rock to prevent leakage. Various storage sites have been proposed, including depleted hydrocarbon reservoirs, saline aquifers, coal beds, enhanced oil recovery by oil displacement, and salt caverns [11]. Among these, deep saline formations are the most widely used storage site. However, depleted oil or gas reservoirs are considered an attractive alternative due to the presence of an impermeable cap rock and pre-existing wells, facilities, and infrastructure [12]. Upon sequestration, liquid CO_2 is subjected to high temperature and pressure conditions (above 31.1 °C and 73.8 bar), to ensure a supercritical state, and injected into the reservoir where it is retained in the sediments by physiochemical processes. These processes include structural trapping, fluid

dissolution, capillary trapping, and mineral trapping. Structural and capillary trapping occur during the initial stages of injection and is related to the physical properties of the rock, while dissolution and mineral trapping occur over time as CO_2 reacts with the reservoir fluids and minerals.

CCS is an established technology but there are some potential risks such as public acceptance, induced seismisity and earthquakes, and leakage of CO_2 from the reservoirs through undetected faults, fractures, or leaking wells. However, the formation of a solid CO_2-hydrate layer above the storage site could reduce the risk of leakage by functioning as an additional trapping mechanism [13]. Because the agglomeration of hydrates within the pore space reduces permeability and blocks fluid flow, the layer would serve as an artificial cap rock preventing upward migration of CO_2 at the base of the gas hydrate stability zone (GHSZ) [14]. The GHSZ is found in the upper layer of the sediments (0.5 km for offshore Europe), where both the temperature and pressure is lower compared to deep saline aquifers and hydrocarbon reservoirs. The cooler storage conditions could enhance CO_2 storage capacity due to increased CO_2 density, mobility control, and CO_2 solubility in water compared to storage of supercritical CO_2 in deep formations [15]. Furthermore, CO_2 is usually transported in a liquid state and can therefore be injected without additional heating, meaning less energy is required as opposed to conventional deep formation sequestration of supercritical CO_2. Moreover, a self-sealing CO_2 hydrate layer could facilitate storage in sites without geological traps and caprocks [16]. The increased stability and safety of CO_2 storage by using hydrate technology could also improve the public acceptance.

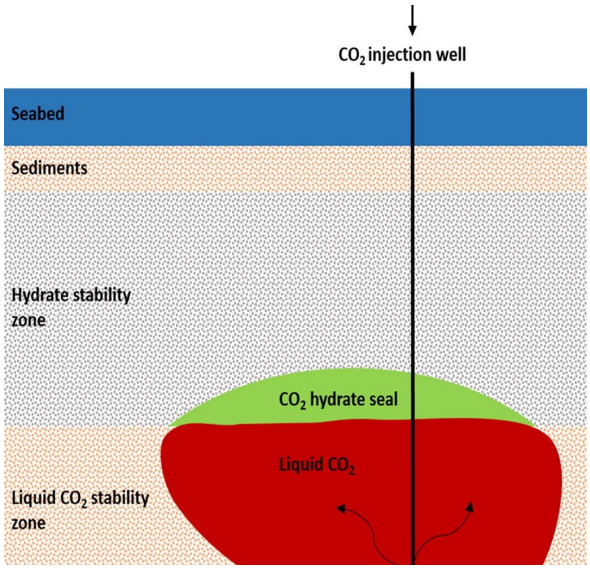

Figure 1.3: Illustration of storage of liquid CO_2 utilizing CO_2 hydrate as a sealing mechanism, from Gauteplass et al. [16].

1.3 Objectives and scope of work

The overall objective of this thesis is to investigate the formation mechanisms of CO_2-hydrates in porous media and the potential of utilizing CO_2 hydrates as a sealing mechanism for geological CO_2 storage. More specifically, this study will investigate:

- CO_2 Hydrate formation mechanisms in porous media. Hydrate growth pattern, formation kinetics, and sealing properties for each experiment are mapped by direct pore-level visualization of CO_2 hydrate formation at reservoir conditions.
- The effect of initial water saturation and temperature on hydrate formation by performing seven micromodel experiments with deionized water at varying temperatures under constant pressure (75 bar).
- The effect of salinity on hydrate formation by performing twelve micromodel experiments with brine at different salinities. Two different salts, sodium chloride (NaCl), and calcium chloride ($CaCl_2$) are used for this purpose. Six experiments are conducted for each salt, with salinities ranging from 1wt%-5wt%. The experiments are carried out at constant pressure and temperature (75 bar and 3.5 °C) to replicate the conditions within the hydrate stability zone.

A high-pressure silicon micromodel resembling the pore network in Berea sandstone is used in this work. The micromodel is connected to a pump system consisting of two pump cylinders filled with a distinct fluid (brine/water and liquid CO_2), with the pressure of the system and the volume of the fluids maintained and recorded using Quizix PumpWorks program. A dual cooling chamber ensures a constant temperature within the hydrate stability zone. The system is saturated with water or brine, and liquid CO_2 is injected. The formation of CO_2-gas hydrates from liquid CO_2 and water/brine at different salinities is visually investigated using a microscope connected to a camera illuminated by a light source. Hydrate growth mechanisms and saturations is estimated through both qualitative and quantitative characterization of the images. The quantitative characterization of the images is estimated using the visualization software, ImageJ.

2. Theory

This chapter provides an overview of the fundamental properties of gas hydrates, focusing on CO_2 hydrates. Section 2.1 provides a general overview of the properties of CO_2 for a better understanding of the following sections. Sections 2.2-2.6 introduce the gas hydrate phenomenon, the history of gas hydrate research, the different hydrate structures, hydrate formation and dissociation mechanisms, and the effect of salt on hydrate formation.

2.1 CO_2 Properties

Carbon (C) is the primary constituent of all organic matter and the carbon cycle, a process which transfers carbon between plants, microbes, animals, minerals, and the atmosphere. Carbon dioxide (CO_2) is a vital component of the Earth's atmosphere, playing a significant role in the carbon cycle and regulating the planet's temperature. Carbon dioxide gas (CO_2) is produced by combustion or decay of organic materials, fermentation, and respiration in animals. Photosynthetic organisms absorb CO_2 from the air and convert it into carbohydrates and oxygen. Vast amounts of carbon has accumulated in the Earth's crust as fossil fuels such as oil, gas and coal. Burning these fuels converts the otherwise stored carbon into gaseous CO_2, which is then released into the atmosphere. CO_2 in the atmosphere absorbs infrared radiation, contributing to the greenhouse effect and global warming. Figure 2.1 is a simplified illustration of the transfer of carbon between the biosphere and the atmosphere.

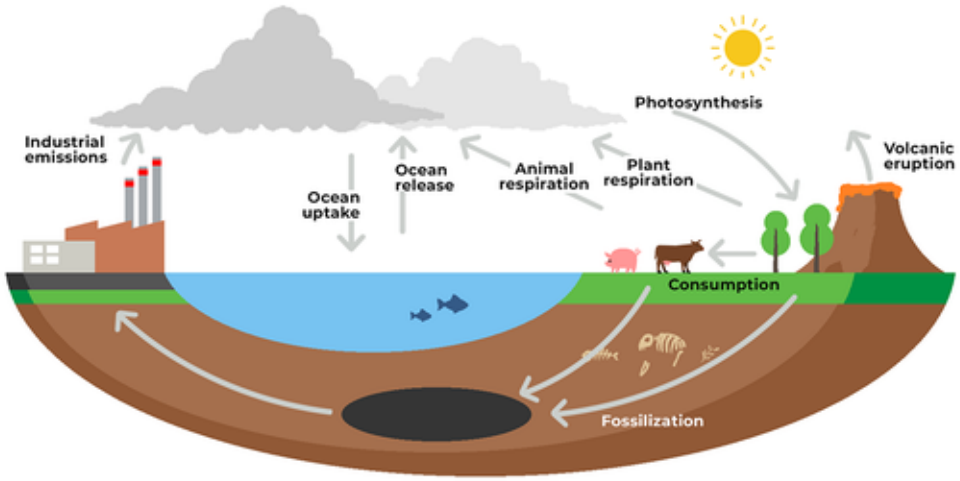

Figure 2.1: Diagram of the carbon cycle with arrows showing the flow of carbon between the biosphere and the atmosphere [17].

CO_2 is a chemical compound where the carbon is attached to two oxygen atom by a covalent double bond as shown in Figure 2.2. The molecule is linear and has no electric dipole moment, making it a non-polar molecule with polar bonds. Because of the difference in the electronegativity of the oxygen (3.44) and carbon (2.55), the molecule has a partial negative (δ^-) charge on the oxygen atoms and a partial positive charge (δ^+) on the hydrogen atoms. The partial charges enable the molecule to interact with other polar molecules such as water, making it soluble in water.

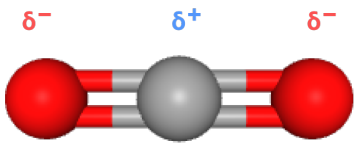

Figure 2.2: Chemical model of CO_2 with the molecular partial charges. Oxygen is illustrated by the red spheres and carbon by the gray spheres. The negative partial charge is denoted δ^- and the positive partial charge is denoted δ^+.

The solubility of CO_2 in water is affected by various factors, such as temperature, pressure, and salinity. The solubility in aqueous solution increases with increasing pressure and decreasing temperature. The solubility also decreases with increasing salinity, expressed by the following equation [18]:

$$w_{CO_2,b} = w_{CO_2,w} \cdot (1.0 - 4893 \cdot 10^{-2} \cdot S + 0.1303 \cdot 10^{-2} \cdot S^{-2} - 0.1871 \cdot 10^{-4} \cdot S^3) \quad (2.1)$$

Where $w_{CO_2,w}$ and $w_{CO_2,b}$ is the solubility of CO_2 in water and brine, respectively. S is the salinity of the water (wt%).

CO_2 is a gaseous phase at ambient conditions but can exist as a solid, liquid, or supercritical fluid depending on the pressure and temperature, represented by Figure 2.3. Supercritical conditions refer to the state where gas cannot be separated from the liquid, thus the fluid possesses properties from both states. During conventional CCS, carbon dioxide is sequestered in a supercritical phase, as opposed to sequestration within the GHSZ where CO_2 is in a liquid phase.

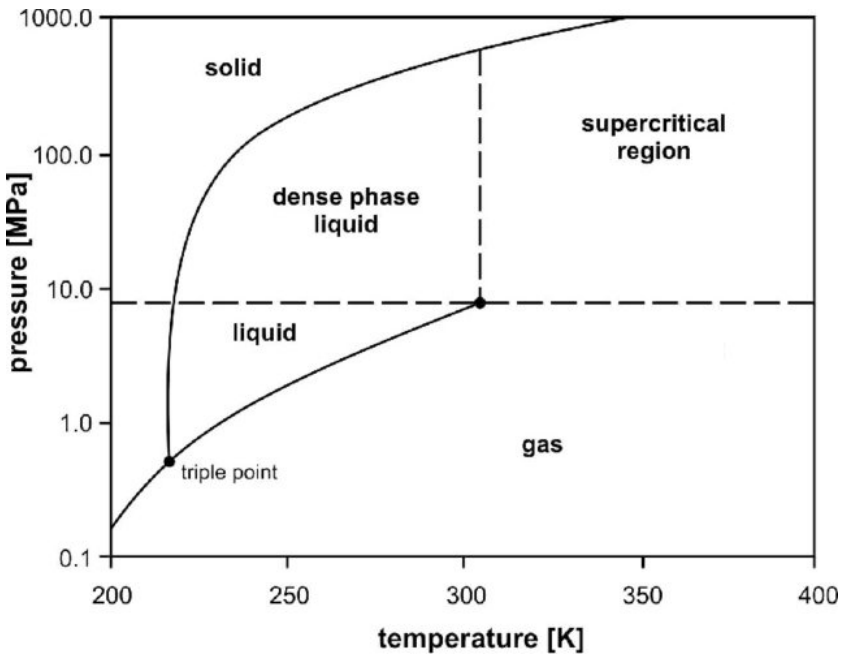

Figure 2.3: CO_2 phase diagram showing the temperature in Kelvin and pressure in MPa at which carbon dioxide is in a solid, liquid, gasous, and supercritical phase. Phase diagram modified from Witkowski et al. [19].

2.2 Clathrate hydrates

Gas hydrates are crystalline solid compounds composed of gas molecules ("guest") trapped inside the cavities of hydrogen-bonded water molecules ("host"). The small guest molecules are in a gaseous state at ambient conditions which is why these compounds are called gas hydrates. The structure is stabilized by attractive van der Waals forces between the encaged gas molecules and the surrounding water molecules. The percentage of occupied cages may vary, depending on the pressure, temperature and availability of gases. Consequently, gas hydrates do not have a fixed composition and are so-called non-stoichiometric compounds. Clathrate hydrates only form under favorable conditions, that is, moderate to high pressures and low temperatures. In nature, microbial CH_4 (methane produced by bacteria) may be readily available in sediments. Therefore, natural gas hydrates can be found in abundance in ocean sediment floors and in permafrost regions where the conditions are favorable for hydrate thermodynamic stability. The extensive availability of CH_4 gas hydrates in nature implies a potential of utilizing CO_2 gas hydrates as a means for storage and sequestration of carbon dioxide.

The conditions for gas hydrate stability can be illustrated by the hydrate phase curve which shows the gas hydrate stability zone (GHSZ) where we have the hydrate phase. The hydrate stability zone is dependent on the geothermal gradient in the sediments and is normally larger for permafrost regions than in marine sediments. To successfully retain CO_2 and prevent leakage, a thick GHSZ is critical. The CO_2-GHSZ thickness for offshore Western Europe is estimated to 0.5 km of the upper sediments, demonstrating immense potential for storing liquid CO_2 [20]. Figure 2.4 shows the CO_2-hydrate stability conditions for for two geological formations: marine sediments (Figure 2.4a) and permafrost regions (Figure 2.4b). The GHSZ lies below the equilibrium line (blue) and the geothermal gradient line (dotted red). The equilibrium line is also referred to as the phase boundary curve, above which no hydrate will form.

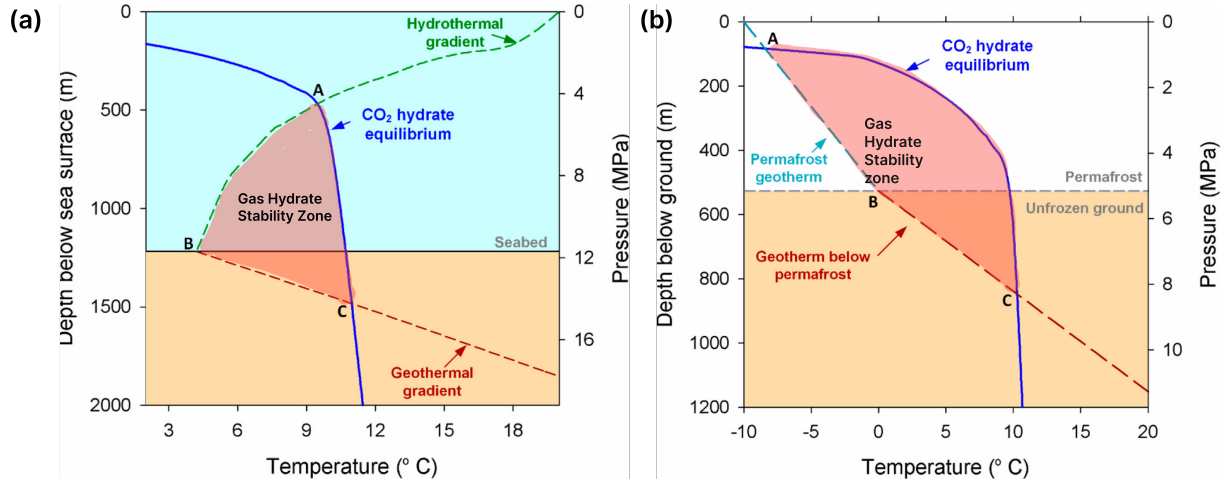

Figure 2.4: CO_2 hydrate stability zone for (a) Marine sediments and (b) Permafrost regions. The blue line represents the equilibrium line, and the green and red dashed lines are the hydrothermal gradient and the geothermal gradient, respectively. The red area between the thermal gradients and the equilibrium lines is the hydrate stability zone. The figures are modified from Zheng et al. [21].

2.3 Historical Overview

In 1810 Sir Humphrey Davy discovered, through a series of experiments, that what he believed to be solid chlorine contained water [22]. This discovery is recognized as the first scientific observation of hydrates [23]. In the following years, quantitative descriptions of inorganic hydrates and direct measurements of their composition became the main objective of hydrate research, until 1888 when Villard discovered the existence of organic gas hydrates [24]. The 1930s marks the beginning of the modern hydrate research era for hydrate research, which up until 1934 had been driven by scientific curiosity [23]. In 1934, Hammerschmidt discovered hydrate plugs in gas transmission pipelines at temperatures above freezing point [25]. This discovery shifted the focus of hydrate research toward thermodynamic properties, particularly the effects of temperature and pressure on the formation of hydrates in pipelines and the development of hydrate formation inhibitors. The effect of inhibitors was investigated by several researchers, and chloride salts, methanol, and monoethylene glycol were considered, with methanol being one of the most favored inhibitors [23].

In the late 1940s and early 1950s, von Stackelberg and coworkers summarized and interpreted two decades of x-ray hydrate crystal diffraction data which led to the discovery of two different hydrate crystal forms, structures I (sI) and II (sII) [23]. From 1959 to 1967, Jeffrey and coworkers performed a series of crystallographic studies on sI and sII hydrates. The studies showed that hydrates are members of a class of compounds called "clathrates" [26]. The third hydrate structure, structure H, was discovered by Ripmeester et al in 1987 [27]. Although a few other clathrate hydrate structures have been identified, these three structures are the most common. The discovery of hydrate structures allowed for more accurate methods of predicting hydrate thermodynamic properties. In 1959, Van der Waals and Pletteeuw proposed a statistical theory to predict thermodynamic properties such as temperature and pressure, from intermolecular potentials. This method is the foundation of the thermodynamic method used today [23].

The existence of natural gas hydrate deposits and the idea about the potential of natural gas hydrates as an unconventional energy source was formulated in the 1960s by the Soviet scientist Makogon [28, 29]. The first deposit was discovered in 1963 after drilling the Markhinskaya well in the permafrost region of Siberia. This discovery resulted in decades of geological research to identify the natural gas deposits around the world and the properties of these species [23]. Natural gas is the cleanest burning fossil fuel, meaning that it emits fewer air pollutants and less CO_2 compared to other fossil fuels. Natural gas is mainly methane and emits mostly CO_2 and water vapor upon burning. If used in place of coal or

oil, natural gas can help reduce global greenhouse gas emissions and improve air quality [30]. Large amounts of natural gas reside in natural gas hydrate deposits around the world, one volume of methane hydrate at 26 bar and 0°C contains 164 volumes of gas [31]. Sloan and Koh (2008) estimated the global hydrate reserves to exceed that of coal, natural gas, and oil reserves combined, with an estimate of 10 000 GtC [32]. Most estimates are not well defined and recent studies have shown large deviation from earlier estimations. Piñero et al. [33] estimated the global reserves to be 400-1100 GtC, orders of magnitudes lower than first estimated. However, even the lowest estimates indicate large amounts of natural gas stored.

In 1998, pilot drilling and production testing were performed in permafrost regions in the Mallik well in Canada. The international field experiment took place in 2002. The Mallik pilot proved the possibility of recovering energy from permafrost hydrates using dissociation techniques such as depressurization and thermal stimulation. More recent research has focused on an alternative methane recovery method from hydrates which combines sequestration of anthropogenic CO_2 and methane production. CO_2 is the thermodynamically preferred hydrate former and by injecting CO_2 into a natural gas reservoir, CO_2 will replace CH_4 in the hydrates and thus release methane as CO_2 is stored. The first field trial to investigate the CO_2/CH_4 exchange technique was the Ignik Sikumi #1 Field Trial in Alaska in 2012, where more than half of the injected CO_2 was sequestered [34].

Previous research have been focused on methane recovery from hydrate bearing sediments by CO_2/CH_4 exchange mechanisms and CO_2 hydrates alone have not been studied as extensively [13]. However, in recent years the concept of CO_2 sequestration within the hydrate stability zone in addition to, or as an alternative to conventional storage of supercritical CO_2 in deep formations has gained interest among researchers. The possibility of sequestering CO_2 in hydrates in shallow geological formations was first proposed in 1995 by Koide et al. [14], who suggested that the sealing of pores in sedimentary formations by CO_2-gas hydrates could function as an artificial cap rock and prevent leakage of carbon dioxide. More recent research on the subject will be presented in chapter 3.

2.4 Hydrate structure and guest molecule

Gas hydrates are crystalline compounds consisting of hydrogen bonded water molecules comprising cavities capable of encapsulating gas molecules. At STP these complexes can accommodate up to 164 volumes of gas in one volume of hydrate [31]. Typical gas hydrate formers are methane, ethane, propane, and carbon dioxide, although over 130 compounds are known to form clathrate hydrates with water molecules. Most of these compounds form hydrates of cubic structures I and II (sI, sII), or hexagonal structure H (sH), and they can be distinguished by the composition of their cavities as shown in Figure 2.5. The formation of these structures require the presence of the hydrate former due to the stabilizing Van der Waals forces between the guest molecule and the cavities. This is because repulsive forces between the water molecules and the guest molecules in either neighboring cavities or the cavity itself prevent strain and breakage of the hydrogen bonds [23]. Thus, the structure and stability of the lattice cavities (sI, sII, or sH) are dependent on the size and shape of the guest molecule. While there have been reports of other gas hydrate structures, they are very rare and will not be included in this thesis.

All hydrate structures are composed of five hydrogen-bonded water molecules forming a polyhedra. The nomenclature description of the polyhedra is n_i^{mi}, where n_i is the number of edges (water molecules) and m_i is the number of faces with n_i edges, the simplest being the 5^{12} cavity is composed of twelve pentagonal faces ($n_i = 5$ and $m_i = 12$) where all bond-lengths and angles between the water molecules are equal [23].

2.4.1 Structure I

Structure I (sI) is the smallest of the three structures (12 Å) and predominates in nature. One unit cell of sI gas hydrate consists of 46 water molecules making up a primitive cubic lattice. The structure consists of two small almost spherical cavities with twelve pentagonal faces (5^{12}, pentagonal dodecahedron) and six large nonspherical cavities with twelve pentagonal and two hexagonal faces ($5^{12}6^2$, tetrakaidecahedron). The average radius of the small cavities is 3.95 Å making them perfectly fitted for small guest molecules such as methane. Carbon dioxide typically forms hydrates of sI and is capable of stabilizing both 5^{12} and $5^{12}6^2$ cages but prefer the large cavities, with an average radius of 4.33 Å, making them able to accommodate both smaller molecules such as methane and larger molecules. Therefore, CO_2 will not occupy all eight cavities, but rather occupy the small and large cavities in a ratio of 1:3 [35].

2.4.2 Structure II

Structure II (sII) is composed of 136 water molecules making up a cubic structure of 17.3 Å. The structure is made up of 16 small cavities with twelve pentagonal faces (5^{12}) with an average radius of 3.91 Å, able to accommodate small guest molecules such as oxygen, nitrogen and methane. Eight large almost spherical cavities with twelve pentagonal and four hexagonal faces ($5^{12}6^4$) with an average radius of 4.73 Å, can be filled by larger molecules such as propane or iso-butane.

In cubic structures I and II, small molecules can occupy both the small and the large cavities, thereby stabilizing the lattice. Large molecules however, stabilize the lattice by occupying the large cavities, leaving the small cavities empty.

2.4.3 Structure H

Structure H (sH) is composed of 34 water molecules making up a hexagonal system with two lattice parameters, a=12.2 Å and c=10.1 Å. One unit cell of sH is made up of three small pentagonal dodecahedra cavities (5^{12}) of 3.94 Å, two medium cavities (4.04 Å) with three square faces, six pentagonal faces and three hexagonal faces ($4^3 5^6 6^3$), and one large cavity (5.79 Å) of twelve pentagonal faces and eight hexagonal faces ($5^{12}6^8$).

To stabilize sH both large, medium and small cavities must be occupied by molecules of the appropriate size. Therefore gas mixtures of both small and large molecules could potentially form gas hydrates of structure sH.

Table 2.1: Geometries of one unit cell of hydrate structures I, II, and H.

Hydrate structure	I		II		H		
Cavity	Small	Large	Small	Large	Small	Medium	Large
Description	5^{12}	$5^{12}6^2$	5^{12}	$5^{12}6^4$	5^{12}	$4^3 5^6 6^3$	$5^{12}6^8$
Number of cavities	2	6	16	8	3	2	1
Average cavity radius (Å)	3.95	4.33	3.91	4.73	3.91	4.06	5.71
Coordination number	20	24	20	28	20	20	36
Water per unit cell	46		136		34		

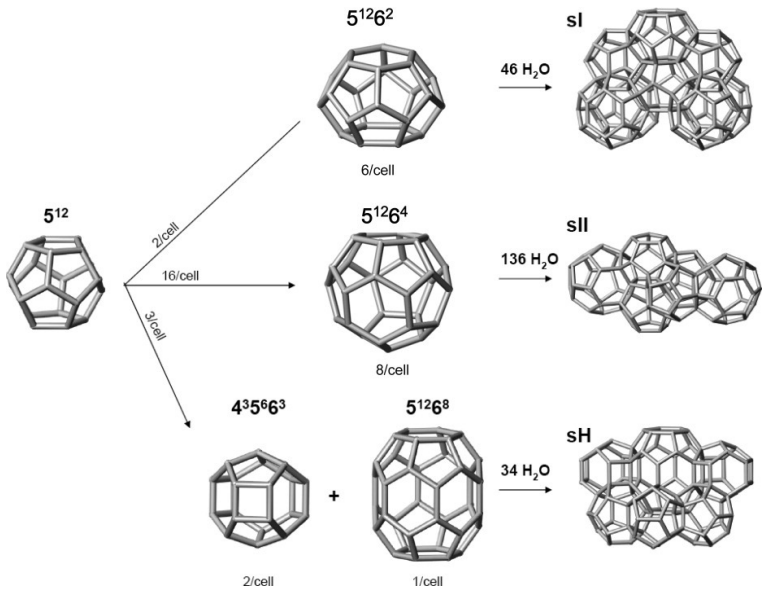

Figure 2.5: Gas hydrate cavities and structures sI, sII and sH. From Sloan et al. [36].

2.5 Hydrate formation and dissociation

Hydrate formation occurs when both hydrate former (gas) and water is readily available, under thermodynamic favorable conditions (within the GHSZ). Hydrate formation is a time-dependent phenomena which can be divided into two stages: (1) nucleation and (2) growth. Hydrate dissociation is also time-dependent and will occur when the thermodynamic conditions are outside the GHSZ, or when introduced to an inhibitor. In the following sections, hydrate nucleation, growth, and dissociation will be described, as well as hydrate formation inhibitors.

2.5.1 Hydrate nucleation

Hydrate nucleation is a time-dependent stochastic process where the reacting system is defined as random collisions of molecules. The hydrate nuclei, defined as small clusters of water and gas, will grow and disperse until a critical size is achieved. The critical cluster size is the size that must be reached before the nuclei can grow spontaneously. The nucleation is a microscopic phenomenon, which makes it difficult to observe experimentally [23]. Hydrate nucleation can be divided into homogeneous nucleation (HON) and heterogeneous nucleation (HEN).

Homogeneous nucleation (HON)

Homogeneous nucleation assumes the absence of particles or solid phases such as surfaces, therefore, HON rarely occurs in nature. However, homogeneous nucleation is the basis of the Classical Nucleation Theory and is still relevant for modern descriptions of nucleation. Due to the thermal motion of the molecules, molecular collisions could result in the formation of clusters. These clusters might continue to grow until they reach the critical size or they might dissolve. A stable nucleus comprises several thousand molecules and the simultaneous collision of these molecules is unlikely. The more probable reaction mechanism is a sequence of bimolecular collisions resulting in a sequential formation of clusters of increasing size as illustrated in Figure 2.6 [23]. As two molecules collide they may create a cluster containing two molecules (A_2), this cluster collides with a third molecule, creating a cluster of three molecules (A_3) and so on, until the critical cluster size (A_n) is reached.

$$A + A \Longleftrightarrow A_2$$
$$A_2 + A \Longleftrightarrow A_3$$
$$A_{n-1} + A \Longleftrightarrow A_n$$

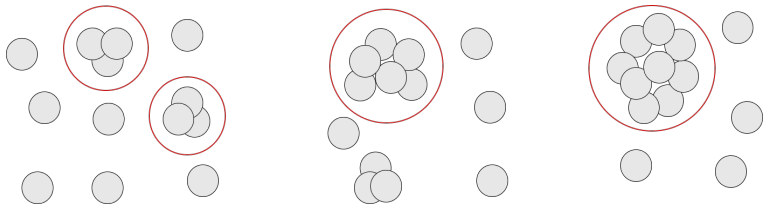

Figure 2.6: Schematic illustration of the formation of a critical nucleus.

Many cluster fail to achieve the critical size and instead dissolve due to density or composition fluctuations. This process can be explained in terms of Gibbs free energy (ΔG). Where ΔG is equal to the sum of the excess free energy of the molecules merging with the crystal nuclei (surface excess free energy, ΔG_S), and the free energy of the molecules in the bulk of the crystal nuclei (volume excess free energy, ΔG_V). Both ΔG_S and ΔG_V are functions of the radius of the solid particle, r. The relationship is described by the following equation [23]:

$$\Delta G = \Delta G_S + \Delta G_V = 4\pi r^2 \sigma + \frac{4}{3}\pi r^3 \Delta g_V \tag{2.2}$$

Where σ is the surface tension of the crystal-liquid interface and Δg_V is the free energy change per unit volume and is negative as the cluster size increases. Thus ΔG_S and ΔG_V are of opposite signs. Figure 2.7 shows the relationship between Gibbs free energy and cluster size.

The maximum Gibbs free energy, ΔG_{crit}, is an energy barrier corresponding to the critical nucleus radius, r_c, and must be overcome for the cluster to reach the critical size and grow spontaneously. By differentiating equation (2.2), the value of the critical Gibbs free energy can be obtained:

$$r_c = \frac{-2\sigma}{\Delta g_V} \tag{2.3}$$

and

$$\Delta G_{crit} = \frac{4\pi\sigma r_c^2}{3} \tag{2.4}$$

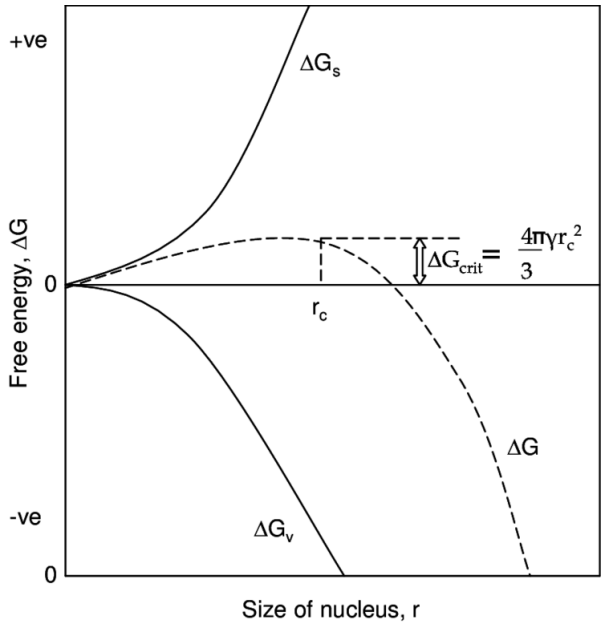

Figure 2.7: ΔG as a function of cluster size [37].

Heterogeneous nucleation HEN

Heterogeneous nucleation occurs in the presence of a solid particle or surfaces and is the most usual form of nucleation in nature. In terms of thermodynamics, it is more probable for hydrate growth to occur on a two-dimensional surface, than in a a three-dimensional surface-free volume. Heterogeneous nucleation can therefore occur at higher temperatures and at a lower critical Gibbs free energy than homogeneous nucleation. To obtain the lower critical Gibbs free energy for heterogeneous nucleation, $\Delta G'_{crit}$, the Gibbs free energy of homogeneous nucleation ΔG_{crit} is multiplied with a fraction, ϕ:

$$\Delta G'_{crit} = \phi \Delta G_{crit} \tag{2.5}$$

where ϕ is related to the contact angle, θ, between the hydrate cluster and a surface or a particle as follows:

$$\phi = \frac{[(2 + \cos\theta)(1 - \cos\theta)^2]}{4} \tag{2.6}$$

The contact angle is a measurement of the wettability, which is the wetting preference of the system and is defined as the ability of a liquid to spread on a solid surface. If the contact angle between a fluid and a solid is in the range [0°-90°], the fluid is said to be the wetting fluid, while contact angles in the range [90°-180°] means that the fluid is a non-wetting fluid. The contact angle of a hydrate-water system, where water is the wetting phase, is given by the Young-Dupree equation:

$$\frac{\sigma_{hs} - \sigma_{ws}}{\sigma_{hw}} = \theta \tag{2.7}$$

where σ is the interfacial tension between the three phases: hydrate, water, and solid/surface as shown in Figure 2.8.

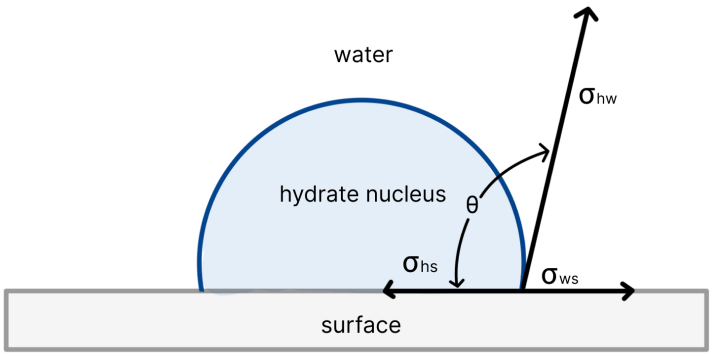

Figure 2.8: Schematic illustration of hydrate growth on a surface, the contact angle, and the surface tensions between hydrate-water σ_{hw}, hydrate-surface σ_{hs}, and water-surface σ_{ws}.

From equation 2.5 and 2.6, it follows that for complete non-wetting of the surface ($\theta = 180°$), $\Delta G'_{crit} = \Delta G_{crit}$ and for complete wetting of the surface ($\theta = 0°$), $\Delta G_{crit} = 0$. Thus, for systems with a low contact angle between the surface and the hydrate nucleus (high surface/hydrate wettability), the surface lowers the critical Gibbs free energy barrier and the critical radius of the nucleus.

In heterogeneous nucleation, the cluster can either form on the solid particle (cap-formed), or at the interface between the solution and gas phase (lens-shaped) as illustrated in Figure

2.9. However, hydrate formation usually occurs at the vapor-liquid interface because the interface lowers the Gibbs free energy barrier of nucleation and the concentrations of both host and guest molecules are high.

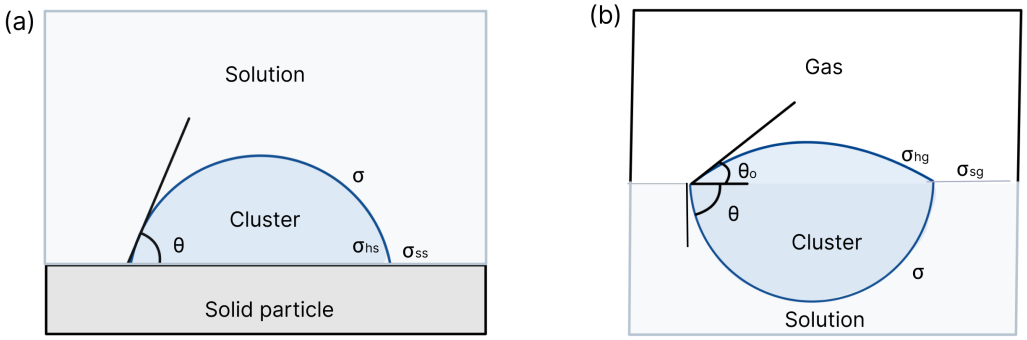

Figure 2.9: Schematic illustration of (a) a cap-shaped cluster on the solid-solution interface and (b) a lens-shaped cluster at the solution-gas interface. $\sigma_{hs}, \sigma_{ss}, \sigma_{hg}$, and σ_{sg} are the interfacial tensions between the phases.

Driving force

The driving force of the nucleation process is is an important component in describing hydrate formation. However, several driving forces have been reported in hydrate literature such as fugacity, chemical potential, supersaturation, degree of subcooling, temperature and pressure [23]. In 1995, Christiansen and Sloan derived an expression where the molar change in Gibbs free energy of hydrate formation (Δg^{exp}) accounts for all nucleation driving forces previously presented [38]. The molar change in Gibbs free energy is given as the difference between Gibbs free energy of the gas and water (reactants) and hydrate (product), expressed as:

$$\Delta g^{exp} = \Delta g^{reactant} - \Delta g^{product} \tag{2.8}$$

Induction time

The induction time is the time it takes for the crystal nuclei to form, also defined as the time elapsed until the appearance of a detectable volume of hydrate phase, or a detectable consumption of gas. Induction times are unpredictable due to their stochastic nature, particularly at low driving forces and are said to be a function of time-dependent variables such as gas consumption, surface area, agitation, history of the water, and the presence of foreign particles [23].

2.5.2 Hydrate growth

When the system energy barrier (ΔG_{crit}) is overcome and the nucleus has reached its critical size, growth will occur. During growth, the overall energy of the system will decrease and proceed toward equilibrium. The Growth period is a rapid process where gas is encapsulated in the hydrate lattice and both water and gas are consumed. Three factors influence the hydrate growth: (1) the kinetics of crystal growth at the hydrate surface, (2) the mass transfer of components to the growing crystal surface, and (3) heat transfer of the exothermic heat of hydrate formation away from the growing crystal surface [23].

Growth mechanisms

Tiller [39] identified two crystal growth mechanisms that both depend on the interfacial driving force: (1) step growth, and (2) continuous growth. Stepwise growth is a mechanism that occurs at low driving forces, where the molecules attach at step kink sites. The interface advances by lateral movement of steps. Continuous growth is a mechanism that occurs at higher driving forces, where molecules attach everywhere on the solid surface, and the growth of the solid interface is normal to itself. Figure 2.10 demonstrates the crystallography resulting from the two mechanisms. Chan et al. [40] reported that well-defined crystallographic surfaces such as single crystals indicated growth by step mechanism (Figure 2.10a). However, as the system pressure increased, a transition from step to continuous growth was observed, as shown in Figure 2.10b.

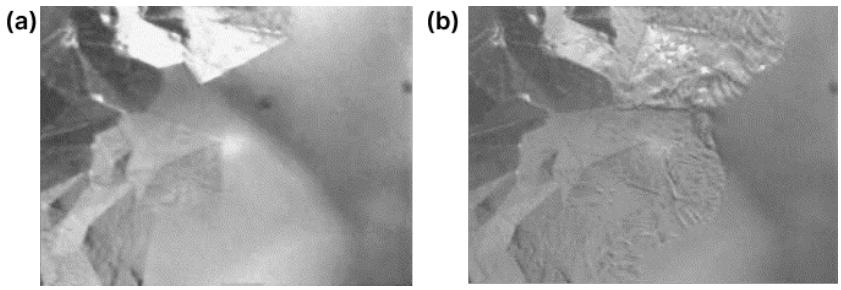

Figure 2.10: (a) Development of methane hydrate crystals at the methane-water interface. (b) The transition from step growth to continuous growth. Modified from Freer et al. [41].

Hydrate growth is typically considered an interfacial phenomenon, which occurs at the water-gas interface where the component concentrations are significantly higher compared with their mutual fluid solubilities [42]. Taylor et al. [43] conducted a series of CH_4 hydrate film formation experiments and suggested the following step-wise hydrate formation mechanism: (1) hydrate film formation, a thin porous hydrate film propagates across the interface, (2)

The hydrate film thickens and pores within the film are filled, (3) Bulk conversion of the hydrate film to solid nonporous hydrate film, all the remaining pores are filled.

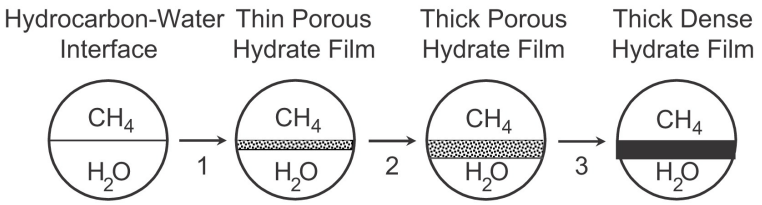

Figure 2.11: Schematic representation of the three hydrate film formation steps proposed by Taylor et al. [43].

Staykova et al. [44] suggested that during the initial formation of the hydrate film, the porous structure of the film enables efficient transport of water or gas through the hydrate layer. Water is transported through capillaries within the porous hydrate layer, while gas is transported out of the hydrate layer[45]. However, as the hydrate shell thickens and the pores within the crystalline cages are filled, mass transport across the film become the rate-determining step. During the final step, the solidification of the hydrate film at the interface restricts further mass transport through the hydrate layer [42].

Hydrate morphology

The crystal morphology refers to the geometric shape of the crystal. Several studies have found that crystal morphology is generally independent of the hydrate former [23]. There are several factors affecting crystal growth, especially important are the driving forces. Servio and Englezos [45] studied the morphology of methane and carbon dioxide hydrate crystals. They found that needle-like crystals appeared when the driving forces were high, while under low driving forces, the surface was smooth and faceted. They concluded that this difference in morphology was due to the larger number of nucleation sites under high driving forces, compared to the number of sites under lower driving forces. The nucleation for high driving forces is also faster, resulting in more random crystal growth and a rough surface. In contrast, lower driving forces result in fewer nucleation sites and slower crystal growth.

Several studies have been done on the morphology of hydrate crystals, common for most is the morphology dependence on the degree of driving forces. Figure 2.12 is taken from a hydrate bulk study conducted by Ohmura et al. [46] and shows the formation of faceted and dendritic hydrate crystals at the methane-water interface. Figure 2.13 shows the two morphologies in a synthetic porous system filled with methane and water.

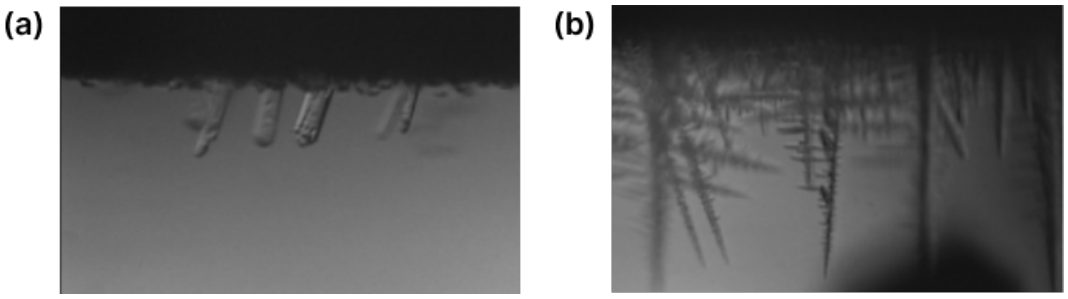

Figure 2.12: The two different morphologies from a study done by Ohmura et al. [46]. (a) Faceted/columnar crystal morphology at the CH_4-water interphase. (b) dendritic needle-like crystal morphology at the CH_4-water interphase.

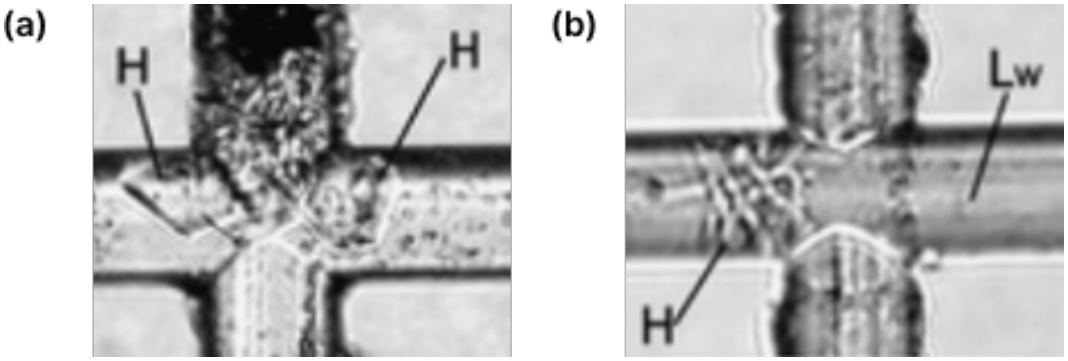

Figure 2.13: Images modified from a study conducted by Katsuki et al [47]. (a) Faceted hydrate crystals (H). (b) Dendritic crystals (H) and liquid water (L).

2.5.3 Hydrate dissociation

Hydrate dissociation is important in gas production and flow assurance in pipelines. Dissociation of solid hydrates to its constituents (hydrate former and water) is an endothermic process, meaning heat must be supplied to break the intermolecular forces between the water molecules (hydrogen bonds) and between the water molecules and the guest molecules (van der Waals forces). There are three methods for dissociating hydrates: (1) Depressurization, (2) Thermal stimulation, and (3) Inhibitor injection [23]. Depressurization is the process of reducing the pressure below the equilibrium pressure at a given temperature. Thermal stimulation involves increasing the temperature above the equilibrium temperature at a given pressure. Hydrate inhibitors are chemicals that are usually injected into pipelines to prevent the formation of hydrates, but will also promote hydrate dissociation in hydrate-bearing sediments.

2.6 The effect of salt on hydrate formation

Hydrate inhibitors are chemicals used to prevent hydrate formation, they are used in a variety of applications such as natural gas production and transportation, CCS, and other industrial processes involving gas and water under high-pressure conditions. There are two kinds of hydrate inhibitors: (1) thermodynamic inhibitors and (2) kinetic inhibitors. Thermodynamic inhibitors work by shifting the hydrate equilibrium conditions to higher pressures and lower temperatures. Thermodynamic inhibitors include alcohols and salts, with methanol and ethylene glycol being the most commonly used. Kinetic inhibitors work by slowing down the rate of formation by adsorbing on the surface of hydrate crystals, or at the gas-water interface, inhibiting the growth of hydrate crystals. Kinetic inhibitors include surfactants, polymers, and other surface tension-altering chemicals.

Water that occurs naturally within the pores of rocks in deep sea formations such as saline aquifers and depleted hydrocarbon reservoirs is called formation water. Formation water is usually a mix between fresh water and high-salinity sea water containing ions such as K^+, Na^-, Ca^{2+}, Mg^{2+}, Cl^-, SO_4^{2-}, CO_3^{2-} [48]. Salt is a thermodynamic inhibitor which inhibits hydrate formation by lowering the freezing point of water and shifting the hydrate equilibrium towards higher pressures and lower temperatures. This happens because of Coulombic forces between the dissolved salt ions and the dipoles of the water molecules. When salt ions are present, water molecules arrange themselves around the ions forming Coulombic bonds stronger than both hydrogen bonds and van der Waals forces between the water cage and guest molecules, thus inhibiting the formation of gas hydrates [23]. This inhibition effect is a colligative property, meaning that increasing salt concentrations will increase the shift of the equilibrium curve. Furthermore, the solubility of the guest molecule in water decrease with increasing salinity, this effect is known as "salting-out". For instance, CO_2 is nonpolar, when CO_2 is dissolved in water the water molecules form hydration shells around the dissolved molecule. In a aqueous solution with both salt and CO_2 the polar water molecules are more attracted to the dissolved salt ions making fewer water molecules available for dissolution of CO_2.

The size and charge of the salt ions also plays an important role in hydrate inhibition using salts [49, 50]. Smaller ions with a higher charge such as Ca^{2+} and Mg^{2+}, are more effective at inhibiting hydrate formation than larger ions with a lower charge, such as Na^{+} and K^{+}. Calcium chloride ($CaCl_2$) and sodium chloride (NaCl) are both salts commonly used as thermodynamic hydrate inhibitors. However, $CaCl_2$ is generally considered a more effective hydrate inhibitor than NaCl because it has a greater impact on the equilibrium conditions of hydrate formation [51]. Ca^{2+} is a larger ion than Na^{+}, with a greater charge density, which means it can attract more water molecules and form stronger Coulombic bonds. This results in a larger shift in the hydrate equilibrium curve towards higher pressures and lower temperatures when $CaCl_2$ is present. NaCl has a smaller ion size and charge density, which means it has a weaker effect on the equilibrium conditions. Furthermore, $CaCl_2$ has been shown to reduce the solubility of gases such as methane and carbon dioxide more than NaCl, because it causes a stronger "salting-out" effect [52]. This means that less of the gas molecule can dissolve in the water, which reduces the concentration of gas available to form hydrates.

Given a system comprised of saline water and gas, only water and gas molecules are consumed to form hydrates. As hydrates form, the concentration of salt ions in the remaining pore water will increase until the salinity of the water reaches a level where further hydrate formation is inhibited. The local increase in salinity will result in a salinity gradient between water pockets with high salt concentration and neighbouring pores. The salinity gradient will equilibrate over time due to film flow and ion diffusion in the water phase wetting the grains [53]. This is known as the desalination effect.

3. Literature Survey

This chapter provides an overview of research on CO_2 hydrate formation in in porous media and is focused on CO_2 hydrate formation in porous media and the effect of salinity on formation thermodynamics and kinetics.

3.1 CO_2 hydrate formation in micromodels

Tohidi et al. [54] were the first to demonstrate visualization of hydrate formation in synthetic glass micromodels. Hydrates were formed from liquid tetrahydrofuran (C_4H_8O), free methane gas (CH_4), and dissolved carbon dioxide gas (CO_2). They found that upon agitation of the system by fluid flow, creating a pressure gradient across the micromodel, CO_2 hydrates formed in the direction of the fluid flow. Furthermore, they discovered that gas hydrates not only formed from free gas, but directly from the solution of dissolved CO_2 in the water phase. Initial hydrate growth occurred in a tendril and cross-hatched skeletal manner before culminating in a pronounced crystalline pattern as seen in Figure 3.1. The hydrates were localized at the center of the pore space, while a thin water film coated the water-wet glass surface. This water film could have a restricting effect on the cementation of the grains. However, Tohidi et al. [55] later investigated the self-sealing mechanism of CO_2 hydrates in subsea sediments and found that sequestered CO_2 migrated upwards towards the GHSZ where it formed hydrates with the pore water. It was found that CO_2 hydrate crystals filled the large pores, while thin layers (flakes) grew in the finer pores, reducing sedimentary permeability and preventing leakage of CO_2.

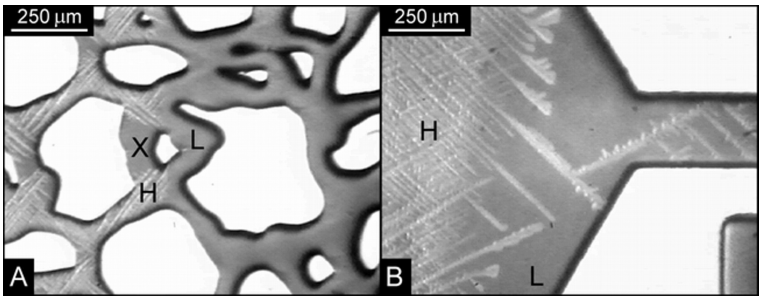

Figure 3.1: CO_2 hydrate formation in porous media: (a) Hydrate formation front (H) and liquid (L). (b) Skeletal hydrate formation layer. From Tohdi et al [54].

In a study by Gauteplass et al. [16], the trapping mechanisms of CO_2 hydrates at pore-level were investigated using a vertically positioned micromodel with flow direction from bottom to top as seen in Figure 3.2. The micromodel was saturated with deionized water before CO_2

was injected at the bottom, displacing the water upward until CO_2 hydrates formed. The researchers found that hydrate formation occurred uniformly trough the pore network, as opposed to the distinct hydrate front advancing through the pore space typically observed in the formation of CH_4 hydrates. Solid hydrate formation was mainly observed in larger pores initially occupied by liquid CO_2, followed by formation in smaller water-filled pores. After several days, the hydrate morphology changed from dark opaque to more transparent due to crystal rearrangement. The hydrates appeared to fill and cement the pore space, and the dissociation of local hydrate structures led to re-formation of the liberated fluids and had no effect on the integrity of the hydrate seal. Similar observations where made by Almenningen et al. [56]. They conducted pore-scale experiments to investigate liquid CO_2 flow and hydrate growth pattern within sedimentary pores. They found that the nucleation of solid hydrates started at the liquid-liquid interface between CO_2 and water and moved laterally into the water phase. They did not observe any movement of the hydrate front and the hydrate crystallized simultaneously in water-filled pores regardless of their size. The growth of hydrates into the CO_2 phase quickly ceased due to low supply of water, leaving pores filled with liquid CO_2 immobilized by the surrounding solid hydrates.

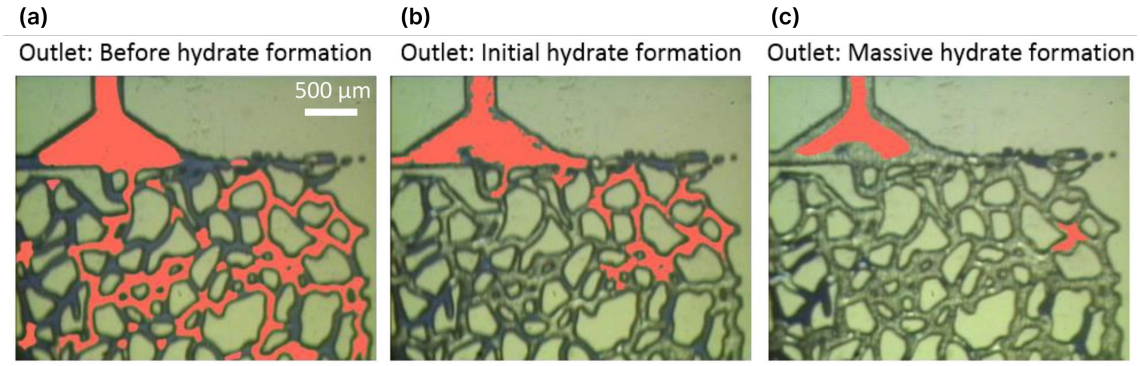

Figure 3.2: Pore-level CO_2 trapping mechanism in micromodel before hydrate formation (a), at the initial stages of hydrate formation (b), and after the initial stages (c). Red color = liquid CO_2, blue = water, gray = hydrate. Modified from Gauteplass et al [16].

Hauge et al. [57] studied CO_2 and CH_4 gas hydrate formation and growth pattern by direct pore-level visualization using the same micromodel as mentioned in the previous paragraph. The growth pattern and formation rate was investigated for both CO_2 and CH_4 hydrates, with a greater emphasis on the latter. They found that CO_2 hydrate formation occurred within connected gas-filled pores, likely because of the supply of mobile water film on the water-wet surface of the pore walls. After three hours a crystalline hydrate phase with lower free energy was observed close to the pore walls. Hydrates also formed in isolated gas bubbles

but no further growth was observed because of inhibited mass transfer due to the hydrate film covering the CO_2-water interface (yellow circle in Figure 3.3b). Pore-to-pore hydrate growth also occurred in water-filled pores when in contact with a hydrate-filled pore. In addition, hydrates formed from dissolved CO_2 in water-filled pores without free gas (white circle in Figure 3.3c).

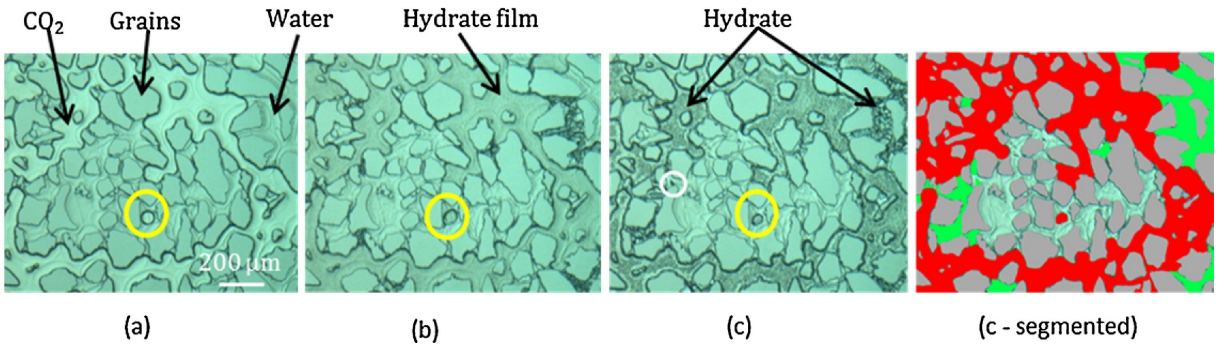

Figure 3.3: Image sequence of CO_2 hydrate formation. Showing (a) the initial water and gas distribution, (b) hydrate film formation surrounding a water-filled area, (c) hydrate redistribution over time, and (c - segmented) hydrate formation in gas-filled pores (red), water-filled pores (green), and water-filled pores with no hydrate formation (blue) [57].

Katsuki et al. [58] investigated the driving force of CO_2 hydrate formation and growth in a glass micromodel. The porous medium was either saturated with water and dissolved CO_2 or water and gaseous CO_2. In the experiments with CO_2 saturated water they observed that fine dendritic crystals formed after $\approx$ 17 s, further growth was observed as branching of the dendritic crystals which changed into particulate crystals (Figure 3.4). For the water saturated system, CO_2 vapor was injected into the water phase to facilitate hydrate formation, resulting in hydrate film formation at the interface between water CO_2 vapor. The hydrate film rapidly covered the CO_2 phase but turned crystalline in the matter of days (Figure 3.5). It was concluded that a higher driving force (degree of subcooling) resulted in fine dendrites and particulate crystals, while lower driving force resulted in faceted crystals which bridged the pores of the medium indicating good cementation properties.

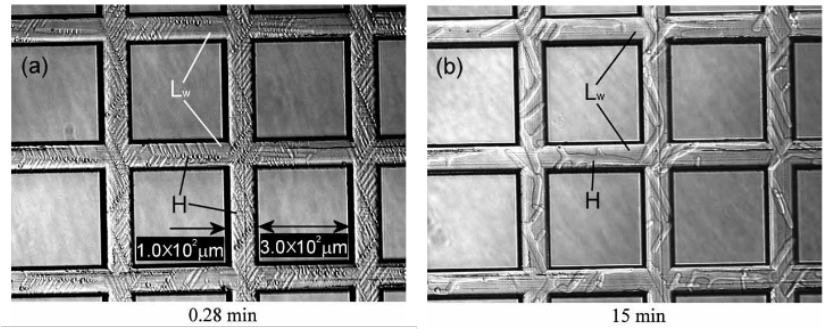

Figure 3.4: Images of hydrate formation in a micromodel filled with CO_2 saturated water and the morphological changes from (a) dendritic hydrate formation to (b) CO_2 particulate hydrate formation. Images modified from Katsuki et al. [58].

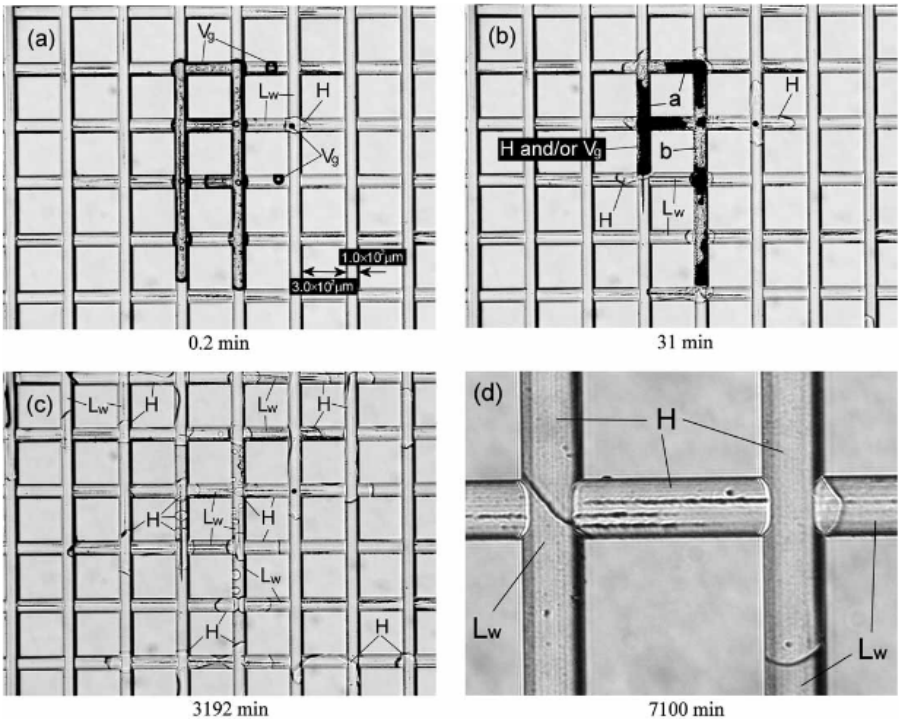

Figure 3.5: Images of hydrate formation in a micromodel filled with water and gaseous CO_2. The images show (a) hydrate formation at the interface between gaseous CO_2 and water, (b) the formation of hydrate film encapsulating the CO_2, and (c)-(d) porous hydrate film turning into faceted hydrate crystals. Images modified from Katsuki et al. [58].

3.2 Hydrate growth rate

Several researchers have studied the formation rate of natural gas hydrates but there are few papers on the formation rate of CO_2 hydrates. Uchida et al. [59] investigated the hydrate formation process at the interface between water and liquid CO_2 at different pressures and temperatures. A series of experiments were performed by injecting a drop of deionized water into a high-pressure vessel filled with liquid CO_2. When water came into contact with the CO_2 phase, CO_2 hydrate film formed at the interface between water and CO_2. They observed that the nucleation site and induction time was different in each experiment and that nucleation sometimes occurred at a site where a small impurity was in contact with the interface. Figure 3.6 shows the propagation process of the CO_2 hydrate film on the water droplet. The arrow in Figure 3.6a indicates the nucleation point on the interface and Figure 3.6a-e show the propagation process of the hydrate film. Figure 3.6f shows the droplet completely covered in hydrate film. After the hydrate film was formed, the thickening rate of the film became lower than the propagation rate and the hydrate grew mainly into the water phase. However, when in the presence of another water droplet, dendrite hydrate was observed to grow into the liquid CO_2 due to the additional source of water. This growth rate was 10^6 times slower than film propagation. The lateral propagation rate of CO_2 hydrate film was estimated to be in the range of $10^{-1} - 10^1\ mms^{-1}$ and was mainly controlled by the degree of subcooling. They also predicted the film thickness to be $0.13 \pm 0.01 \mu m$.

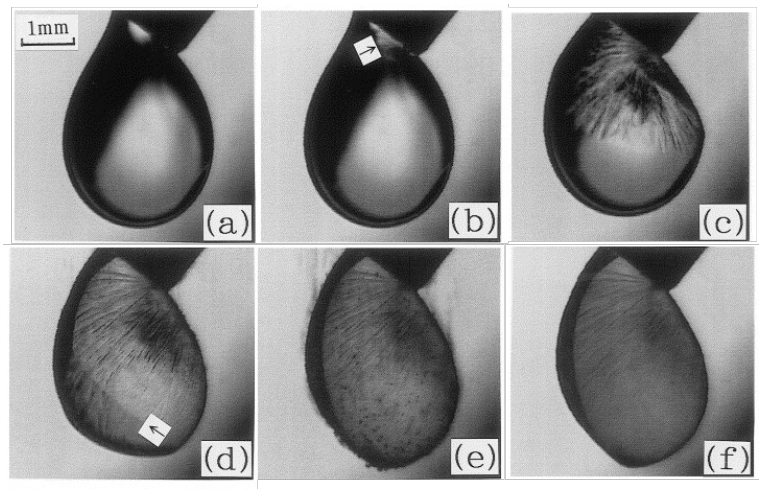

Figure 3.6: Hydrate film formation on a water droplet in liquid CO_2. The images are taken (a) before hydrate formation, (b) during nucleation of the hydrate film at the interface, (c) 0.5 seconds after nucleation (propagation of hydrate film), (d) 1 second after nucleation (second hydrate film observed), (e) 2 seconds after nucleation (bubble formation at the interface), and (f) 15 seconds after nucleation: the droplet is fully covered with hydrate [59].

3.3 The effect of salt on hydrate formation

Uchida et al. [60] also investigated the effect of NaCl on the lateral growth rate of the CO_2 hydrate film. The experiments were conducted using the same set-up as mentioned in the previous section. They found that the hydrate formation from NaCl solution and CO_2 is similar to that with deionized water. The lateral growth rate increased with increasing subcooling, thus the rate determining process was found to be heat transfer. However, the lateral growth rates were slower than for pure water. One explanation for this observation is the increasing NaCl concentration due to the desalination effect. Thus, it was concluded that the rate determining process for hydrate formation in saline water could be the diffusion of salt ions at the reaction site. Husebø et al. [61] reached the same conclusion in their work studying the effect of salinity on hydrate stability. They conducted coreflooding experiments using Bentham sandstone cores saturated with brine. the system was pressurized to 82 bar by injecting methane gas. They found that higher initial salinity resulted in longer induction time and inhibited hydrate formation. They concluded that, when the initial salinity is higher than 4.0wt%, the salinity of the residual water after hydrate formation was the limiting factor for hydrate formation.

Gauteplass et al. [15] conducted similar experiments to investigate the impact of temperature and brine salinity on sedimentary hydrate growth in water saturated sandstone. Coreflooding experiments were conducted under an experimental pressure of 70 bar, with three different conditions tested: 3.5wt% NaCl at 4°C, 3.5 wt % NaCl at 6°C, and 5.0wt% NaCl at 4°C. Hydrates formed and plugged the core sample in all experiments. However, increasing salinity from 3.5wt% to 5.0wt% led to a delay in the formation with 3.5 pore volumes of CO_2 injected. Two additional experiments were conducted at different flow rates using 7.0wt% NaCl at 4°C, but no hydrate formation was observed in either case.

Holzammer et al. [62] conducted a Raman study to investigate the effect of sodium chloride on the development of hydrogen bonds and the solubility of CO_2 in water right before hydrate formation. The experiments were conducted for six salt concentrations from 0.0 to 20.0wt% NaCl under constant pressure. They reported a decrease in hydrate formation with increasing salt concentration in compliance with literature data, however, a bigger scatter was observed for pure water. This could be because small impurities such as low concentrations of Cl^- and Na^+ ions serve as nucleation sites, enhancing hydrate formation. They also reported a decrease in the equilibrium constant K with increasing salinity, due to the water molecules surrounding the Cl^- and Na^+ ions disturbing the interaction between the water molecules, resulting in weaker hydrogen bonds. In addition, the solubility of CO_2 in water decreased

with increasing salinity, due to the salting-out effect. With a salt concentration of 20 wt % the solubility of CO_2 was reduced by 70 %. The decrease in CO_2 solubility contributed to a decrease in hydrate formation and formation temperature.

Research on hydrate formation, growth rate and the effects of additives such as salt have been of interest since the discovery of hydrate plugs in hydrocarbon production pipelines. However, most research have focused on methane recovery from hydrate bearing sediments by CO_2/CH_4 exchange mechanisms. There is less research on CO_2 hydrates. Moreover, research on the effect of salinity on hydrate formation have mostly been performed in bulk phase and not at pore-scale.

4. Methodology

4.1 Experimental set-up and equipment

The following sections describes the experimental set up, the characteristics of the micromodel, and the experimental procedures. All 19 experiments were performed at the Department of Physics and Technology at the University of Bergen.

The experimental set-up used in this work was adapted from previous work performed by master and PhD students with the Reservoir Physics group at the Department of Physics and Thechnology. The micromodel was submerged in a dual cooling chamber composed of an inner chamber, an adjacent outer chamber, and a refrigerated bath circulator. The inner part of the chamber was filled with deionized stagnant water and covered by a lid to ensure undisturbed visual communication between the micromodel and the microscope. The outer chamber was used to circulate cooling liquid (deionized water) through the refrigerated bath circulator to maintain a constant temperature throughout the experiments. The two chambers were separated by an aluminum barrier to ensure efficient heat transfer between the circulating cooling liquid and the micromodel submerged in stagnant water. The temperature was measured using a thermocouple placed directly under the micromodel.

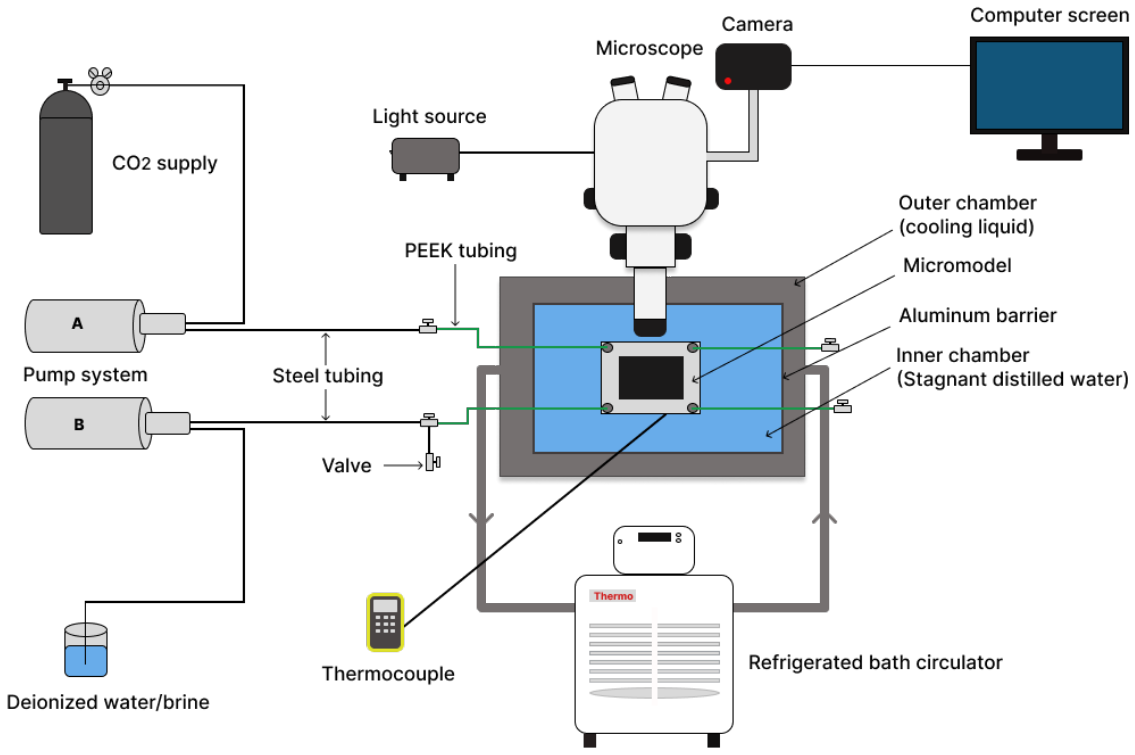

Figure 4.1: Experimental set-up.

A high-pressure, Quizix SP-5200 pump system consisting of two cylinders was connected to the micromodel by PEEK and steel tubing. The cylinders were denoted cylinder A and B and were each filled with a distinct fluid, CO_2 and deionized water/brine, respectively. Cylinder A was connected to port 1 and cylinder B was connected to port 3. The two remaining ports were not connected to the pump system, with port 2 being the production outlet and port 4 being used to induce agitation of the system. Two operating modes were used: constant volumetric flow rate mode was used to inject and retract fluid and constant pressure mode was used to monitor and maintain a constant pressure. Visual data was obtained by a camera (Nikon D7100) connected to a microscope, the camera was further connected to a computer which provided live view monitoring of the system, as well as videos and images. The field of view was illuminated by a cold light source. The chemicals used in this work are listed in table 4.1, while a complete list of the experimental equipment can be found in Appendix A.

Table 4.1: Table of chemicals, provider and purity.

Chemicals	**chemical formula**	**provider**	**purity**
Carbon dioxide	CO_2	Nippon Gases	100%
Sodium chloride	NaCl	Supelco	$\geq$ 99.5%
Calcium chloride dihydrate	$CaCl_2$	Merck	$\geq$ 99.5%

4.1.1 Micromodel

CO_2 gas hydrate formation was studied at pore-level using a 2D porous micromodel. The high-pressure micromodel system consists of an etched silicon wafer and optically transparent borosilicate glass. A well-defined two-dimensional geometric pattern based on real Berea sandstone was etched in the silicon wafer by a DRIE (Deep Reactive Ionic Etching) technique. Berea sandstone is a sedimentary rock known for its high porosity and permeability, making it a common reference for studying fluid flow through sandstone pores. The sandstone is primarily composed of quartz grains, but its clay composition varies. The DRIE technique produces highly accurate patterns which ensure an exact representation of the rock properties such as sharp edges, rough pore walls, pore throats and pore bodies found in Berea sandstone. Figure 4.2 is a scanning electron microscope image of the pores in the etched-silicon micromodel. The pore pattern comprised 36 repetitions of pore network, which can be considered a simplified two-dimensional projection of real pore structures (Figure 4.3). The etched silicon wafer was later enclosed by anodically bonding it to a silica glass plate. The system can be pressurized to 150 bar without external confinement pressure. The micromodel was naturally water-wet due to a silicon dioxide film coating the surfaces, the detailed

manufacturing process is described elsewhere [63]. The micromodel had dimensions of 27 mm x 21.4 mm x 0.003 mm, with an average pore diameter of 100 μm, detailed specifications are listed in Table 4.2. Each corner of the micromodel was connected through flow lines providing external access to the porous system, enabling fluid injection, production, and pressure monitoring. Two flow distribution channels connecting ports 1 and 2, 3 and 4, ensured distribution of fluids through the micromodel.

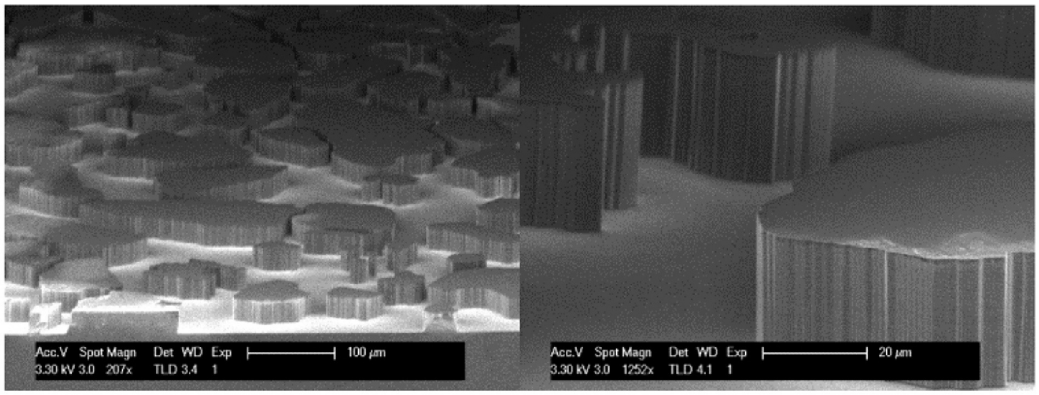

Figure 4.2: Scanning electron microscope (SEM) image of the pore walls in the etched-silicon micromodel [57]

Table 4.2: List of micromodel properties from Benali et al. [64]

Parameter	**Value**
Width	27 mm
Length	21.4 mm
Depth	30 $m\mu$
Porosity	0.61
Permeability	2.97 D
Pattern repetition	36
Unique grains	749
Total Grians	27000
Grain Size	100-79000 μm^2
Pore throat length	10-300 μm
Pore volume	11.1 μL

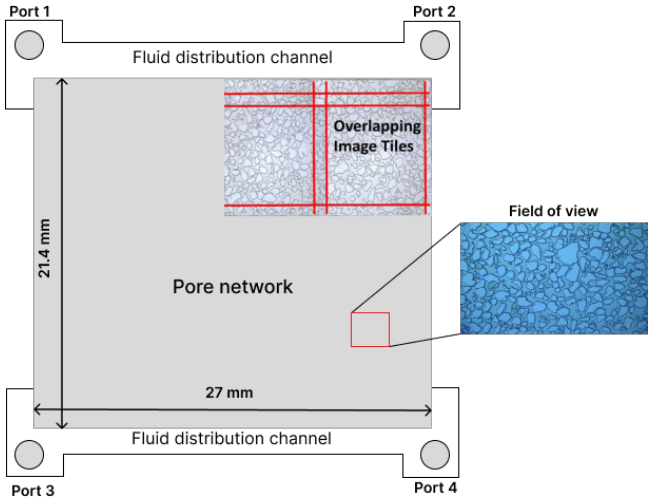

Figure 4.3: Schematic representation of the micromodel dimensions with two fluid distribution channels, four ports and field of view (1% of micromodel).

4.2 Experimental procedure

Before each experiment, the micromodel was cleaned by injection of one pore volume of isopropanol and 40 mL deionized water.

4.2.1 Formation

1. Cylinders A and B were pressurized with liquid CO_2 and water, respectively.
2. The micromodel was flushed with water/brine to ensure 100% saturation of the system.
3. Only the valve connected to the water cylinder was open to pressurize the system to 70 bar by setting the water pump to independent constant pressure operation while increasing the pressure in increments of 10, to 70 bar.
4. The pressure in cylinder A was increased to 70 bar. The temperature of the micromodel and the cylinder volume of CO_2 was measured, and the data log was started.
5. CO_2 was injected by opening the valve connecting cylinder A to the micromodel and injecting at a constant flow rate of 10mL/h until 30 seconds after CO_2 entered the pore system, which was confirmed visually.
6. The water valve was closed, and the CO_2 pump was set to independent constant pressure operations at 75 bar for 24 hours to ensure that the CO_2 was fully dissolved in the media and that there were no leakages in the system.
7. After 24 hours the dual cooling bath system was set to 3.5°C and left for an additional 24 hours. The target temperature and pressure ensure the system is within the hydrate stability zone.
8. The camera was set to automatic interval shooting (every 15 minutes) to monitor the fluid behavior in the micromodel.
9. If no hydrates formed within 24 hours under the given thermodynamic conditions the system was agitated by swiftly opening and closing the outlet. This created a pressure difference through the micromodel, causing the fluids to redistribute, resulting in hydrate formation within minutes.
10. Before agitation the camera was set to video recording to monitor the fluid behavior and hydrate formation. After agitation and initial hydrate formation, the camera was set to automatic interval shooting (every second minute) for another 24-48 hours.

4.2.2 Dissociation

Hydrate formation usually lasted for 24-48 hours until there was no more visible changes, then the cooling system was turned off. When the system reached ambient temperature, it was depressurized to induce hydrate dissociation in the following way:

1. The CO_2 cylinder pump was turned off and the valve was closed.
2. The water cylinder pump was pressurized to the system pressure (75 bar) and the water valve was opened.
3. The water pump cylinder was retracted at a constant volumetric rate from 1 mL/h to 50 mL/h.
4. When the system pressure was lowered 5-10 bar below the equilibrium pressure at ambient temperature, the pump cylinder was set to constant pressure operation mode.
5. Subsequently, the camera was set to video recording to monitor the hydrate dissociation.

4.3 Optical properties

This section describes the optic properties of the microscope and the interpretation of the images acquired from the two-dimensional micromodel.

The microscopic view of the micromodel was illuminated by a light source. The light propagated through the micromodel and the different media before it was reflected back to the microscope. Therefore it is important to understand the propagation of light through the micromodel in order to interpret the data. The hydrate growth in the micromodel resulted in two different hydrate formation types 1) hydrate film encapsulating the liquid carbon dioxide and, 2) crystalline hydrate. The media present in the micromodel is liquid CO_2 (L), water (W), crystalline hydrate (H), hydrate film encapsulating liquid carbon dioxide (HF), and grains (G) as illustrated by Figure 4.4. The wettability of the micromodel can be used to distinguish the different fluids. Due to the water wet nature of the micromodel, carbon dioxide develops a convex curvature toward the water phase and the pore walls, making it possible to distinguish liquid carbon dioxide from water. In addition, the roughness of the micromodel bottom caused water droplets of different sizes to reside below the liquid carbon dioxide giving the liquid CO_2 a grainy appearance as seen in Figure 4.4a.

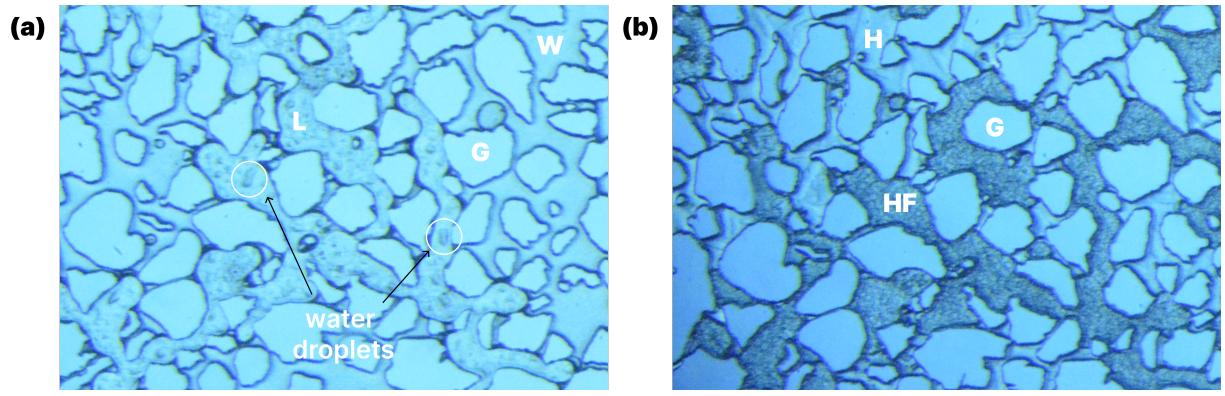

Figure 4.4: View of the micromodel and the fluids within the pore space: (a) water (W), liquid carbon dioxide (L) with water droplets residing below, and grains (G) before hydrate formation. (b) Hydrate film (HF), crystalline hydrate (H) and grains (G).

The refractive index (n) can also be used to identify the fluids in the micromodel. As light propagates through a medium the light is bent (refracted) and reflected back at a different angle. The index describes how light propagates through a medium and is a measurement of the refracted light. The refractive indices of the phases present in the micromodel is listed in Table4.3. The difference in the refractive index of water (1.333) and liquid CO_2 (1.200-1.250) makes the hydrate film easily detected. When liquid CO_2 is present beneath the hydrate films, it causes the light to bend and reflect at the boundary between the fluids, resulting in a small amount of light returning to the microscope. This leads to the hydrate films appearing darker than they would otherwise. Scientific literature on the refractive index of crystalline CO_2 hydrates is not readily available. However, since both CO_2 and methane hydrate form structure I hydrates, the refractive index of crystalline methane hydrate (1.346) will be used for this section. The refractive index of crystalline hydrate is close to that of water causing no reflection of light at the interface between the two fluids. The light propagates through both water and hydrate before it reaches the bottom of the micromodel and is reflected back to the microscope. The crystalline hydrate therefore appears transparent making it difficult to visually distinguish the two phases.

Table 4.3: Refractive indices of the fluid phases present in the micromodel.

Fluid phase	**Refractive index** (n)
Liquid water	1.333 [65]
Liquid CO_2	1.200-1.250 [66]
CH_4 crystalline hydrate	1.346 [67]

4.3.1 Image quality

This thesis presents raw data in the form of two-dimensional micromodel images. The quality of these images varied and was affected by factors such as camera settings, external light sources, microscope magnification, and the position of the micromodel relative to the microscope.

The images were generated either by interval timer shooting or by video recording. Video recordings captured the initial hydrate formation, whereas interval timer shooting was utilized to observe system changes after the initial formation. Images from video recordings were extracted as individual frames using MATLAB. Even though the same camera was used for both interval timer shootings and video recording, the two functions had different camera settings which resulted in different image quality and magnification. The images obtained from video recordings exhibited higher color contrast and magnification compared to the images generated by interval timer shooting.

The internal light source did not provide uniform illumination of the field of view, causing uneven lighting across the micromodel. This was particularly pronounced at lower magnification, causing the images to appear darker in the edges than in the center (Figure 4.5). This effect was minimized by choosing a higher magnification. The microscope had a magnification ratio of 0.75X-11.25X and the magnification ratio used in this work ranged from 4X-5X.

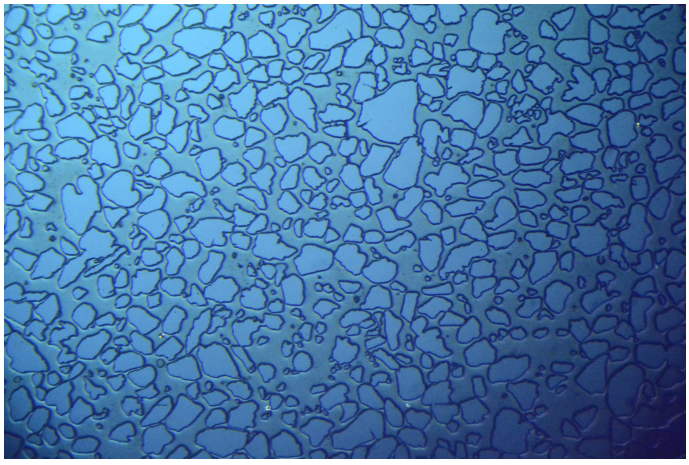

Figure 4.5: Illustration of the uneven illumination through the micromodel field of view. The upper right corner and lower corners appear darker.

Furthermore, although the experimental set-up was designed to be isolating, some external light was able to penetrate through the exterior of the chamber. As a result, the brightness of

the images taken throughout the experiment differed as seen in Figure 4.4. The micromodel was placed parallel to the microscopic lens inside the cooling chamber to ensure an even color distribution. However, the construction of the experimental set-up resulted in a slight angle between the micromodel and the microscope lens. This angle caused a color gradient through the micromodel, making some parts appear blue in color while others appear pink or grey as seen in Figure 4.6.

Figure 4.6: The color difference within the micromodel caused by the color gradient.

4.4 Image analysis method

This thesis provides both qualitative and quantitative descriptions of hydrate formation on pore scale. The qualitative analysis focused on studying the behavior of hydrates in porous media, particularly the observation of various hydrate configurations during formation under different conditions such as temperature, and salinity. The quantitative analysis was a characterization of the images to analyze and quantify image characteristics such as phase saturations and gray scale variations. By quantifying these parameters, it is possible to obtain a more precise understanding of hydrate formation dynamics. Since the pore volume of the micromodel (11.1 μL) is several orders smaller than the volume of the tubing, material balance calculations would be very sensitive to small leakages of the system and therefore not applicable. Instead, fluid saturation and hydrate growth rates were estimated by quantitative characterization of the images using the visualization software ImageJ.

4.4.1 Hydrate formation and growth

Besides the qualitative description of hydrate formation and growth in porous media, hydrate formation was also quantified using to two different approaches: (1) Saturation calculations and (2) Measurement of change in gray scale. Saturation calculations are estimates of the fluid distribution within the two-dimensional micromodel field of view and will be further discussed in the following section. The change in gray scale serves as an indicator for estimating hydrate growth. Both water and liquid CO_2 exhibit lighter colors compared to porous

hydrate. As hydrates form, the initial porous hydrate phase appears dark (gray/black), leading to a decrease in the gray scale. Therefore, a reduction in the gray scale signifies hydrate growth and film thickening.

To study the effect of water saturation on hydrate formation, data points of initial water saturation vs. hydrate saturation were plotted. Additionally, the effect of water saturation on induction time was investigated. Driving force in the terms of temperature was also investigated by plotting the temperature vs. hydrate saturation and induction time. Lastly, the effect of salinity was examined by plotting the salinity against hydrate saturations.

The change in gray scale and characterization of the hydrate front is typically used to calculate hydrate growth rates. However, in most experiments there was little to no hydrate front observed and in the experiments where a hydrate front was observed, the front propagation was too fast to measure. Therefore, hydrate growth rates were estimated by measuring the global gray scale of the image sequences in incremental steps and plotting change in gray scale vs. time.

4.4.2 Fluid saturation

Fluid saturations including initial water saturation and hydrate saturations (crystalline and porous) were determined using image sofware ImageJ. At the onset of hydrate formation, the grain area and the fluids present in the micromodel field of view was identified and segmented by adjusting the image threshold as seen in Figure 4.7. Subsequently, the porosity of the porous media and the fluid saturations were calculated based on the pixel count of the segmented phases. This procedure was repeated at a specified time after hydrate formation.

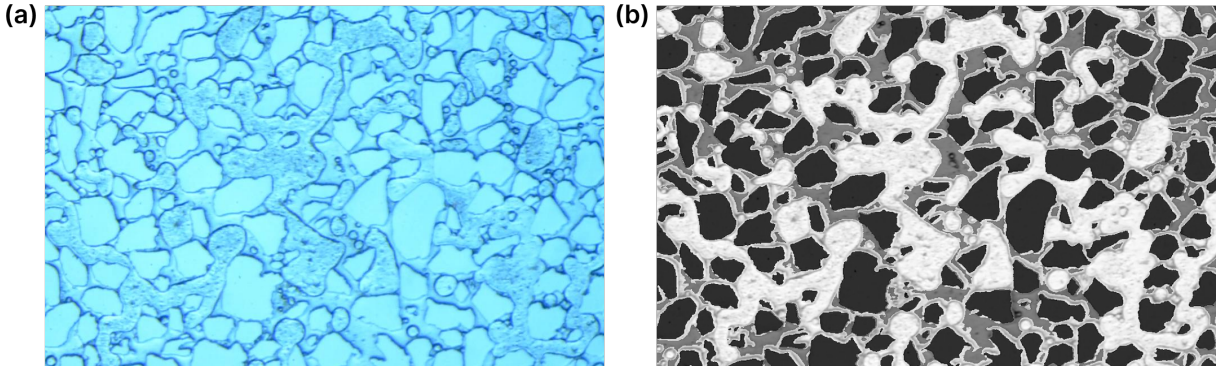

Figure 4.7: Illustration of the image processing and segmentation using ImageJ. (a) The original image is extracted from video recordings of hydrate formation in experiment 19. (b) The processed and segmented image. The grains are colored black, the water phase is a darker gray color, and the CO_2 phase is a light gray color.

The total image area is expressed in pixels, and each shade og gray covers a certain amount of number of pixels. The porosity and fluid saturations were estimated through the pixel count analysis, by the following equation:

Porosity:

$$\phi_p = \frac{A_v}{A_{tot}} = \frac{N_v}{N_{tot}} = \frac{N_{tot} - N_{grains}}{N_{tot}} \tag{4.1}$$

Where ϕ_p is the porosity, A_v and A_{tot} are the area of void space and the total area of the image respectively, N_v, N_{tot}, and N_{grains} are the number of void pixels, total number of pixels in the image and the number of grain pixels respectively.

Saturation:

$$S_i = \frac{A_i}{A_v} = \frac{N_i}{N_v} \tag{4.2}$$

where A_i is the area of a particular phase (gas or hydrate) and N_i is the number of pixels for that phase. Since the sum of phases saturating the pore space must equal 1, the water saturation could be estimated as the difference between 1 and the sum of the remaining saturations of the phases.

The standard deviation, σ, of each area measurement is given by the analysis tool ImageJ, the standard deviations of the water and hydrate saturations were calculated from the given standard deviations by the following equation:

standard deviation:

$$S = S_i \sqrt{(\frac{\sigma_{Ai}}{A_i})^2 + (\frac{\sigma_{A_v}}{A_v})^2} \tag{4.3}$$

Where σ_{Ai} is the given standard deviation of the area of a particular phase. And σ_{tot} is the standard deviation of the total area of void space.

Saturation calculations were performed under the assumption that all CO_2 is completely consumed in areas where the hydrate film covers the CO_2 phase, providing two-dimensional approximations of fluid saturations. However, this approach does not consider the coexistence of multiple fluids within the pore depth, except for initial water saturations, where larger water droplets are included in the calculations. As a result, the obtained saturations serve only as approximations of the three-dimensional fluid distributions within the micromodel field of view. The hydrate film saturation represents a two-dimensional estimation of how much CO_2 is encapsulated by the film, but the film thickness is not estimated due to the microscope's limited resolution.

5. Results and discussion

This chapter presents the results obtained from the micromodel experiments, which are analyzed both qualitatively and quantitatively. CO_2 hydrate formation, growth patterns, and the effect of salinity on pore scale will be investigated to asses the potential of utilizing hydrates as a sealing mechanism for geological CO_2 storage. Section 5.1 provides a qualitative description of hydrate formation in porous media, while section 5.2 is a quantitative analysis of hydrate formation and growth.

The 19 hydrate formation experiments conducted in this project are listed in Table 5.1. The effect of initial water saturation on hydrate formation was investigated for all 19 experiments. Seven experiments were carried out to study the CO_2 hydrate formation mechanics and growth pattern using deionized water, while twelve experiments were performed to investigate the effect of salinity on hydrate formation and growth. For the experiments conducted with deionized water, the formation pressure, p, was kept constant at 75 $\pm$ 1.4 bar, while the system temperature, T, ranged from 2.0-5.0 $\pm$ 0.2 °C. After experiment 5, there was a blockage in the tubing of the experimental set-up and the micromodel underwent maintenance where the original tubing was replaced. Therefore, experiments 1-5 differ from the rest with regard to agitation and fluid flow.

The remaining twelve experiments were performed using brine. Six of these were performed with varying concentrations of NaCl (1-5wt%), and six experiments with varying concentrations of $CaCl_2$ (1-5wt%). For this purpose, the pressure and temperature of all twelve experiments were kept constant at 75 $\pm$ 1.4 bar and 3.5 $\pm$ 0.2 °C. Experiments with salinities of 1-3wt% are referred to as low-salinity experiments, while experiments with salinities of 4 and 5wt% are denoted high-salinity experiments. Both experiments 6 and 17_2 were performed with no visible initial CO_2 in the system before agitation and therefore differ from the rest of the experiments. All 19 hydrate formations were induced by agitation causing a pressure pulse, fluid flow, and redistribution of fluids through the micromodel.

The Quizix Q5200 pump system has an uncertainty of $\pm$1.4 bar, and the thermocouple has an uncertainty of $\pm$0.1°C. However, the system temperature fluctuated by 0.1°C due to temperature fluctuations in the laboratory and therefore the uncertainty in the measurement was set to 0.2°C. The uncertainty of the brine concentrations is 0.02wt%.

Table 5.1: Summary of the micromodel experiments and the experimental conditions.

DI-water			**NaCl**				**$CaCl_2$**			
Exp.	**p** [bar] ±1.4	**T** [°C] ±0.2	**Exp.**	**C** [wt%] ±0.02	**p** [bar] ±1.4	**T** [°C] ±0.2	**Exp.**	**C** [wt%] ±0.02	**p** [bar] ±1.4	**T** [°C] ±0.2
1	75	5.0	**6**	1.0	75	3.5	**14**	1.0	75	3.4
2	75	5.0	**8**	1.0	75	3.5	**15**	2.0	75	3.6
3	75	5.0	**9**	2.0	75	3.4	**16**	3.0	75	3.5
5	75	3.5	**10**	3.0	75	3.5	**17**	4.0	75	3.5
13	75	3.5	**11**	4.0	75	3.6	**17_2**	4.0	75	3.5
19	75	2.0	**12**	5.0	75	3.5	**18**	5.0	75	3.5
20	75	5.0								

5.1 Qualitative analysis of hydrate formation and growth

The pore space was initially filled with liquid CO_2 and water/brine. Agitation of the system resulted in the displacement of water and high saturations of CO_2 due to its high mobility and sweep efficiency. After agitation, several hydrate growth mechanisms were observed. This section provides a qualitative analysis of the observed hydrate growth mechanisms in the micromodel. Section 5.1.1-5.1.5 is an analysis of the general growth mechanisms and crystal configurations in the continuous CO_2 phase and the water phase, while section 5.1.6 is a qualitative analysis of the effect of salt on hydrate growth mechanisms.

5.1.1 Hydrate formation mechanisms and crystal configuration

Two different hydrate configurations were observed: (1) hydrate film encapsulating gas and (2) nonporous crystalline hydrate. Hydrate films appeared gray in color and was the most abundantly observed hydrate crystal morphology. Hydrate film forms as shell-like growth along the water-CO_2 interface resulting in porous hydrate with encapsulated CO_2 within the hydrate shell. Transformation from black porous hydrate film to transparent crystalline hydrate by CO_2 consumption and inward crystal growth requires sufficient water diffusion through the hydrate film. Hydrate film growth without complete conversion to solid hydrate is thought to form when there is an insufficient mass transfer of water or insufficient pressure in the CO_2 phase [53]. Crystalline hydrate, being transparent, is considered non-porous and free of encapsulated CO_2, making it the more stable crystal morphology compared to the black porous hydrate. Crystalline hydrate was observed in the water-filled pores within

seconds of agitation. However, when water was the limiting hydrate-forming component, little to no crystalline hydrate would form in the water phase.

In this work, higher water saturations (S_{wi}>0.40) usually led to continued growth and conversion from porous hydrate to crystalline hydrate within 24 hours of agitation as seen in Figure 5.1. In the continuous CO_2 phase the water availability is limited to the thin water film coating the grains, top, and bottom of the micromodel. At low initial water saturations, the water film is sufficient to form the hydrate film, encapsulating the CO_2, but further growth requires an additional water supply. Water transfer from adjacent/neighboring water-filled pores can supply water to the inward hydrate growth, but the migration of water is slow. Therefore, the hydrate film thickens gradually over time causing a change in gray scale from light gray to darker gray. At high initial water saturations the hydrate texture and gray scale changed from a dark coarse texture to more transparent indicating a redistribution of fluids and solidification of a dense crystalline hydrate phase.

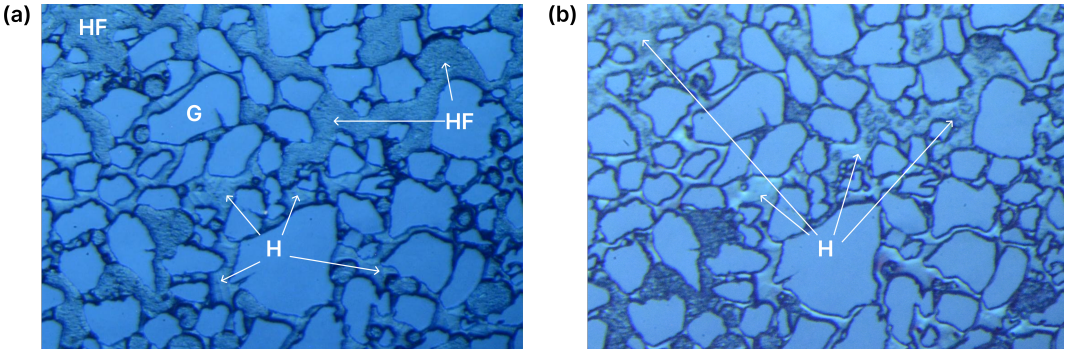

Figure 5.1: Hydrate formation in experiment 13. The two images show (a) hydrate configurations 4 minutes after initial hydrate formation. Crystalline hydrate (H) formed in the water phase and hydrate film (HF) in the CO_2 phase. The hydrate film appeared gray in color with a coarse texture, while the crystalline hydrate appeared transparent with a distinct crystalline texture. And (b) hydrate configuration 18 hours after initial hydrate formation. large amounts of the hydrate film slowly transforms into a transparent and more crystalline hydrate configuration.

Almenningen et al. [68] obtained similar results when studying the effect of water saturation on hydrate formation. At low initial water saturation (S_{wi}<0.50), the hydrate formation was slow (∼6 minutes) due to the limited availability of water. The water was fully consumed and the final fluid configuration consisted of hydrate film encapsulating the gas. High initial water saturation (S_{wi}>0.50) resulted in a rapid crystalline hydrate formation in the water phase. Nearly all of the gas was consumed to form solid hydrates due to the sufficient local water supply.

5.1.2 Hydrate formation and growth at the water-CO_2 interface

Hydrate formation was first observed at the curved water-CO_2 interface and along the vertical pore walls, followed by film formation in the center of the pore. The formation was rapid, usually within 20 seconds of agitation. The rapid formation is likely because of the large surface area between water and CO_2 due to the water-wet nature of the micromodel. The grains are rectangular in shape and placed vertically and perpendicular to the top (glass) and bottom (wafer) of the micromodel. Water films coat the vertical pore walls and the horizontal bottom and top of the micromodel. As shown in Figure 5.2 (a), water accumulates in the pore corners, while CO_2 fills the center of the pores. Hydrate growth initiates at the water-CO_2 interface because concentrations of water and CO_2 at this interface greatly exceed their mutual solubilities [42, 56, 57, 58, 59]. The availability of water and CO_2 is therefore higher at the interface between the fluids. Hydrate formation is therefore expected to initiate at the water-CO_2 interface in the pore corners, followed by simultaneous growth in all water-CO_2 interfaces. This coincides with the observed hydrate growth pattern in this work, where hydrate formation initiated at the water-CO_2 interface in pore corners, followed by simultaneous growth in all fluid interfaces. Similarly, Almenningen et al. [56] found that hydrate film formation around the CO_2 phase was rapid, while the lateral movement of the hydrate front into the CO_2 phase and thickening of the film was slower due to the restriction of mass transfer through the hydrate film [69].

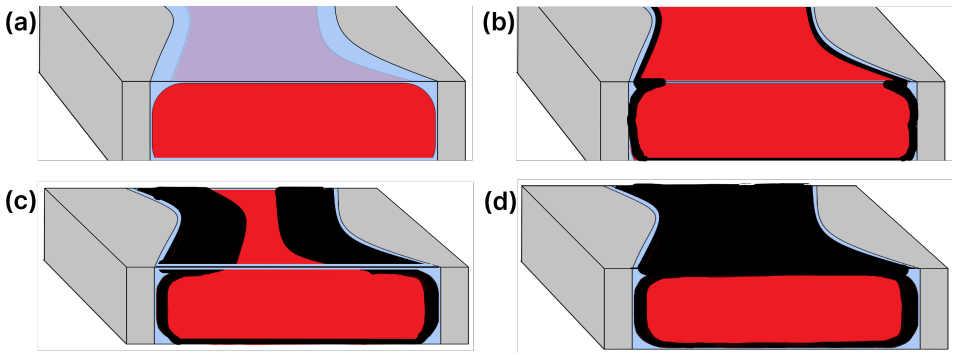

Figure 5.2: Schematic model of the fluid distribution in a gas-filled pore within the micromodel. The model is a three-dimensional cross-sectional area of a pore (gray), with water (blue) coating the pore walls and top glass (only visible in (a)). CO_2 residing in the center of the pore is illustrated by the red area, and hydrate film is represented by the black area. (a) Water films coat the grains, top, and bottom of the micromodel. Due to the shape of the pore, the water film is thicker in the corners. Liquid CO_2 resides in the middle of the pore due to the water-wet nature of the micromodel. (b) Hydrate film formation at the interface between water and CO_2. (c) Hydrate film grows from the pore walls into the liquid CO_2 phase. (d) The CO_2 is encapsulated in hydrate film.

5.1.3 Hydrate formation and growth in the CO_2 phase

Table 5.2: Overview of experiments conducted using deionized water at varying temperatures. The results are obtained from the video image sequences approximately 20 minutes after agitation.

Exp.	**T** [°C]	**Pore-filling**	**Hydrate front**	**Crystalline hydrate**	**Induction time** [s]
1	5.0	No	Yes	Yes	10
2	5.0	No	Yes	Yes	12
3	5.0	No	Yes	Yes	6
5	3.5	No	Yes	Yes	6
13	3.5	Yes	No	Yes	5
19	2.0	Yes	No	Yes	3
20	5.0	Yes	No	Yes	8

The experiments conducted using deionized water (experiments 1-5, 13, 19, and 20) are listed in 5.2. For experiments 1-5, a hydrate front propagating from the pore wall to the pore center was observed. However, due to a blockage in the micromodel tubing and maintenance performed on the experimental set-up, these experiments differ from the rest. No hydrate front was observed in the three remaining experiments performed using deionized water (experiments 13, 19, and 20). Regardless, it was commonly observed in all deionized water experiments that simultaneous to the initial hydrate film formation at the curved water-CO_2 interface, further hydrate nucleation occurred at the interface of larger water droplets residing underneath the CO_2 phase. An expansion of the hydrate film into the water phase was also observed for all experiments, illustrated by the red circle in Figure 5.3b.

Conversely, previous research on hydrate growth in the continuous CO_2 (or CH_4) phase reports initial hydrate formation at the curved interface between water and CO_2 (CH_4) close to the pore wall followed by propagation of the hydrate front towards the pore center [56, 57, 58, 59]. The observations made in this project suggest that initial hydrate film formation is not limited to the curved interface and pore walls, as previous research suggested, but can happen anywhere along the interface of CO_2 and water as seen in Figure 5.3a-b. For experiments 1-5, further growth was observed as propagation of the hydrate front into the CO_2 phase from the nucleation points by consumption of smaller water droplets in the continuous CO_2 phase (Figure 5.3c). In small pores, the development of the hydrate film was rapid and resulted in complete encapsulation of the CO_2. Conversely, in larger pores, the film propagation was slower and the advancement of the hydrate front into the CO_2

phase was limited, likely due to insufficient water supply. The low initial water saturations in experiment 1-5, could explain why the hydrate front did not propagate further. Unlike the other experiments, there was less conversion of the porous hydrate to a crystalline structure, further supporting the theory that water was the limiting component in these experiments. Under high pressure and low-temperature conditions, the solubility of liquid CO_2 in water is much greater than the solubility of water in liquid CO_2 [70]. Consequently, a negligible amount of water is dissolved in the CO_2 phase and hydrate growth is therefore strongly dependent on capillary forces and water film flow to drive water to the formation site. Once all water is consumed, growth ceases. The formation is therefore strongly dependent on the initial water saturation.

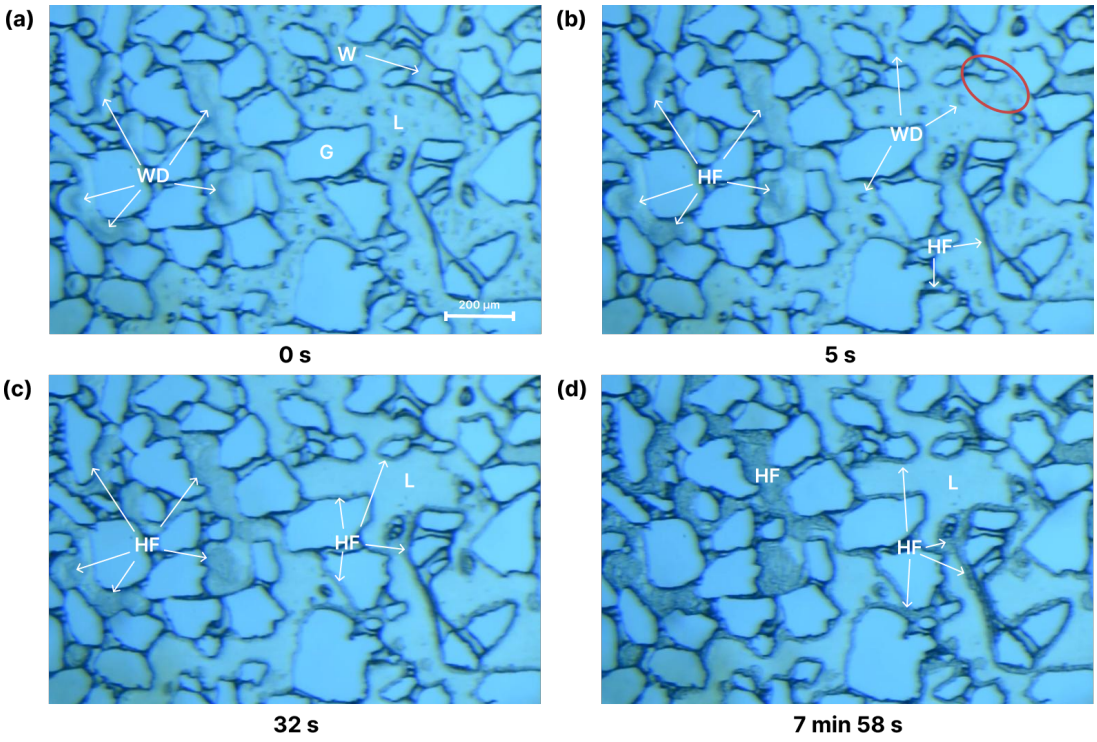

Figure 5.3: Hydrate film formation (HF) in experiment 1. The time lapse from hydrate formation (0 s). (a) Before hydrate film (HF) develop in the continuous CO_2 phase (L). Larger water droplets (WD) reside underneath the CO_2, while smaller water droplets give the CO_2 phase a grainy appearance. (b) The larger water droplets (WD) work as nucleation sites for hydrate film formation in the CO_2 phase. Hydrate film (HF) form at the water-CO_2 interface and on the larger water droplets in the continuous CO_2 phase. (c) The hydrate film propagates from the nucleation site into the CO_2 phase and the smaller water droplets are consumed. (d) The hydrate film thickens causing a darkening of the gray scale.

In the deionized water experiments conducted after the maintenance of the micromodel (experiments 13, 19, and 20), the initiation of hydrate film growth occurred simultaneously at both the curved water-CO_2 interface and the interface of water droplets within the continuous CO_2 phase, as seen in Figure 5.4b. Hydrate film thickening was observed as further darkening of the gray scale and seemed to develop uniformly through the field of view (Figure 5.4c. Contrary to experiments 1-5, no lateral movement of the hydrate front into the CO_2 phase was observed and the hydrate configuration appears to be completely grain contacting and pore-filling. Following the initial hydrate formation, the hydrate film continued to expand into the water phase, indicating further growth and water consumption. As water was consumed, the hydrate configuration began changing from dark coarse porous hydrate to transparent crystalline hydrate until all the residual water was consumed and the hydrate formation ceased as seen in Figure 5.4c (after approximately 24-48 hours).

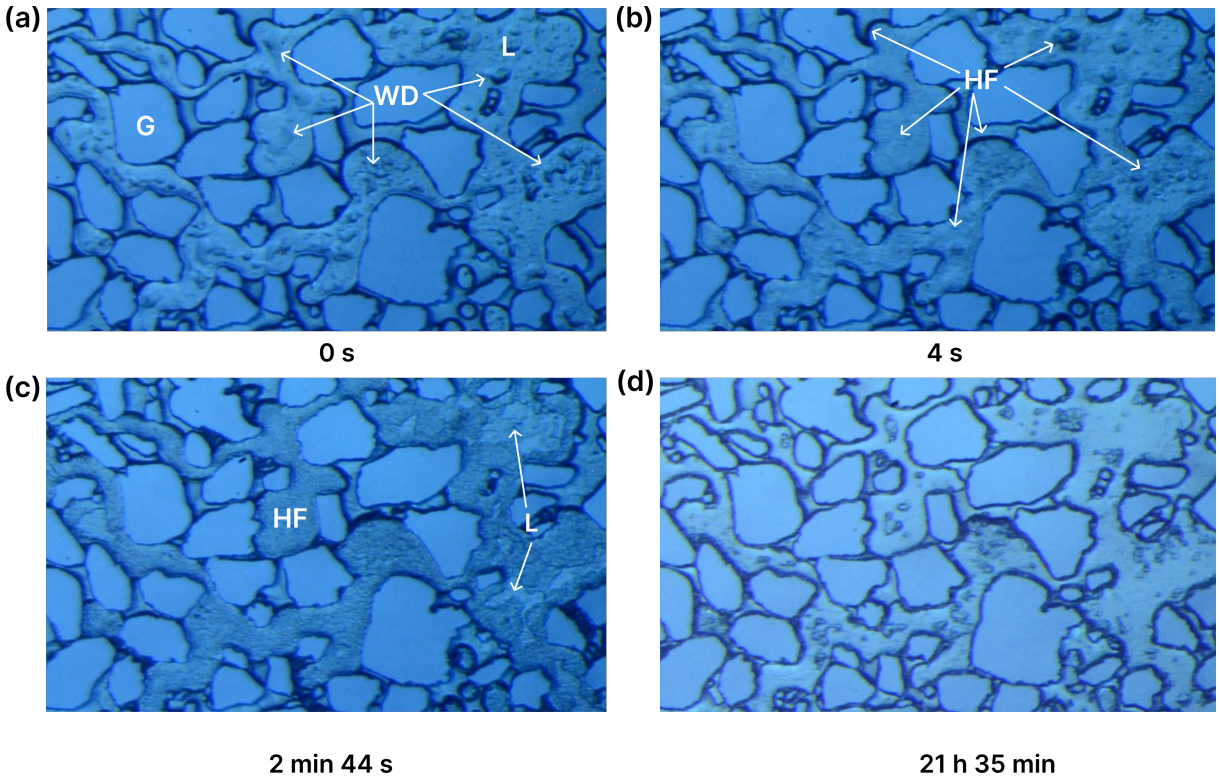

Figure 5.4: The figure is a representation of uniform hydrate film formation in experiment 13. The images show the time-lapse from hydrate formation. (a) One second before hydrate formation. Water droplets (WD) reside below the continuous CO_2 phase (L). (b) Hydrate film formation (HF) at the water-CO_2 interface in the continuous CO_2 phase. Larger water droplets function as nucleation sites and there is no hydrate front movement. (c) Thickening of the hydrate film by consumption of water. (d) The transformation from porous hydrate to crystalline hydrate in the continuous CO_2 phase.

The absence of lateral movement of the hydrate front into the CO_2 phase can be attributed several factors. First, the water droplets residing underneath the CO_2 could be sufficiently supplying water to the hydrate formation causing a uniform hydrate film layer around the CO_2 phase. Second, it could be due to the driving forces, such as pressure difference before and after agitation or degree of subcooling. Higher driving forces such as temperature and pressure reduces induction time and promotes hydrate formation. Considering the tubing was replaced in the micromodel due to blockages, pressure difference is likely the primary contributing factor. Third, it is possible that the formation and propagation of the hydrate front occurred too rapidly to be observed. The video image sequencing was set to 30 images per second, implying that the growth rate of the hydrate front must have exceeded 6000 μm/s to encapsulate the CO_2 in the large pores. In comparison, previous studies reported much slower growth rates for CH_4 hydrates, with growth rates along the pore walls approximately 100 times faster (500 μm/s) than toward the pore center (7-8 μm/s) [57, 71]. In contrast, a CO_2 hydrate propagation speed of 6000 μm/s is more than tenfold the reported pore wall growth rates for CH_4 hydrates and 1000 times the reported pore center growth rates.

Staykova et al. [44] compared CH_4 and CO_2 reaction kinetics in bulk conditions and found that CO_2 reacts about 3 times faster than CH_4. The reaction rate was found to be inversely proportional to the particle size. Since the surface area increases with decreased particle size, the reaction rate must also increase with increased surface area. Due to the water-wet nature of the micromodel used in this master's project, water/brine covered the entire surface of the micromodel, resulting in a large interfacial area between CO_2 and water/brine. A higher reaction/growth rate is therefore to be expected. Moreover, the solubility of CO_2 in water is nearly 10 times greater than that of CH_4 in water (3.4 g/kg and 0.04 g/kg, respectively) [72]. The partial charges on the CO_2 molecular bonds enable interactions with polar water molecules, making CO_2 more soluble in water than CH_4. Consequently, more CO_2 was dissolved in the water phase, resulting in a larger surface area between CO_2 and water compared to CH_4. Furthermore, CO_2 is found to be the preferred hydrate former compared to CH_4, making CO_2 hydrates more thermodynamically stable [73].

Hydrate formation in the isolated CO_2 phase

Within the micromodel field of view, CO_2 existed either as a continuous CO_2 phase or as smaller isolated droplets surrounded by water. Agitation caused high saturations of CO_2 which resulted in short distances between the continuous CO_2 phase and areas with isolated CO_2 droplets. Due to Ostwald ripening, the continuous CO_2 phase often expanded towards the isolated CO_2. In other words, the continuous CO_2 phase grew at the expense of smaller CO_2 droplets. In areas where isolated CO_2 was not absorbed, the formation of hydrate film usually occurred simultaneously with the formation of hydrate film in the continuous CO_2 phase. Furthermore, the film thickening in the isolated phase seemed to be consistent with the thickening of the film in the continuous phase. Conversley, Katsuki et al. found that isolated gaseous methane bubbles enclosed in hydrate film seemed to disappear after formation, and concluded the bubble was consumed by crystal growth in the water phase. Contrary to these findings, the disappearance and consumption of the isolated CO_2 phase was not observed in this work. The isolated CO_2 remained the same size, indicating that the formation of hydrate crystals in the water phase was mainly controlled by the transportation of dissolved CO_2 in the water phase and not by mass diffusion through the hydrate film.

5.1.4 Hydrate formation and growth in the water phase

Hydrate formation in water-filled pores resulted in a crystalline hydrate morphology but this formation was rare due to the restricted supply of water. Agitation of the system caused a flow of CO_2 through the micromodel, which, due to its high mobility and sweep efficiency, displaced water and led to high saturations of CO_2.

The initial formation of hydrate crystals occurred in the vicinity of hydrate film in the CO_2 phase as seen in Figure 5.5. This is expected since the shortest distance between the hydrate-forming region and the water phase facilitates rapid mass transfer of CO_2 through the hydrate film. For experiments with deionized water, hydrate crystals were first observed at the CO_2-water interface near the pore walls in the smallest pores, simultaneously or milliseconds after the initial hydrate film formation in the CO_2 phase (Figure 5.5b). Hydrate formation in the larger water-filled pores initiated later than in the smaller pores but still within seconds of hydrate film formation. The hydrate crystals rapidly propagated into the center of the water-filled pores, indicating, either that a sufficient amount of CO_2 was dissolved in the pores, or that the hydrate film was not yet encapsulating the CO_2 allowing mass transfer of CO_2 through the film. Crystalline hydrate was also observed to form in the vicinity of isolated CO_2 as seen in Figure 5.5b. Indicating that the growth mechanism was mainly

controlled by transport of CO_2 through the hydrate film. Seconds after the initial crystalline hydrate formation, hydrate crystals also formed in pores not in cantact with hydrate film (yellow circle in Figure 5.5c). This is likely due to the supply of dissolved CO_2 in the water phase. CO_2 is highly soluble in water compared to other hydrate formers and is expected to form hydrates more readily in the water phase compared to systems with less soluble hydrate formers like CH_4 [68]. This mechanism was usually slower and harder to observe which can indicate that the growth mechanism was controlled by a combination of slow mass transport of CO_2 through the hydrate film and transport of dissolved CO_2 in the water phase. Almenningen et al. [56] reported similar results in their pore-scale study of CO_2 hydrate formation; Crystalline hydrate growth initiated at the curved CO_2-water interface and moved laterally into the water phase. Contrary to the findings in this thesis, they reported simultaneous crystalline hydrate growth in all pores, independent of pore size.

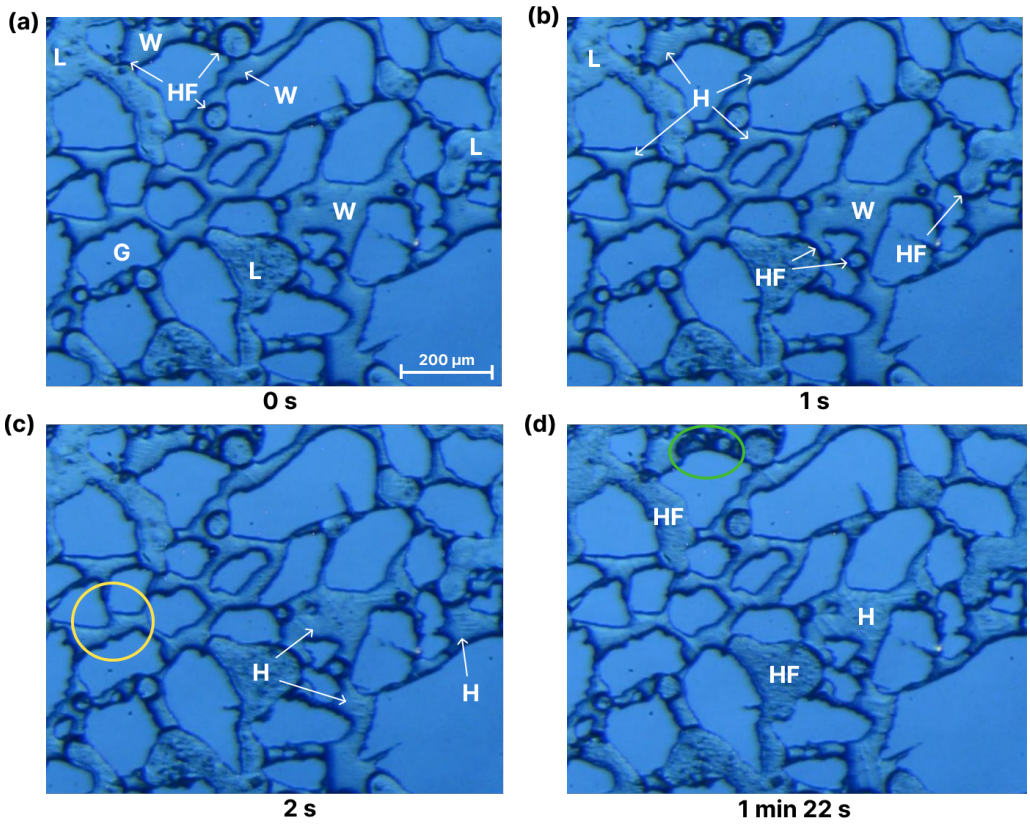

Figure 5.5: Crystalline hydrate formation in the water phase in experiment 13. The time-lapse from hydrate film formation (0 s) is given below the images. (a) Hydrate film formation (HF) at the CO_2-water interface along the pore walls. (b) Crystalline hydrate formation (H) in small water-filled pores in the vicinity of hydrate film. (c)-(d) Crystalline hydrate formation in the larger pores and in water-filled pores not in contact with hydrate film (yellow circle). The green circle shows porous hydrate film moving into the water phase, consuming the CO_2 in the crystalline hydrate phase.

5.1.5 Other observations

For all experiments, continuous movement of fluids was observed, indicating a redistribution and rearrangement of the hydrate crystals. Within 20 minutes of hydrate formation, the hydrate film was observed to move laterally into the water phase. Either observed as an expansion of the hydrate film or as dark coarse tendrils stretching from the hydrate film into the water phase. This indicates a conversion from crystalline hydrate in the water phase to coarse porous hydrate. This mechanism could be due to Ostwald ripening where larger crystals grow at the expense of smaller crystals in adjacent pores. The opposite was also observed. Within hours of hydrate film formation, the film slowly became more transparent. Hauge et al. [57] reported similar findings in their micromodel experiments. Both CO_2 and CH_4 hydrate film turned transparent and crystalline within hours of hydrate formation, indicating a transformation from hydrate film encapsulating the free gas phase, to a more stable crystalline hydrate phase. They concluded that the hydrate growth and redistribution could be explained by the water-wet nature of the micromodel; mobile water is supplied by capillary film flow on the water-wet surfaces resulting in hydrate growth and redistribution of fluids [57]. The transformation typically initiated at the center of the pore and propagated towards the pore walls. This behavior is likely because of a thinner hydrate film at the pore center compared to the pore edges. The thinner porous hydrate film facilitates the transport of water through the pores, thereby promoting further growth and transformation into crystalline hydrate. Lund et al. [74] proposed that after the initial hydrate formation, further formation was caused by dissociation and reformation of the hydrate film. This theory could explain the movement and conversion of the hydrate phases.

5.1.6 The effect of salinity

This section is a qualitative analysis of the salinity experiments to better understand the impact of salinity on hydrate formation patterns and pore-filling behavior within porous media. The formation mechanics and fluid behavior in the presence of these two salts, NaCl and $CaCl_2$, will be discussed. Six experiments for each salt was conducted with salt concentrations ranging from 1-5wt%.

NaCl

Table 5.3: Overview of experiments 6 and 8-12 performed using NaCl brine of different concentrations [C]. The results are obtained from the video image sequences 20 minutes after agitation.

Exp.	**[C]** [wt%]	**Pore-filling**	**Hydrate front**	**Crystalline hydrate**	**Induction time** [s]
6*	1	Yes	No	Yes	26
8	1	Yes	No	Yes	6
9	2	Yes	No	Yes	7
10	3	Yes	No	Some	7
11	4	Mostly	Some	No	11
12	5	Mostly	Some	No	11

* Agitated with no visible CO_2 in the system.

Experiments 6-12, summaized in table 5.3, were conducted using brine of varying NaCl salinities, while keeping the pressure and temperature constant at 75 bar and 3.5 °C, respectively. In all experiments, initial hydrate film formation occurred at the curved CO_2-water interface along the pore walls and at the interface of water droplets underneath the CO_2 phase. For low salinity experiments, the hydrate formation was uniform throughout the micromodel field of view. The formation initiated somewhat simultaneously with no distinct hydrate front observed as seen in Figure 5.6 (b)-(c). Within one minute of agitation, the hydrate film almost completely encapsulated the CO_2 phase and continued to thicken, leading to a darkening of the film from light gray to dark gray (Figure 5.6 (c)-(d)). Interestingly, low concentrations of NaCl appeared to promote hydrate film formation, resulting in a thicker and more uniform hydrate film compared to experiments conducted with deionized water. Previous research has suggested that small impurities, such as Na^+ and Cl^- ions, can serve as nucleation sites, promoting hydrate growth and reducing induction time. Despite salts being considered thermodynamic inhibitors, they can act as kinetic promoters at low concentrations by enhancing the formation rate [59, 75].

With increased salinity, the hydrate front became slightly more visible. While the hydrate film still encapsulated the CO_2 phase, there were more visible spots of CO_2 not encapsulated by the film in the larger pores. However, all six experiments exhibited pore-filling hydrate film behavior, indicating that the porous hydrate phase occupied the entire pore space and contacted the grains. Increased salinity also seemed to have a delaying effect on hydrate formation as the induction time increased with increasing salt concentration. These results coincides with the findings of Gauteplass et al. [15], who conducted core scale experiments to investigate the effect of salinity on hydrate formation. They observed that an increase in salinity from 3.5wt% to 5.0wt% resulted in a delay in hydrate formation and consequently, more CO_2 was injected.

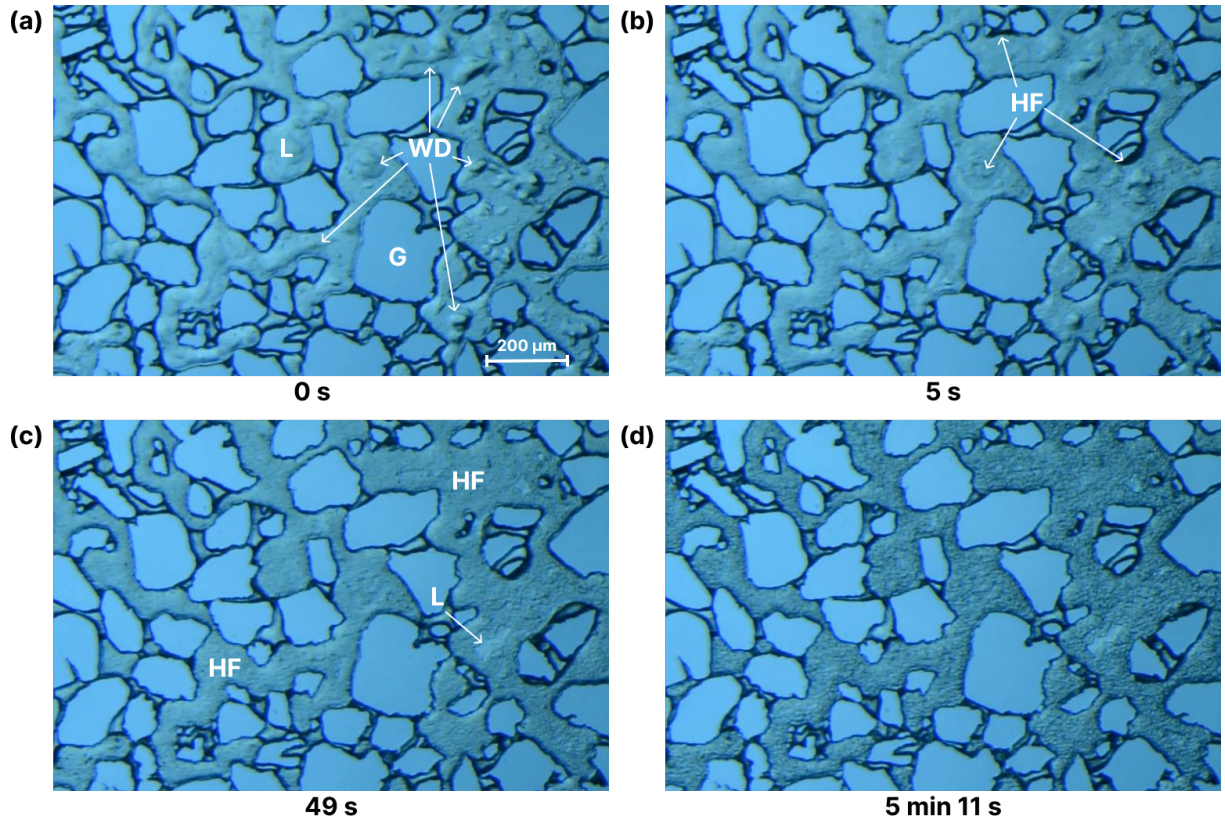

Figure 5.6: Uniform hydrate film formation in experiment 10 (3wt% NaCl). Time-lapse from hydrate formation (0 s) and is given below the images. (a) The micromodel before hydrate formation. Water droplets (WD) reside below the continuous CO_2 phase (L). (b) Hydrate film formation (HF) at the water-CO_2 interface in the continuous CO_2 phase. The film formation is almost uniform in all interfaces. Larger water droplets function as nucleation sites but there is no hydrate front. (c) Thickening of the hydrate film by consumption of water droplets and residual water. (d) Further film thickening.

In the low-salinity experiments, crystalline hydrate formed in all water-filled pores. Similar to no-salinity experiments, the formation was simultaneous to the hydrate film formation along the pore walls. The crystals initially formed in the vicinity of the continuous CO_2 phase and were first observed in the smaller pores. In larger pores, the formation was slower but still within seconds of film formation. The crystalline hydrate configuration appeared completely pore-filling and all CO_2 was consumed as seen in figure 5.7. For high-salinity experiments, no crystalline hydrate growth was observed within the first three hours of hydrate film formation, which is expected due to the inhibiting effect of salt. Hydrate crystals do not contain salt, as water is consumed for hydrate formation, salt will remain in the water phase and the salinity of the residual water increases, inhibiting further hydrate formation. Over time, ion diffusion and film flow from neighbouring water filled pores to the high-salinity water-filled pores will result in a decrease in the local salt concentration, thereby delaying the formation of crystalline hydrate in the water phase. Another reason for the delay could be the low solubility of CO_2 in saline water. Hydrate growth in the water phase is governed either by CO_2 transport through water, which is dependent on the dissolution of CO_2 in the water phase, or diffusion of CO_2 through hydrate film. Increased concentrations of salt lead to a decrease in CO_2 solubility, thereby restricting the availability of CO_2 in the water phase. Formation of crystalline hydrate through the diffusion of CO_2 from the hydrate film is a slower process, thus explaining the delaying effect of crystalline hydrate formation. Eventually the porous hydrate film turned transparent for all NaCl experiments, indicating a transformation from the porous hydrate film to a more stable crystalline hydrate phase.

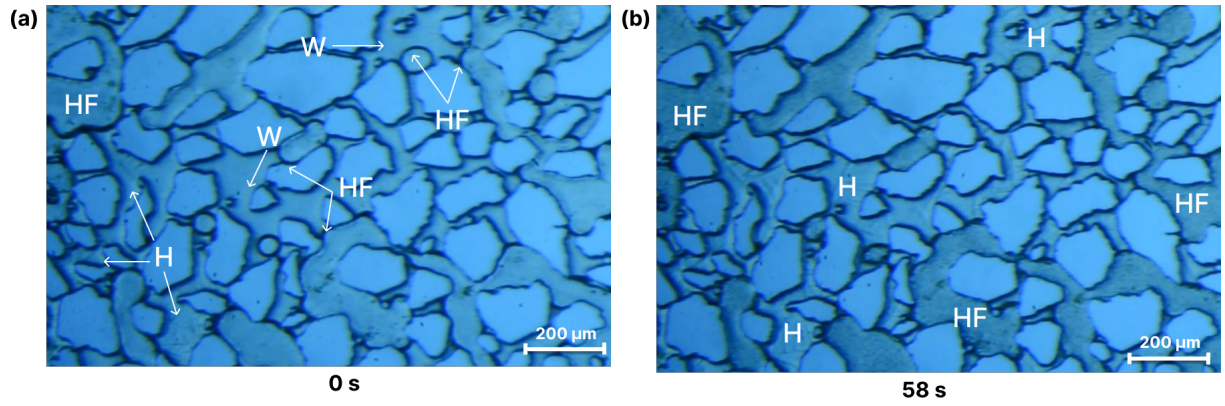

Figure 5.7: Massive hydrate formation in experiment 6. The time after the onset of hydrate formation is given below the images. The images show grains (G), liquid CO_2 (L), water (W), crystalline hydrate (H), and hydrate film (HF). Image (a) shows hydrate film forming uniformly in the liquid CO_2 phase and crystalline hydrate forming in the smaller pores, (b) shows further crystalline hydrate formation in the larger pores.

$CaCl_2$

Table 5.4: Overview of experiments 14-18 performed using $CaCl_2$ brine of different concentrations [C]. The results are obtained from the video image sequences 20 minutes after agitation.

Exp.	[C] [wt%]	Pore-filling	Hydrate front	Crystalline hydrate	Induction time [s]
14	1	Yes	No	Yes	5
15	2	Yes	No	Yes	25
16	3	No	Yes	No	25
17	4	Yes	Some	No	15
17_2*	4	Mostly	Some	No	50
18	5	Partially	Some	No	51

* Agitated with no visible CO_2 in the system.

Experiments 14-18, summarized in table 5.4, were conducted using brine of different $CaCl_2$ salinities, while keeping the pressure and temperature constant at 75 bar and 3.5 °C. All experiments exhibited the same initial hydrate film formation behavior. Formation of the hydrate film initiated at the curved CO_2-water interface along the pore walls and at the interface of water droplets residing underneath the CO_2 phase. The formation was observed as an expansion of the hydrate film, with a simultaneous darkening of the curved interface. Further hydrate growth was observed as rapid film propagation from the nucleation points into the CO_2 phase, encapsulating the liquid CO_2.

In contrast to the experiments conducted with NaCl brine, the observed hydrate formation mechanisms in $CaCl_2$ experiments were inconsistent. For instance, experiment 16 (3wt% $CaCl_2$) exhibited a distinct hydrate front as seen in figure 5.8c, whereas experiments with both lower and higher salinities displayed less visible hydrate fronts. The hydrate front propagated rapidly from the nucleation sites, but the growth quickly ceased, likely due to insufficient water supply. Despite the hydrate film appearing to contact the grains, large areas of visible CO_2 were observed in both large and small pores, the hydrate film is therefore not considered pore-filling. This could be due to a number of reasons. First, the unpredictability of the agitation method resulted in different drops in pressure for the experiments. If the difference in pressure before and after agitation was low, the driving force would be low, resulting in less hydrate formation. However, the pressure seems to be within the average value for the experiments (as seen in Appendix B). Second, the saline solution could be contaminated with foreign particles such as dust. While small contaminants might promote hydrate growth due to their large surface area, large particles can inhibit hydrate nucleation.

Experiments 17, 17_2, and 18 (4 and 5wt%, respectively) also exhibited hydrate fronts, although significantly less pronounced compared to experiment 16 (figure 5.8d-f). This was likely due to the inhibiting effect of salt and the salting out effect resulting in a slower hydrate formation process. Conversely, experiments 14 and 15 displayed no noticeable hydrate fronts and the hydrate film formation appeared uniform through the field of view.

Experiments 14, 15, 17, and 17_2 (1, 2, and 4wt%, respectively) exhibited pore-filling hydrate behaviour. However, experiment 18 (5wt%) was only partially pore-filling. The hydrate film was mostly grain contacting and appeared to occupy large portions of the pore space. However, significant areas with unconsumed CO_2 resided in the center of larger pores. The consumption of CO_2 decreased with increasing salinity, with the exception of experiment 16, resulting in larger areas of CO_2 not encapsulated by the hydrate film. There was a higher volume of unconsumed CO_2 in the pore space compared to the NaCl experiments with equivalent salinities. Furthermore, there was no correlation between increased salinity and induction time. The induction time for experiment 17, which was conducted with 4wt% brine, was faster than both experiment 15 and 16 which were conducted with 2wt% and 3wt% salinity brine, respectively. This could be attributed the difference in driving force (pressure) as discussed earlier or to the unpredictability of induction times due to their stochastic nature.

The crystalline hydrate formation for the $CaCl_2$ experiments was unpredictable. In the 1-2wt% $CaCl_2$ experiments, crystalline hydrate formation was observed in all water-filled pores, primarily near the continuous CO_2 phase where the hydrate film covered the curved CO_2-water interface. However, unlike NaCl experiments, the simultaneous formation of hydrate film and crystalline hydrate was only observed in experiment 14 (1wt%). In experiment 15 (2wt%), although crystalline hydrate formation occurred within seconds of hydrate film formation in the smallest pores, the formation was slower compared to the NaCl experiments of the same salinity. In contrast, for 3-5wt% $CaCl_2$, crystalline hydrate formed after three hours. Furthermore, compared the NaCl experiments, less porous hydrate film transformed into crystalline hydrate for high-salinity $CaCl_2$ experiments. The difference between the NaCl and the $CaCl_2$ experiments could be attributed several factors. First, as discussed in section 2.6, the inhibiting effect of salts increases with the ion charge, and thus, Ca^{2+} is expected to have a more pronounced inhibiting effect compared to Na^{+}. Second, due to the large charge density of Ca^{2+} ions and strong Coulombic forces between water molecules and Ca^{2+} ions, $CaCl_2$ is known to have a stronger salting-out effect than NaCl, resulting in a stronger reduction in CO_2 solubility.

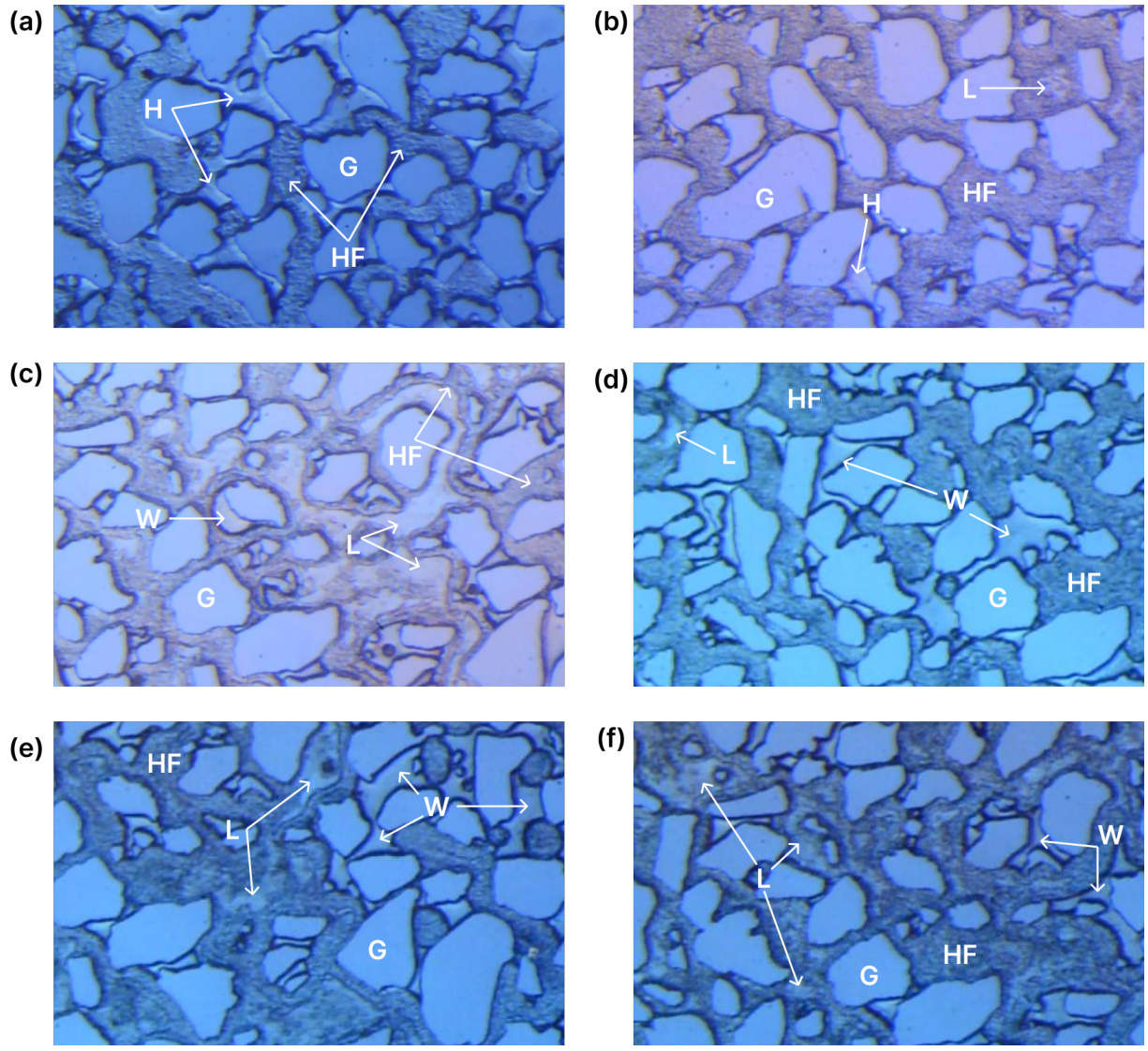

Figure 5.8: Images from hydrate formation experiments 14-18 conducted with varying $CaCl_2$ concentrations. (a) Experiment 14 (1wt% $CaCl_2$). Hydrate film formation in the continuous CO_2 phase and crystalline hydrate formation in the water phase. The entire CO_2 phase is encapsulated by hydrate film. (b) Experiment 15 (2wt% $CaCl_2$). Hydrate film formation in the continuous CO_2 phase, and crystalline hydrate formation in the water phase. Small areas with visible liquid CO_2. (c) Experiment 16 (3wt% $CaCl_2$). Hydrate film formation in the continuous CO_2 phase and a distinct hydrate front. There was no crystalline hydrate formation in the water phase. Large areas with visible liquid CO_2. (d)-(e) Experiments 17 and 17_2 (4wt% $CaCl_2$). Hydrate film formation in the continuous CO_2 phase and a slightly visible hydrate front. There was no crystalline hydrate formation in the water phase. Some areas with visible liquid CO_2 are not encapsulated by the film. (f) Experiment 18 (5wt% $CaCl_2$). Porous hydrate film formation in the continuous CO_2 phase with visible CO_2. No crystalline hydrate formation in the water phase.

5.2 Quantitative analysis

In this section, a quantitative analysis of the data obtained from experiments 1-20 is presented. The effect of initial water saturation, temperature, and salinity will be discussed to estimate the potential of utilizing CO_2 hydrates as a sealing mechanism for CO_2 storage. Initial water saturations, porous hydrate saturations, crystalline hydrate saturations, and total hydrate saturations were estimated by analyzing video image sequences in the image analysis tool, ImageJ.

5.2.1 The effect of water saturation

The effect of initial water saturation on hydrate formation was investigated for both no-salinity experiments and salinity experiments. Experiments 1-5, 13, 19, and 20 were performed using deionized water under constant pressure with varying temperatures, ranging from 2.0-5.0 °C. Table 5.5 summarizes estimated initial water saturation (S_{wi}), porous hydrate saturation (S_{HF}), and crystalline hydrate saturation (S_H) for experiments 1-5, 13, 19, and 20.

Table 5.5: Overview of experiments 1-5, 13, 19, and 20 performed using deionized water. S_{wi} is the initial water saturation before hydrate formation, S_{HF}, S_H, S_{Htot} is the porous hydrate film saturation, crystalline hydrate saturation, and total hydrate saturation, respectively. ΔS_{HF}, ΔS_H, and ΔS_{Htot} are uncertainties in the saturations.

Exp.	ΔT [°C] $\pm$ 0.2	S_{wi} [frac.]	ΔS_w $\pm$	S_{HF} [frac.]	ΔS_{HF} $\pm$	S_H [frac.]	ΔS_H $\pm$	S_{Htot} [frac.]	ΔS_{Htot} $\pm$
1	5.0	0.306	0.009	0.579	0.007	0.114	0.001	0.693	0.046
2	5.0	0.298	0.027	0.544	0.031	0.090	0.005	0.634	0.060
3	5.0	0.326	0.021	0.589	0.045	0.141	0.005	0.730	0.041
5	3.5	0.407	0.007	0.572	0.022	0.284	0.002	0.856	0.013
13	3.5	0.428	0.006	0.654	0.025	0.276	0.002	0.931	0.049
19	2.0	0.481	0.063	0.574	0.044	0.382	0.013	0.955	0.046
20	5.0	0.501	0.048	0.565	0.035	0.395	0.011	0.960	0.029

Tables 5.6 and 5.7 summarizes the measured initial water saturation and hydrate saturations of the NaCl and $CaCl_2$ experiments, respectively. The experiments were conducted under constant pressure and temperature (75 bar and 3.5°C).

Table 5.6: Overview of experiments 6 and 8-12 performed using NaCl brine of different salinities (c). S_{wi} is the initial water saturation before hydrate formation, S_{HF}, S_H, S_{Htot} is the hydrate film saturation, crystalline hydrate saturation, and total hydrate saturation, respectively. ΔS_{HF}, ΔS_H, and ΔS_{Htot} is the uncertainties in saturations.

Exp.	c [wt%]	S_{wi} [frac.]	ΔS_w ±	S_{HF} [frac.]	ΔS_{HF} ±	S_H [frac.]	ΔS_H ±	S_{Htot} [frac.]	ΔS_{Htot} ±
6	1	0.590	0.010	0.618	0.006	0.314	0.003	0.959	0.014
8	1	0.376	0.006	0.798	0.005	0.144	0.001	0.942	0.008
9	2	0.391	0.007	0.717	0.008	0.155	0.002	0.872	0.015
10	3	0.385	0.007	0.672	0.007	0.160	0.002	0.832	0.014
11	4	0.363	0.007	0.764	0.008	0	0	0.764	0.008
12	5	0.334	0.007	0.658	0.007	0	0	0.658	0.007

Table 5.7: Overview of experiments 14-18 performed using $CaCl_2$ brine of different salinities (c). S_{wi} is the initial water saturation before hydrate formation, S_{HF}, S_H, S_{Htot} is the hydrate film saturation, crystalline hydrate saturation, and total hydrate saturation, respectively. ΔS_{HF}, ΔS_H, and ΔS_{Htot} is the uncertainties in saturations.

Exp.	c [wt%]	S_{wi} [frac.]	ΔS_w ±	S_{HF} [frac.]	ΔS_{HF} ±	S_H [frac.]	ΔS_H ±	S_{Htot} [frac.]	ΔS_{Htot} ±
14	1	0.348	0.024	0.720	0.028	0.145	0.006	0.865	0.054
15	2	0.322	0.021	0.821	0.030	0.028	0.001	0.849	0.052
16	3	0.311	0.010	0.661	0.010	0.006	0.001	0.667	0.021
17	4	0.365	0.054	0.703	0.053	0	0	0.703	0.052
17_2	4	0.371	0.048	0.693	0.050	0	0.0	0.693	0.050
12	5	0.350	0.037	0.691	0.044	0	0	0.701	0.044

Experiments conducted with destilled water

Figure 5.9 illustrates the relationship between initial water saturation and hydrate saturation for experiments 1-5, 13, 19, and 20. The crystalline hydrate saturation increases with increasing water saturation, which was to be expected from the qualitative analysis of hydrate growth. Given that crystalline hydrates initially form in the water phase, a higher S_{wi} results in a higher crystalline hydrate saturation. In contrast, the porous hydrate saturation remains more or less the same with increasing water saturation but the trend is weak ($R^2 = 0.034$). Consequently, the total hydrate saturation increases with increased water saturation. There seems to be a strong correlation between crystalline hydrate growth and initial water saturation ($R^2 = 0.989$), which results in a strong correlation between the overall hydrate saturation and initial water saturation ($R^2 = 0.946$).

Although no visible evidence of increased hydrate film growth was observed, it is possible that the hydrate film thickened due to the sufficient water supply, which may not have been visible with the limited microscope resolution. In comparison, Ersland et al. [76] investigated gas permeability in CH_4-CO_2 exchange systems within porous media. They found that increased initial water saturation led to an increase in hydrate saturation and reduced gas permeability. Similarly, Zhao et al. [77] investigated the effect of initial water saturation on CO_2 storage capacity and leakage ratio in core plugs and found that the final hydrate saturation increased with increased initial water saturation. Although, initial water saturations above 0.26 were sufficient to form a hydrate cap, preventing leakage of CO_2, the CO_2 leakage ratio decreased with increasing hydrate saturation. Pore-filling hydrates initiate at the grain surface of sediments and grow outward into the pore space reducing the fluid flow and permeability. Pandey et al. found that for $S_{wi} = 0.35$ or above, resulted in pore-filling hydrates. In this work, water saturations of $S_{wi} = 0.32$ or above, resulted in pore-filling hydrate film. However, higher initial water saturations resulted in more rapid transformation from hydrate film to solid non-porous crystalline hydrate, likely due to the sufficient supply of water. This observation supports the theory that higher water saturation leads to thicker and more pore-filling hydrate films.

The study of hydrate saturation with respect to initial water saturation has certain limitations. First, both initial water saturations and hydrate saturations were estimated from images of the micromodel, covering approximately 1% of its area, thereby neglecting saturation variations within the micromodel caused by water displacement during agitation. Second, it was assumed that wetting water films covered the grain surfaces due to the water-wet nature of the micromodel, but these films could not be observed due to microscope resolution limitations. Thus, the water film was not considered in water saturation estimations. Third, the thickness of the hydrate film could not be estimated because of the limiting resolution of the microscope. Therefore, the hydrate film saturations are only estimations. In practical terms, the hydrate film saturations are likely to be lower with higher concentrations of unconsumed CO_2 residing underneath the film.

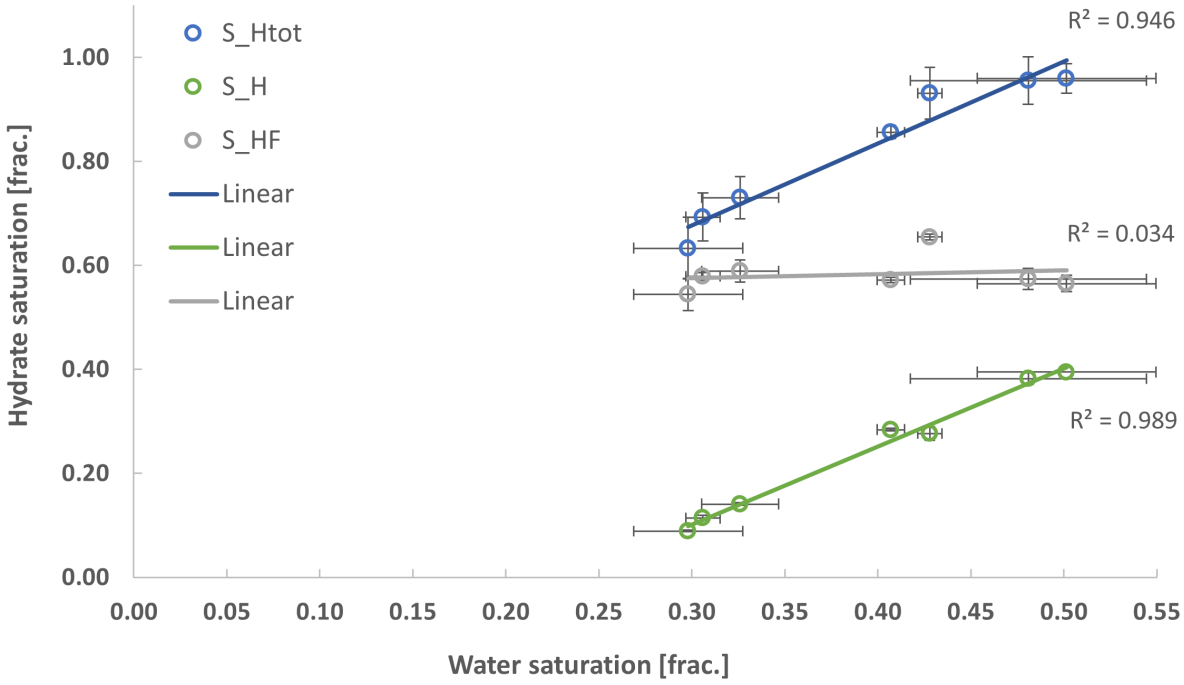

Figure 5.9: Hydrate saturation as a function of initial water saturation for experiments 1-5, 13, 19, and 20. The green data points represent the crystalline hydrate saturation for each experiment. The blue represents the total hydrate saturation and the gray represents the porous hydrate saturation within the micromodel field of view. The solid linear trend lines for total, porous, and crystalline hydrate saturation The correlation.

For experiments 1-5, hydrate film growth was estimated by measuring the gray scale of the video image sequences. In practice, the gray scale value decreases with increasing darkness of the film. However, for the purpose of representation in this study the gray scale values are presented as increasing with darkness. An increase in gray scale is therefore interpreted as hydrate film thickening and vertical growth. Figure 5.10 shows the increase in gray scale over time from the onset of hydrate formation. There seems to be a relationship between initial water saturation and hydrate growth, the gray scale increases with increasing initial water saturation for the experiments: 2 (0.298) < 1 (0.306) < 3 (0.326) < 5 (0.407). This indicates that the hydrate film thickens with increased water saturation. Almenningen et al. [68] conducted micromodel experiments to investigate the CH_4/CO_2 phase transition in porous media and discovered that the thickness of the hydrate film varied from pore to pore based on the availability of water and gas/liquid CO_2. Interestingly, even when the initial water saturation exceeded 0.65, hydrate formation was still predominantly governed by excess gas/liquid CO_2, leading to complete consumption of water. The hydrate film grew thicker in pores where water was readily available and continued to thicken until all water was consumed, supporting the theory that hydrate film thickening is strongly dependent of initial water saturation.

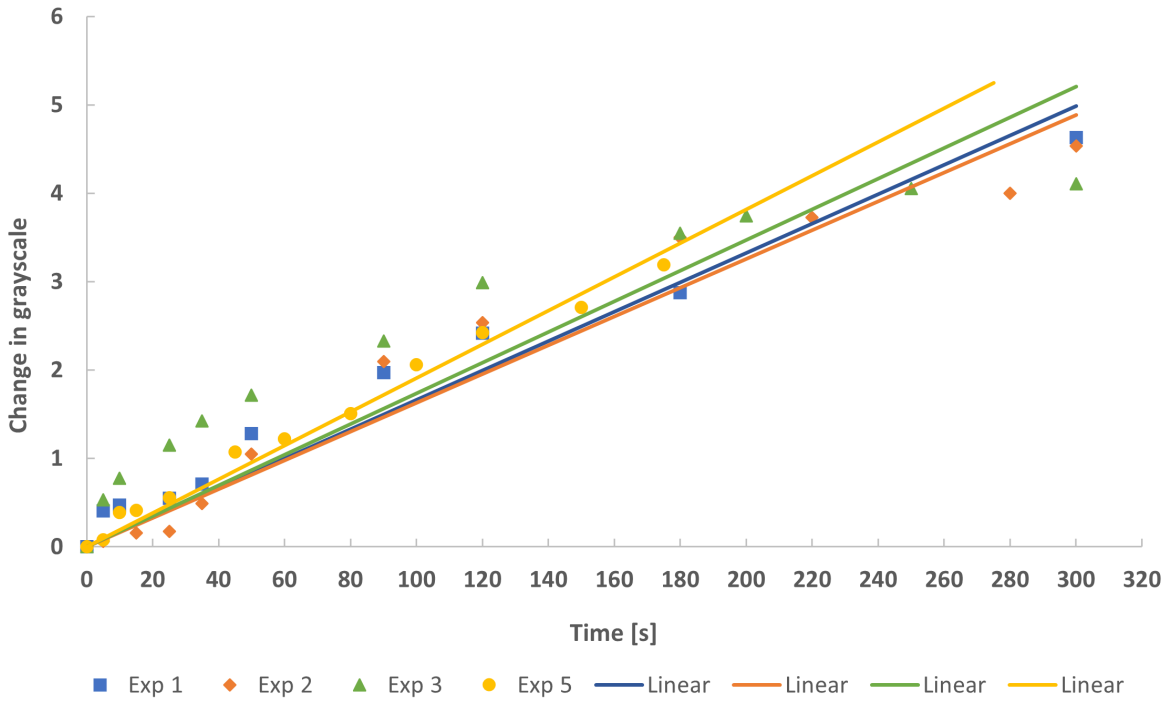

Figure 5.10: Change in gray scale over time for experiments 1-5. The change in gray scale was plotted against time to study the hydrate film growth.

Quantifying the growth was challenging due to three main reasons. First, the hydrate formation was rapid and no distinct hydrate front was observed. There are two possible explanations, either, there was no hydrate front and hydrate film formation was uniform through the field of view. Or the hydrate front was too fast to observe. Second, the quality of the images varied due to light disturbances from the surroundings. The difference was observed not only between different experiments but also within the same experiments. In some cases, the disturbances in lighting conditions hindered accurate quantification of gray scale values. Third, movement from the surrounding equipment such as the refrigerated bath circulator and the pump system, caused movement of the water in the inner cooling chamber. The movement caused the area of focus to shift slightly from one second to the next. Therefore, the area of measurement at one data point might be slightly different for the next data point. Hydrate growth was therefore only quantified for the first five experiments.

The relationship between the initial water saturation and induction time for experiments 1-5, 13, 19, and 20 is illustrated in Figure 5.11. The induction time in this work is defined as the elapsed time from agitation to the first visible sign of hydrate formation. The induction time decreases with increasing water saturation with the exception of experiment 20 which had the highest water saturation. The Figure illustrates both linear and power trend lines, with the linear trend being the best fit for the data points. Upon removing the outlier, the fit improves significantly from 0.602 to 0.927. The induction time decreases with increasing water saturation and both the power law trend ($R^2 = 0.944$) and the linear trend ($R^2 = 0.927$) give a good correlation between water saturation and induction time illustrated by Figure 5.12.

The observations in this work are in accord with Wang et al. who investigated the induction time of methane hydrates in porous media and found that when initial water saturations increased from 30% to 70%, the induction times decreased. However, when the initial water saturations increased from 70% to 90%, the induction time increased due to the poor solubility of CH_4 in water, resulting in limited contact between methane and water molecules. Conversely, Benmesbah et al. found no clear correlation between initial water saturation and induction time. Induction times are generally known to be unpredictable due to their stochastic nature and are said to be a function of time-dependent variables such as gas consumption, surface area, agitation, history of the water, and the presence of foreign particles [23]. The reason for the increased induction time in experiment 20 could be due to a decrease in driving forces such as increased temperature or the pressure difference before and after agitation, or it could be attributed the stochastic and unpredictable nature of hydrate nucleation.

Induction times can provide an indication of how quickly CO_2 can be trapped in a hydrate structure under specific conditions. Short induction times are favorable for CO_2 sequestration as they lead to a rapid formation of the hydrate cap. The formation of a hydrate cap is crucial for CO_2 sequestration within or below the hydrate stability zone, as it prevents further CO_2 migration and reduce CO_2 leakage [15, 77]. However, if the induction time is to short, pore-filling hydrates can restrict the contact between pore water and CO_2, hindering further hydrate formation. Zhao et al. [77] found that the time of hydrate pore plugging was only a few minutes after the induction period of hydrate formation, concluding that induction time is the main factor to determine the onset of plugging. They also found that initial water saturation was the key parameter in determining whether sediment layers have the potential to form a pore plugging hydrate cap. The induction times observed in this work are short (under 1 minute), indicating good potential for fast formation of a hydrate seal within the porous media. However, further experiments should be conducted to examine induction time with respect to reduction in fluid permeability.

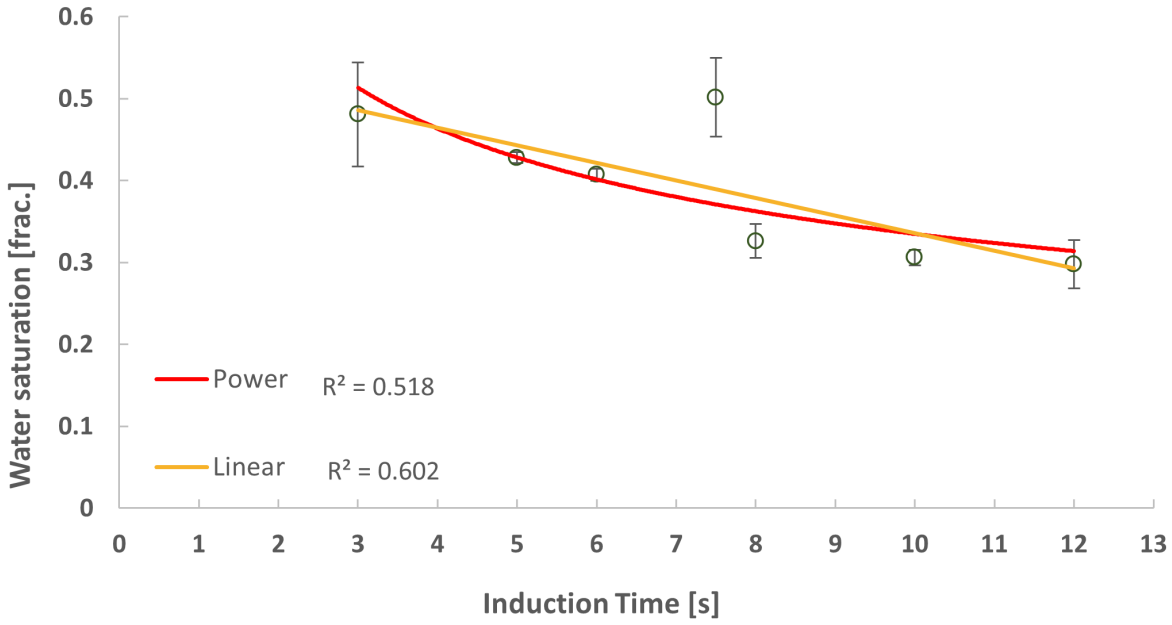

Figure 5.11: Induction time as a function of water saturation for experiments 1-5, 13, 19, and 20, with both power (red) and linear (orange) trends.

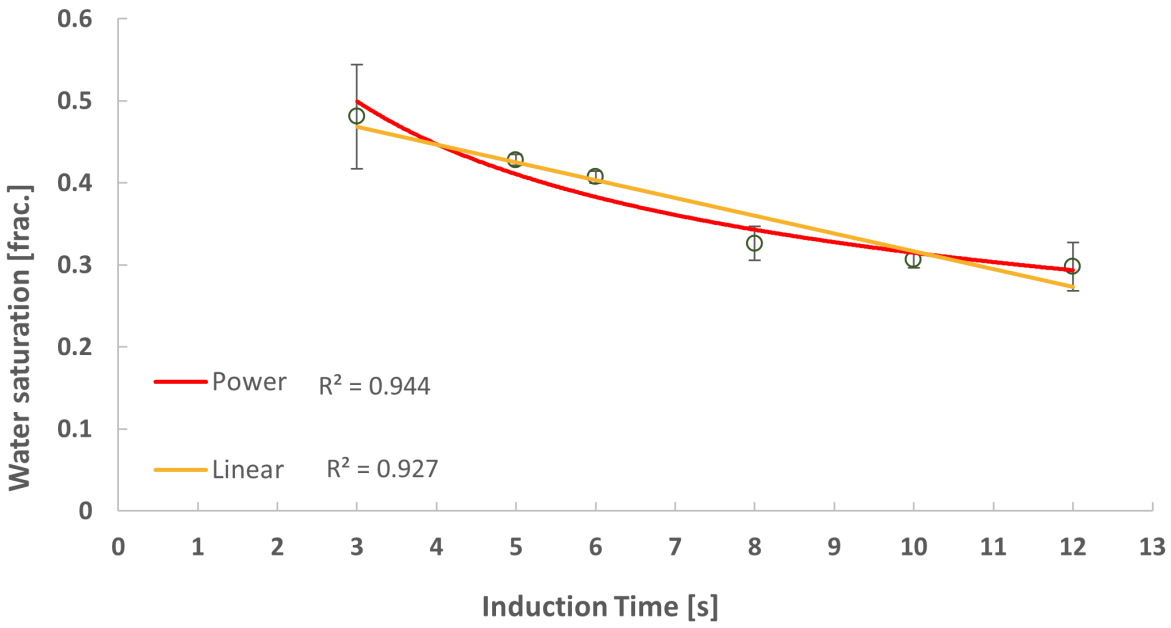

Figure 5.12: Induction time as a function of water saturation for experiments 1-5, 13, and 19, with both power (red) and linear (orange) trends. The outlier has been removed for a better trend line fit.

Experiments conducted with brine

Figures 5.13 and 5.14 illustrates the relationship between initial water saturation and hydrate formation for the NaCl, and $CaCl_2$ experiments, respectively. Only the total hydrate saturation is included due to the low crystalline hydrate saturations in these experiments. For the NaCl experiments the hydrate saturation increases with increased water saturation and the relationship shows a good positive correlation of R^2=0.702. Coversley, for the $CaCl_2$ experiments the total hydrate saturation seems to decrease with increased initial water saturation but no clear trend is observed and the linear correlation is poor (R^2=0.031).

Experiment 8, conducted with 1wt% NaCl brine, shows a significantly higher hydrate saturation (0.942) compared to its initial water saturation (0.376). In contrast, experiments 9 and 10, both with higher initial water saturations of 0.391 and 0.385, respectively, exhibited lower hydrate saturations than experiment 8. By removing the outlier (experiment 8) the correlation is further improved and increases from 0.702 to 0.995. However, the hydrate saturations could be affected by other parameters such as salinity. Small impurities such as salt ions can promote hydrate growth by functioning as nucleation sites for hydrate formation. In the case of experiment 8, which was conducted with 1wt% brine, the low salt concentration

and dissolved ions likely had a promotional effect on hydrate nucleation and formation. This theory is further supported when comparing the total hydrate saturation for the low-salinity NaCl-experiments (table 5.6) to the deionized-water experiments (table 5.5) performed under the same thermodynamic conditions. Both experiments 8 (1wt%) and 9 (2wt%) with initial water saturations of 0.376 and 0.391, respectively, had higher hydrate saturations (0.942 and 0.872, respectively) than experiment 5, which had a higher initial water saturation of 0.407 and total hydrate saturation of 0.856. Furthermore, the correlation between initial water saturation and hydrate formation is stronger for the experiments conducted with deionized water, indicating that the salinity is a confounding variable. Thus, because there are too many variables and few data points to classify experiment 8 as an outlier, the correlation seems plausible. The effect of salinity and initial water saturation on hydrate formation will be further discussed in section 5.2.3.

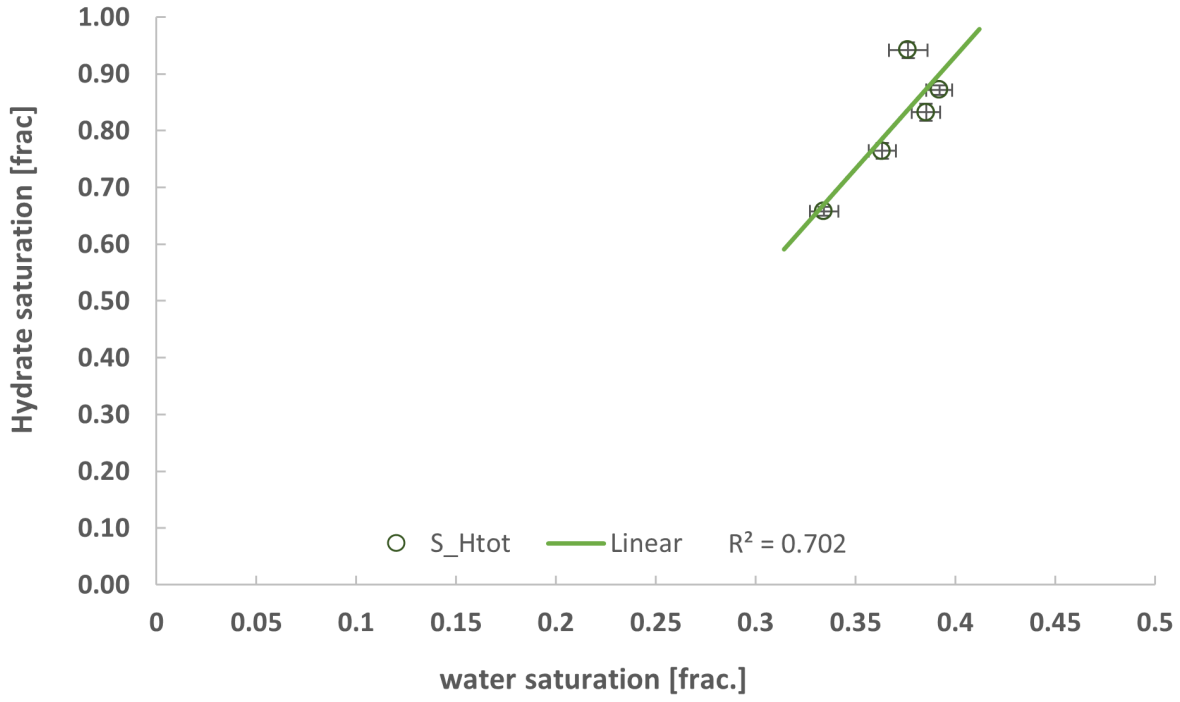

Figure 5.13: Hydrate saturation as a function of water saturation for experiments conducted with NaCl brine. The linear trend line shows the correlation between the two variables.

Similar observation were made in the $CaCl_2$ experiments. Experiment 16 differs significantly from the other experiments and removing it from the data set improved the correlation significantly (from 0.031 to 0.543), but the correlation remains poor. This is in contrast to the deionized water and NaCl experiments, where there was a strong correlation between initial water saturation and hydrate formation. These results suggest that experiments 14-18 are strongly influenced by a different variable. Considering that $CaCl_2$ is considered a stronger hydrate inhibitor compared to NaCl, an increase in salinity is expected to have a bigger effect on hydrate formation than that of NaCl. However, experiment 14 conducted with 1wt% $CaCl_2$ solution had an initial water saturation of 0.348 and a total hydrate saturation of 0.865 which is higher than experiment 5 (deionized water), which had a higher initial water saturation ($S_{wi} = 0.407$) and a total hydrate saturation of 0.856. Although this could indicate that the low salt concentration had a promotional effect on hydrate formation, the $CaCl_2$ data set show considerable variations in hydrate saturation with regard to both initial water saturation and salinity and it is therefore challenging to reach a definite conclusion.

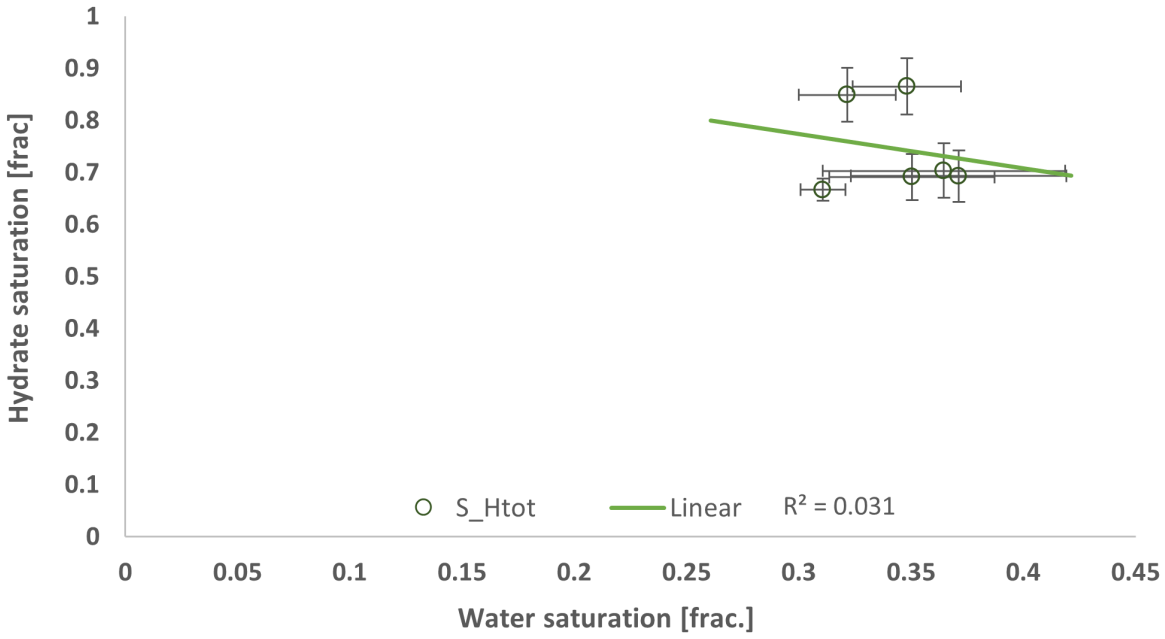

Figure 5.14: Hydrate saturation as a function of water saturation for experiments with $CaCl_2$ brine. The linear trend line shows a poor correlation between the two parameters (R^2=0.031).

5.2.2 The effect of Temperature

The effect of temperature was investigated in experiments 1-5, 13, 19, and 20. The temperature ranged from 2.0-5.0 °C while the pressure was kept constant at 75 bar. Figure 5.15 illustrates the relationship between experimental temperature and hydrate saturations for experiments 1-5, 13, and 19. Experiment 20 is considered an outlier and is excluded from the data set. The crystalline hydrate saturation decreased with increasing temperature, while the porous hydrate saturation remained more or less constant, resulting in an overall reduction in total hydrate saturation. However, the relationship between hydrate film formation and temperature is weak (R^2=0.071). Nevertheless, there is a strong correlation between the decrease in crystalline hydrate formation and the increase in temperature, resulting in an overall strong correlation between temperature and the total hydrate saturation (R^2=0.842).

The strong correlation between temperature and the amount of crystalline hydrate (R^2 = 0.962) could be explained by the solubility of CO_2 in the water phase. As temperature decreases, the solubility of CO_2 increases, leading to a greater availability of CO_2 for hydrate formation in the water phase. While the relationship between temperature and total hydrate saturation is strong, it is not as strong as the correlation between initial water saturation and total hydrate saturation ($R^2 = 0.946$). This could be due to a number of factors. First, the initial water saturation varied between 0.29-0.50 and increased with decreasing temperature. Seeing as crystalline hydrate initially only forms in the water phase, an increase in the initial water saturation would lead to an increase in the crystalline hydrate saturation, and consequently, the total hydrate saturation. Furthermore, experiment 20 is not considered an outlier when studying the effect of initial water saturation on hydrate saturation because its high initial water saturation seems highly correlated to the final hydrate composition. This suggests that water is the limiting factor, contributing more significantly to the increase in total hydrate formation than the effect of temperature. The agitation method itself could also influence the experiments. The pressure pulse induced by agitation causes a redistribution of fluids and renewal of the water-CO_2 interfaces. The pressure drop was not equal for each experiment and may have resulted in a difference in the renewal of the interfacial areas. Additionally, the difference in pressure before and after agitation was not equal, a higher differential pressure would likely result in a stronger driving force for hydrate formation.

The high correlation between temperature and hydrate saturation support the theory that lower temperature and degree of subcooling affects the final hydrate saturation. However, due to the number of variables present it is challenging to draw definite conclusions from the data. Further investigation and controlled experiments are necessary to establish a clearer understanding of the effect of temperature on hydrate formation.

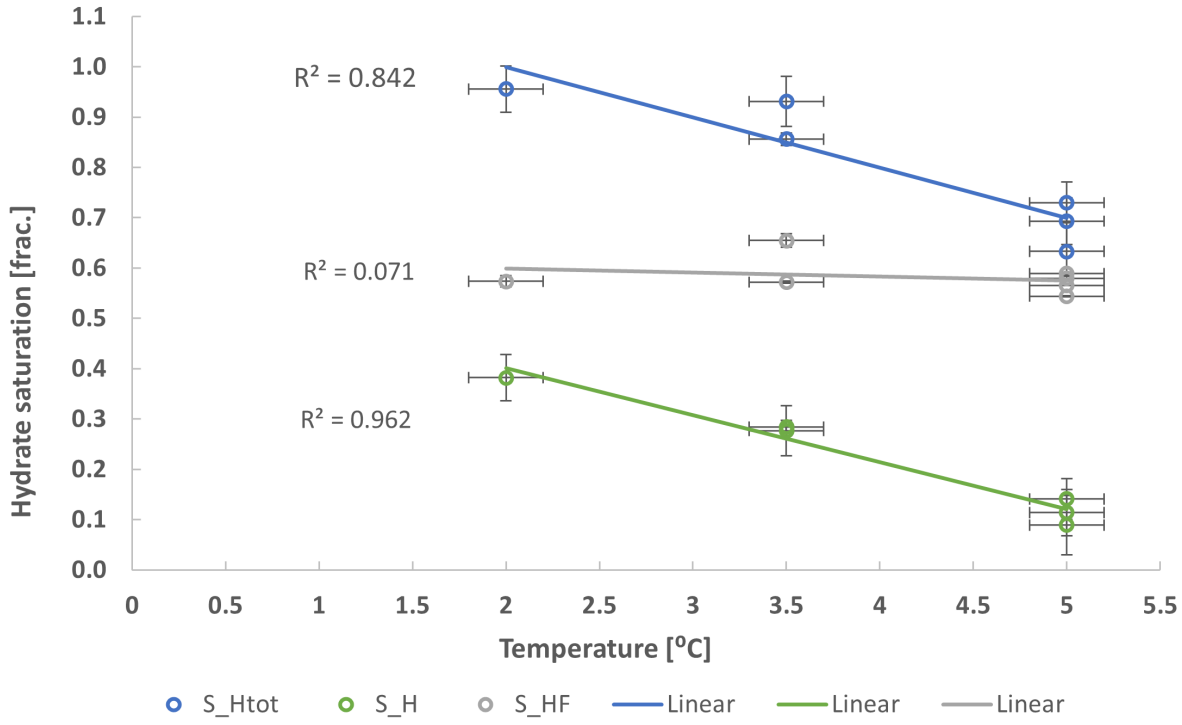

Figure 5.15: A representation of the correlation between temperature and hydrate saturation. The blue line represents the total hydrate saturation, the orange represents the crystalline hydrate saturation and the blue line represents the total hydrate saturation.

The effect of temperature with respect to induction time for experiments 1-5, 13, 19, and 20 was also investigated. The induction time increases with increasing temperature. Both linear and power trend shows a strong correlation of $R^2 = 0.751$ and $R^2 = 0.797$, respectively. The observations in this work coincides with previous research, which has shown that lower experimental temperatures results in shorter induction times and promote growth of a more stabilized pre-hydrate structures [15, 78]. As previously explained, lower temperatures promote solubility of CO_2 in the water phase, increasing the contact area between water and CO_2 which in turn promotes faster hydrate nucleation. The increase in induction time with increased temperature could therefore be attributed the increased solubility of CO_2. While the correlation between initial water saturation and induction time shows a better correlation

of 0.944 (power trend), experiment 20 which is considered an outlier with respect to initial water saturation, is not considered an outlier with respect to temperature. This might indicate that the induction time is more strongly affected by the degree of subcooling. Induction times plays a crucial role in estimating how quickly CO_2 can be trapped in a hydrate structure under specific conditions. In addition, short induction times are essential for converting the upward flow of CO_2 into solid hydrates before the migration front escapes the GHSZ [16]. The induction times observed in this thesis are very short but it is unclear whether it is due to the sufficient subcooling or initial water saturation. Therefore, induction times should be researched further in order to estimate the potential of utilizing CO_2 hydrates in carbon storage.

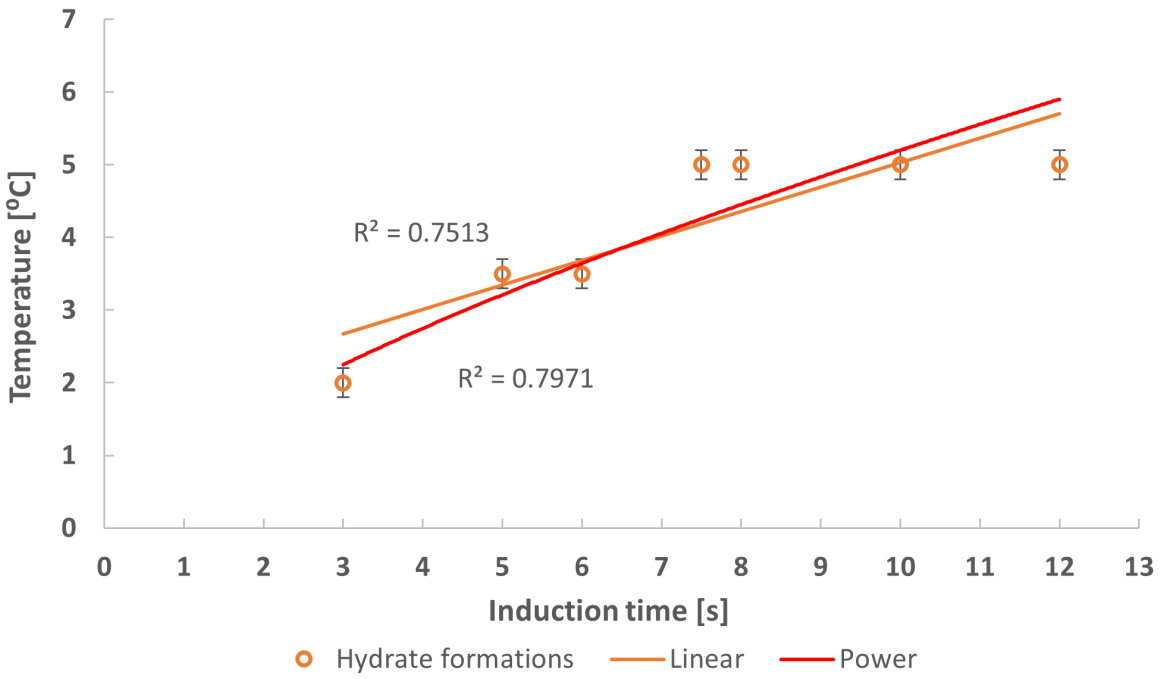

Figure 5.16: Hydrate induction time as a function of temperature for experiments 1-5, 13, 19, and 20 with both linear and power trends.

5.2.3 The effect of salinity

Experiments 6-12 were conducted using NaCl-brine, while experiments 14-18 were conducted using $CaCl_2$-brine. The salinity ranged from 1-5wt% and the experimental pressure and temperature were kept constant for all experiments. Figures 5.17 and 5.18 shows the relationship between hydrate film saturation, crystalline hydrate saturation, and total hydrate saturation with respect to the NaCl and $CaCl_2$ concentrations, respectively. Experiment 16 was excluded from the $CaCl_2$ data set due to its irregular formation behavior and low hydrate saturation.

In the NaCl experiments (figure 5.17) the hydrate film saturation stays constant with increasing salinity and there is no observable correlation between the two ($R^2 = 0.011$). In contrast, the relationship between crystalline hydrate saturation and salinity seems correlated ($R^2 = 0.691$). The crystalline hydrate saturation decreases with increasing NaCl concentration and for high-salinity experiments, there is no crystalline hydrate formation in the water phase. Consequently, the total hydrate formation decreases with increasing salinity and the relationship seems to be strongly correlated ($R^2 = 0.980$). In contrast, in the $CaCl_2$ experiments, the hydrate film saturation decreases with increased salinity. Although the correlation is weak (0.340), it is significantly stronger compared to NaCl ($R^2 = 0.011$). Similarly, the crystalline hydrate saturation also decreases with increased salinity and the relationship appeared to be slightly more correlated ($R^2 = 0.728$) than for NaCl. However, the correlation between total hydrate saturation and salinity is slightly lower compared to NaCl ($R^2 = 0.927$ and $R^2 = 0.980$, respectively).

As discussed in section 5.2.1 the initial water saturation plays a significant role in predicting the hydrate composition and saturation within porous media. To analyze the effect of both initial brine saturation and salinity on hydrate formation and to compare the two variables, combination graphs were used. These graphs, represented in Figures 5.19 and 5.20, illustrate the relationship between hydrate saturation, salinity, and initial brine saturation. In these graphs, the primary y-axis (left side) represents hydrate saturation, while the secondary y-axis represents salt concentration (right side). The salinity of each experiment is indicated by the yellow line. The bars in the graph represent hydrate film saturation (gray), crystalline hydrate saturation (green), and total hydrate saturation (blue) at varying initial initial brine saturations (x-axis) for each experiment.

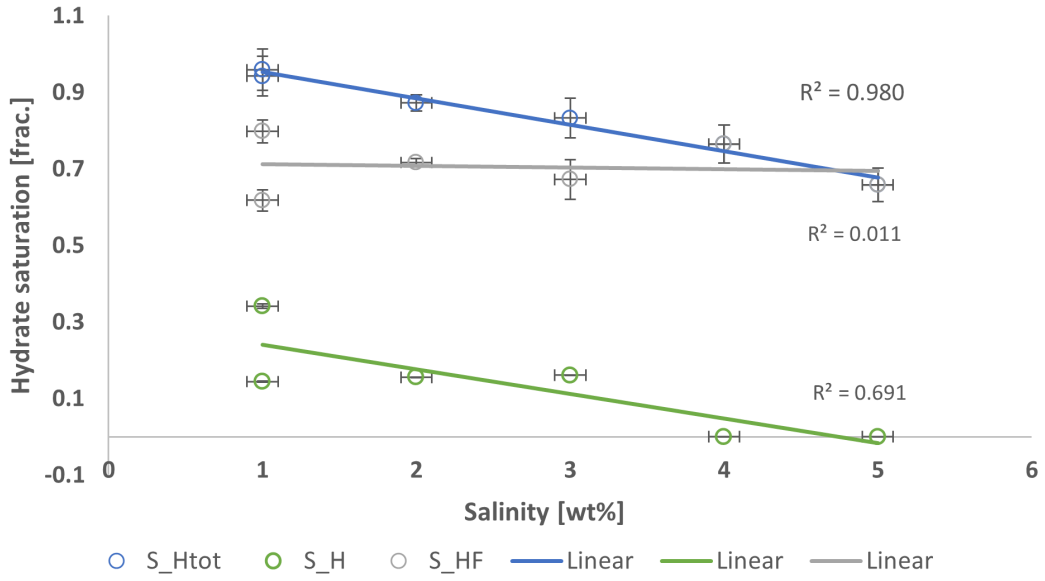

Figure 5.17: Hydrate saturation as a function of water salinity for NaCl experiments with linear trend lines. The blue, gray, and green data points represents the total hydrate saturation, the porous hydrate film saturation, and the crystalline hydrate saturation, respectively.

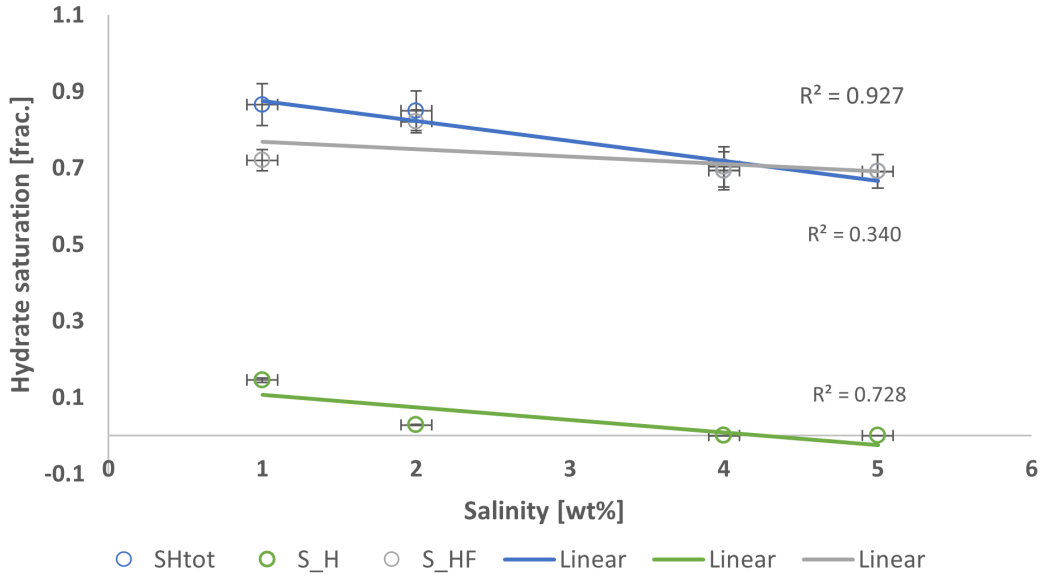

Figure 5.18: Hydrate saturation as a function of salinity for $CaCl_2$ experiments with linear trend lines. The blue, gray, and green data points represents the total hydrate saturation, the porous hydrate film saturation, and the crystalline hydrate saturation, respectively.

In the NaCl experiments, the crystalline hydrate saturation decreases not only with increasing salinity but also with decreasing initial brine saturation as seen in figure 5.19. This is evident when comparing experiments 6 and 8, both conducted with 1wt% NaCl brine. Experiment 6 had an initial brine saturation of 0.590, while experiment 8 had an initial brine saturation of 0.376. This difference in initial brine saturation resulted in significant differences in the composition of hydrate film and crystalline hydrate between the two experiments. Experiment 8 exhibited a higher abundance of hydrate film, while experiment 6 displayed a higher crystalline hydrate saturation. Consequently, there was very little difference in the total hydrate saturation. Furthermore, despite both experiments 9 and 10 having higher salinities (2 and 3wt%, respectively) compared to experiment 8, the crystalline hydrate saturation increases. This observation is probably due to their higher initial brine saturations (0.392 and 0.385, respectively). These findings indicate that initial water/brine saturation plays a crucial role in predicting the composition of hydrates within the porous media. Nevertheless, no crystalline hydrate formed within the first 3 hours when the salinity exceeded 3wt%, suggesting that the presence of salt at concentrations higher than 3wt% has an inhibiting and delaying effect on crystalline hydrate formation in the brine phase.

A similar trend was observed for the $CaCl_2$ experiments (Figure 5.20). The total hydrate saturation and the crystalline hydrate saturation decreases with increasing salinity. however, the hydrate saturations in these experiments showed larger variations compared to the NaCl experiments. For instance, experiment 16 (3wt% $CaCl_2$) exhibited unusual hydrate formation behavior compared to experiments of both lower and higher salinities. As for NaCl, no crystalline hydrate was observed when the salinity exceeded 3wt%. However, in contrast to the NaCl experiments, where significant amounts of crystalline hydrate was observed for salinities of 1-3wt%, experiments conducted with 2wt% and 3wt% $CaCl_2$ (experiment 15 and 16, respectively) exhibited almost negligible amounts of crystalline hydrate. Although this fact could be attributed to the low initial brine saturation (0.322 and 0.311, respectively), it could also be due to the inhibiting effect of salt.

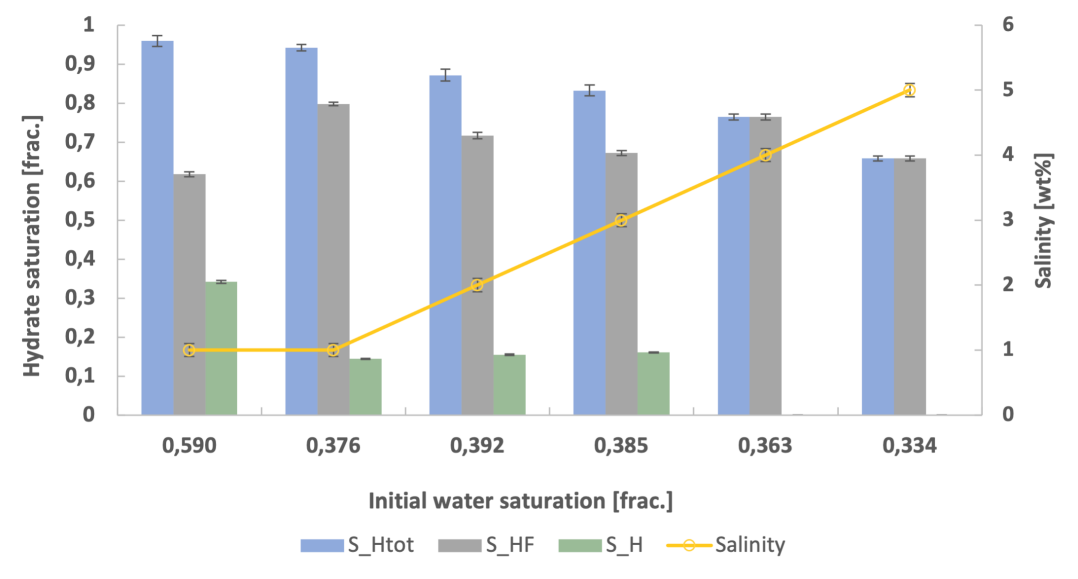

Figure 5.19: Experiments 6-12 with NaCl brine. Hydrate saturation is on the primary y-axis (left), while the salinity is on the secondary y-axis (right). The x-axis represents the initial water saturation of each experiment. The bars represent hydrate film, crystalline hydrate, and total hydrate saturation as a fraction of the pore volume.

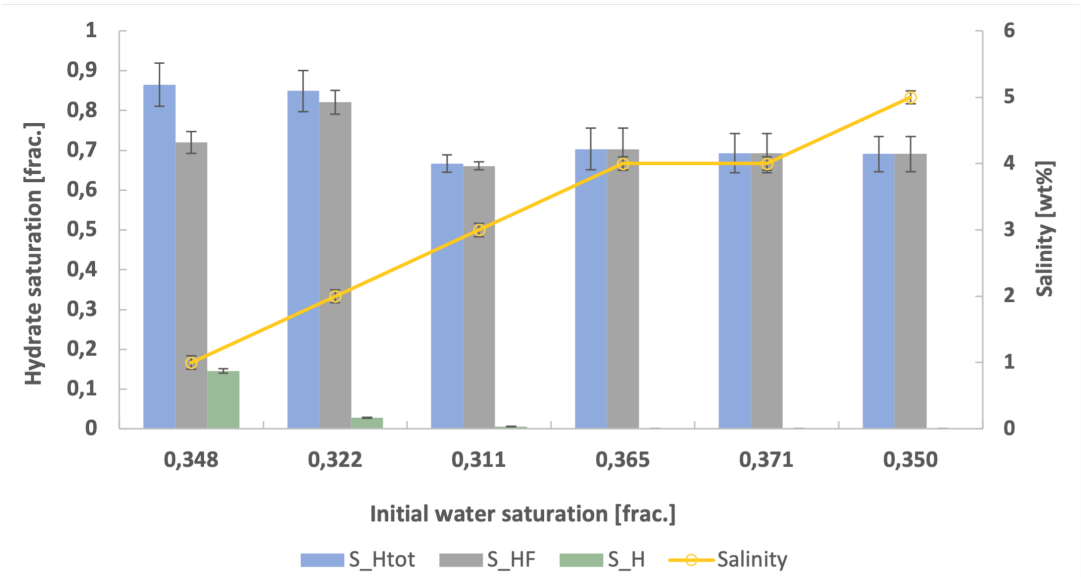

Figure 5.20: Experiments 6-12 with $CaCl_2$ brine. Hydrate saturation is on the primary y-axis (left), while the salinity is on the secondary y-axis (right). The x-axis represents the initial water saturation of each experiment. The bars represent hydrate film, crystalline hydrate, and total hydrate saturation as a fraction of the pore volume.

These findings coincide with the observations made in the qualitative section (section 5.1.6). The crystalline hydrate saturation is expected to decrease due to the inhibiting effect of salt, the desalination effect, and the salting out effect. As hydrates form in the CO_2 phase the salinity of the surrounding water increases, thereby inhibiting further hydrate formation. With an increase of salt concentration in the surrounding pore water the solubility of CO_2 will decrease, restricting the availability of CO_2 in the water phase. The formation of crystalline hydrates in the water phase will therefore be reliant on water film flow from neighbouring pores and the concentration gradient causing ion diffusion from areas with high salt concentration to low salt concentration. These processes are slow but over time, the local salt concentration will decrease, resulting in a delay in hydrate formation. This effect seems to be more pronounced for $CaCl_2$ where the crystalline hydrate saturation decreases with concentrations above 1wt%. In contrast, the crystalline hydrate saturation remains relatively constant for NaCl concentrations between 1-3wt% and decreases with salinities above 3wt%.

Similarly, Husebø et al. [61] concluded that when the initial salinity is higher than 4wt% NaCl, the salinity of residual water after hydrate formation was the limiting factor for further hydrate formation. Furthermore, the hydrate film saturation for the $CaCl_2$ decreased with increasing salinity. Additionally, less hydrate film transformed into non-porous crystalline hydrate when the salinity exceeded 3wt% $CaCl_2$. Indicating a larger amount of unconsumed CO_2 and less stable hydrate structure compared to NaCl experiments where almost all hydrate film transformed into crystalline hydrate. This indicates that, even at low concentrations, the effect of $CaCl_2$ is more pronounced compared to NaCl, further supporting the theory that $CaCl_2$ is a stronger thermodynamic inhibitor.

6. Conclusion

The formation mechanisms of CO_2 hydrates on pore scale were investigated both qualitatively and quantitatively utilizing a silicon micromodel. The effect of initial water saturation, temperature, and salinity was studied to investigate the potential of utilizing CO_2 hydrates as a sealing mechanism for geological CO_2 storage. This chapter presents key observations and is divided into three parts: hydrate formation mechanisms, the effect of intial water saturation and temperature, and the effect of salinity.

Hydrate formation mechanisms

- Hydrate formation resulted in two different configurations: (1) hydrate film encapsulating gas and (2) nonporous crystalline hydrate. The availability of water and was crucial in predicting formation of the latter.
- Hydrate film formation initiated at the curved water-CO_2 interface along the pore walls and the interface between large water droplets residing underneath the CO_2 phase. The hydrate front rapidly propagated into the continuous CO_2 phase until all water was consumed.
- With sufficient driving force (difference in pressure before and after agitation), the hydrate film formation was uniform within the field of view and no hydrate front was observed. The hydrate configuration displayed a pore-filling configuration and gradually transformed into solid crystalline hydrate.
- The formation of crystalline hydrate in the water phase was simultaneous to the hydrate film formation in the continuous CO_2 phase in smaller pores due to rapid mass transfer of CO_2 through the hydrate film. The formation of crystalline hydrate in larger pores and pores not in contact with the continuous CO_2 phase was slower indicating that hydrate formation from dissolved CO_2 and CO_2 mass transfer in the water phase are slower mechanisms.
- Low concentrations NaCl (1-3wt%) had a promotional effect on hydrate growth while high concentrations resulted in a more pronounced hydrate front and areas with unconsumed CO_2. Nevertheless, the hydrate film was pore-filling for all concentrations (1-5wt%) and eventually transformed into crystalline hydrate.
- The effect of salinity on hydrate formation was more pronounced for $CaCl_2$ brine compared to NaCl brine. While 1wt% $CaCl_2$ had a promotional effect on hydrate growth, higher concentrations had a delaying effect on hydrate formation. Furthermore the

hydrate front became more pronounced with increasing salinity and for high-salinity experiments the hydrate configuration did not exhibit pore-filling behavior.

The effect of initial water saturation and temperature

- There was a strong correlation between initial water saturation and crystalline hydrate growth. As water saturation increased, so did the crystalline hydrate saturation, while the hydrate film saturation appeared to remain relatively constant. Consequently, the total hydrate saturation increased.
- The hydrate film grew thicker in pores where water was readily available and continued to thicken until all water was consumed, indicating that hydrate film thickening is strongly dependent of initial water saturation. Initial water saturations above 0.33 was found to result in a pore-filling hydrate configuration. Pore-filling hydrates play a crucial role in the formation of a hydrate cap, effectively reducing fluid permeability and flow, thereby preventing upward migration of CO_2 and leakage to the atmosphere.
- There was a strong correlation between temperature and both crystalline and total hydrate saturation. With increasing temperature, the hydrate film saturation remained more or less the same, while the crystalline hydrate saturation decreased. Resulting in a overall decrease in total hydrate saturation. However, the correlation was not as strong as the correlation between initial water saturation and total hydrate saturation, suggesting that initial water saturation is the limiting factor.
- The induction time was observed to decrease with both increasing water saturation and decreasing temperature. While both correlations were strong, the correlation between temperature and induction time is likely stronger. However, due to the number of variables present it remains unclear whether is due to the sufficient subcooling or initial water saturation. Induction times can provide an indication of how quickly CO_2 can be trapped in a hydrate structure. Further research on induction times is therefore required to better understand the potential of utilizing CO_2 hydrates in carbon storage.
- Due to the number of variables present in this work it is challenging to draw definite conclusions from the data. Further investigation and controlled experiments are necessary to establish a clearer understanding of the effect of initial water saturation and temperature on hydrate formation.

The effect of salinity

- The hydrate film saturation remained constant as NaCl concentration increases, showing no clear correlation. However, the crystalline hydrate saturation decreases with higher salinity, and the correlation is strong. Consequently, the total hydrate saturation decreases, and there is a significant correlation between hydrate saturation and salinity. No crystalline hydrate formed when the salinity exceeded 3wt%. This suggests that the presence of salt at concentrations higher than 3wt% has an inhibiting effect on crystalline hydrate formation.
- The effect of salinity was more pronounced for $CaCl_2$ brine. Both hydrate film saturation and crystalline hydrate saturation decreased with increasing salinity. Resulting in an overall strong correlation between salininty and hydrate saturation. Negligible amounts of crystalline hydrate formed when the salinity exceeded 1wt%, supporting the theory that $CaCl_2$ is a stronger hydrate formation inhibitor.
- The crystalline hydrate saturation decreases with both increasing salinity and decreasing initial water saturation. The difference in initial water saturation for experiments conducted with the same salinity resulted in significant differences in the composition of hydrate film and crystalline hydrate. These findings indicate that initial water saturation plays a crucial role in predicting the composition of hydrates within the porous media.

Salinity and initial water saturation were identified as the key factors influencing hydrate formation and predicting hydrate composition in porous media. Initial water saturations above 0.33 was resulted in a pore-filling hydrate film composition and eventually a stable crystalline hydrate morphology. Pore-filling hydrates play a crucial role in the formation of a hydrate cap, effectively reducing fluid permeability and flow, thereby preventing upward migration of CO_2 and leakage to the atmosphere. Salinities exceeding 3wt% NaCl and 2wt% $CaCl_2$ delayed the hydrate formation in both the water phase and the continuous CO_2 phase resulting in longer induction times. Short induction times are preferred to effectively reduce fluid permeability and flow, thereby ensuring that CO_2 is quickly retained under the hydrate seal. These findings demonstrate the potential of utilizing CO_2 hydrates as a sealing mechanism for geological CO_2 storage in formations with water saturations of 0.33 and above, and preferred salt concentrations of approximately 3wt% or less.

7. Further work

The following section presents suggestions for further investigations of unanswered questions based on the findings of this master's thesis.

- Investigation of the effect of initial water saturation on hydrate formation under constant pressure and temperature with a more predictable agitation method, such as controlled pressure pulses.
- The effect of salinity on hydrate composition with constant initial water saturation with a more predictable agitation method, such as controlled pressure pulses.
- Investigation of the effect of initial water saturation on induction times under constant temperature conditions. And, investigation of the effect of temperature on induction times with constant initial water saturation.
- Quantification of the hydrate film growth and thickness by conducting micromodel experiments using a microscope with improved resolution.
- Further micromodel experiments should be conducted to examine fluid permeability and pore plugging with respect to induction time.

A. Experimental Equipment

This chapter provides a list of the equipment utilized in the experimental work.

- Aluminum dual cooling chamber
- Thermo Scientific Neslab RTE 17
- High pressure micromodel
- Refrigerated bath circulator
- Quizix SP-5200 pump system
- PEEK tubing
- OMEGA HH506RA Thermocouple
- Steel tubing
- Nikon D7100 camera
- Photonic LED F1 5500K light source

B. Experimental pressure during agitation

The experimental pressure during agitation is given in Table B.1. The table shows the pressure before, during, and right after the pressure drop during agitation of the system.

Table B.1: Experimental pressure data. B-A is the difference in pressure before agitation and during the pressure drop. A-A is the difference in pressure before and after agitation.

Experiment	Pressure before agitation [bar]	Pressure drop [bar]	Pressure after agitation [bar]	B-A dp [bar]	A-A dp [bar]
1	75.05	74.32	75.36	0.73	-1.04
2	75.01	70.91	76.24	4.1	-5.33
3	75.3	69.39	77.0	5.91	-7.61
5	75.02	74.3	75.3	0.72	-1.0
8	75.0	72.2	75.96	2.8	-3.76
9	75.03	74.3	75.38	0.73	-1.08
10	74.99	73.96	75.3	1.03	-1.34
11	74.98	73.74	75.9	1.24	-2.16
12	75.01	73.95	75.47	1.06	-1.52
13	74.97	68.24	76.36	6.73	-8.12
15	74.99	60.23	79.84	14.76	-19.61
16	75.03	64.97	77.5	10.06	-12.53
17	75.05	71.73	76.62	3.32	-4.89
17_2	75.06	69.75	77.43	5.31	-7.68
18	75.01	65.8	78.21	9.21	-12.41
19	75.03	74.02	75.48	1.01	-1.46
20	74.9	71.87	76.88	3.03	-5.01

7. Bibliography

[1] IPCC, "Summary for policymakers. in: Climate change 2021: The physical science basis. contribution of working group i to the sixth assessment report of the intergovernmental panel on climate change," In Press, 2021.

[2] "The paris agreement," pp. 4–18, 2016/10/19 2016. [Online]. Available: https://eur-lex.europa.eu/legal-content/EN/TXT/?uri=CELEX:22016A1019(01)

[3] UNFCCC, "Adoption of the paris agreement," 2015. [Online]. Available: https://unfccc.int/resource/docs/2015/cop21/eng/l09r01.pdf

[4] IPCC, "Summary for the policymakers," Cambridge University Press, Report, 2022.

[5] ——, "Climate change 2022: Mitigation of climate change," Cambridge University Press, Report, 2022. [Online]. Available: https://www.ipcc.ch/report/ar6/wg3/downloads/report/IPCC_AR6_WGIII_FullReport.pdf

[6] H. Ritchie, M. Roser, and P. Rosado, "Energy," *Our World in Data*, 2022. [Online]. Available: 'https://ourworldindata.org/energy

[7] U. Nations, "The 17 goals," 2015. [Online]. Available: https://sdgs.un.org/goals

[8] G. Mott, C. Razo, and R. Hamwey, "Carbon emissions anywhere threaten development everywhere," 2021. [Online]. Available: https://unctad.org/news/carbon-emissions-anywhere-threaten-development-everywhere

[9] S. Paltsev, J. Morris, H. Kheshgi, and H. Herzog, "Hard-to-abate sectors: The role of industrial carbon capture and storage (ccs) in emission mitigation," *Applied Energy*, vol. 300, p. 117322, 2021. [Online]. Available: https://www.sciencedirect.com/science/article/pii/S0306261921007327

[10] S. Bachu, "Sequestration of co2 in geological media: criteria and approach for site selection in response to climate change," *Energy Conversion and Management*, vol. 41, no. 9, pp. 953–970, 2000. [Online]. Available: https://www.sciencedirect.com/science/article/pii/S0196890499001491

[11] ——, "Sequestration of co2 in geological media: criteria and approach for site selection in response to climate change," *Energy Conversion and Management*, vol. 41, no. 9, pp. 953–970, 2000. [Online]. Available: https://www.sciencedirect.com/science/article/pii/S0196890499001491

[12] M. Jafari, S. C. Cao, and J. Jung, "Geological co2 sequestration in saline aquifers: Implication on potential solutions of china's power sector," *Resources, Conservation and Recycling*, vol. 121, pp. 137–155, 2017, environmental Challenges and Potential Solutions of China's Power Sector. [Online]. Available: https://www.sciencedirect.com/science/article/pii/S0921344916301240

[13] IPCC, *Carbon Dioxide Capture and Storage*, B. Metz, O. Davidson, H. de Coninck, M. Loos, and L. Meyer, Eds. Cambridge, UK: Cambridge University Press, 2005. [Online]. Available: https://www.ipcc.ch/report/co2-capture-and-storage/

[14] H. Koide, M. Takahashi, H. Tsukamoto, and Y. Shindo, "Self-trapping mechanisms of carbon dioxide in the aquifer disposal," *Energy Conversion and Management*, vol. 36, no. 6, pp. 505–508, 1995. [Online]. Available: https://www.sciencedirect.com/science/article/pii/019689049500054H

[15] J. Gauteplass, S. Almenningen, G. Ersland, and T. Barth, "Hydrate seal formation during laboratory co2 injection in a cold aquifer," *International Journal of Greenhouse Gas Control*, vol. 78, pp. 21–26, 2018. [Online]. Available: https://www.sciencedirect.com/science/article/pii/S1750583617310393

[16] J. Gauteplass, S. Almenningen, G. Ersland, T. Barth, J. Yang, and A. Chapoy, "Multiscale investigation of co2 hydrate self-sealing potential for carbon geo-sequestration," *Chemical Engineering Journal*, vol. 381, p. 122646, 2020. [Online]. Available: https://www.sciencedirect.com/science/article/pii/S1385894719320492

[17] "Carbon cycle diagram," [Photograph], n.d., retrieved from Encyclopædia Britannica ImageQuest. [Online]. Available: https://quest.eb.com/search/132_1428008/1/132_1428008/cite

[18] P. Freund, S. Bachu, D. Simbeck, K. Thambimuthu, and M. Gupta, "Annex i: Properties of co2 and carbon-based fuels," in *Carbon dioxide capture and storage*, B. Metz, O. Davidson, H. de Coninck, M. Loos, and L. Meyer, Eds. Cambridge, UK: Cambridge University Press, 2005, pp. 431–456.

[19] A. Witkowski, M. Majkut, and S. Rulik, "Analysis of pipeline transportation systems for carbon dioxide sequestration," *Archives of Thermodynamics*, vol. 35, pp. s. 117–140, 03 2014.

[20] C. A. Rochelle, A. P. Camps, D. Long, A. Milodowski, K. Bateman, D. Gunn, P. Jackson, M. A. Lovell, and J. Rees, "Can co₂ hydrate assist

in the underground storage of carbon dioxide?" *Geological Society, London, Special Publications*, vol. 319, no. 1, pp. 171–183, 2009. [Online]. Available: https://www.lyellcollection.org/doi/abs/10.1144/SP319.14

[21] J. Zheng, Z. R. Chong, M. F. Qureshi, and P. Linga, "Carbon dioxide sequestration via gas hydrates: A potential pathway toward decarbonization," *Energy & Fuels*, vol. 34, no. 9, pp. 10 529–10 546, 2020. [Online]. Available: https://doi.org/10.1021/acs.energyfuels.0c02309

[22] H. Davy, "On a combination of oxymuriatic gas and oxygene gas," *Philosophical Transactions of the Royal Society*, vol. 101, p. 162, 1811.

[23] E. D. Sloan, *Clathrate hydrates of natural gases*, 3rd ed., ser. Chemical industries. Boca Raton, Fla: CRC Press, 2008, vol. 119.

[24] P. Villard, "Sur quelques nouveaux hydrates de gaz," *Compt. rend*, p. 395, 1888.

[25] E. G. Hammerschmidt, "Formation of gas hydrates in natural gas transmission lines," *Industrial and Engineering Chemistry*, vol. 26, no. 8, pp. 851–855, 1934, doi: 10.1021/ie50296a010. [Online]. Available: https://doi.org/10.1021/ie50296a010

[26] G. Jeffrey and R. McMullan, *The Clathrate Hydrates*. John Wiley Sons, Inc., 2007, vol. 8, pp. 43–108.

[27] J. A. Ripmeester, J. S. Tse, C. I. Ratcliffe, and B. M. Powell, "A new clathrate hydrate structure," *Nature*, vol. 325, no. 6100, pp. 135–136, 1987. [Online]. Available: https://doi.org/10.1038/325135a0

[28] Y. F. Makogon, "A gas hydrate formation in the gas saturated layers under low temperature," *Gas Industry*, vol. 5, pp. 14–15, 1965.

[29] Y. Makogon, "Peculiarities a gas-field development in permafrost," *Nedra, Moscow*, pp. 1–17, 1966.

[30] I. G. Union, "Global gas markets supporting growth and sustainability," 2016. [Online]. Available: https://www.igu.org/resources/global-gas-markets-supporting-growth-and-sustainability/

[31] Y. F. Makogon, S. A. Holditch, and T. Y. Makogon, "Natural gas-hydrates — a potential energy source for the 21st century," *Journal of Petroleum Science and Engineering*, vol. 56, no. 1, pp. 14–31, 2007. [Online]. Available: https://www.sciencedirect.com/science/article/pii/S0920410506001859

[32] K. A. Kvenvolden, "Methane hydrates and global climate," *Global Biogeochemical Cycles*, vol. 2, no. 3, pp. 221–229, 1988, https://doi.org/10.1029/GB002i003p00221. [Online]. Available: https://doi.org/10.1029/GB002i003p00221

[33] E. Piñero, M. Marquardt, C. Hensen, M. Haeckel, and K. Wallmann, "Estimation of the global inventory of methane hydrates in marine sediments using transfer functions," *Biogeosciences Discussions*, vol. 9, 2012.

[34] D. Schoderbek, H. Farrell, K. Hester, J. Howard, K. Raterman, S. Silpngarmlert, K. L. Martin, B. Smith, and P. Klein, "Conocophillips gas hydrate production test final technical report," *United States Department of Energy*, vol. 204, 2013.

[35] S. Circone, L. A. Stern, S. H. Kirby, W. B. Durham, B. C. Chakoumakos, C. J. Rawn, A. J. Rondinone, and Y. Ishii, "Co2 hydrate: Synthesis, composition, structure, dissociation behavior, and a comparison to structure i ch4 hydrate," *The Journal of Physical Chemistry B*, vol. 107, no. 23, pp. 5529–5539, 2003. [Online]. Available: https://doi.org/10.1021/jp027391j

[36] C. A. Koh and E. D. Sloan, "Natural gas hydrates: Recent advances and challenges in energy and environmental applications," *AIChE Journal*, vol. 53, no. 7, pp. 1636–1643, 2007. [Online]. Available: https://aiche.onlinelibrary.wiley.com/doi/abs/10.1002/aic.11219

[37] N. Kolesnikov and E. Borisenko, *Modern Aspects of Bulk Crystal and Thin Film Preparation*. Rijeka: IntechOpen, Jan 2012. [Online]. Available: https://doi.org/10.5772/1348

[38] R. L. Christiansen and E. D. Sloan, Jr, "A compact model for hydrate formation," 11 1995. [Online]. Available: https://www.osti.gov/biblio/124617

[39] W. A. Tiller, *The Science of Crystallization: Microscopic Interfacial Phenomena*, 1st ed. Cambridge, England: Cambridge University Press, 1991, hardcover £40.00, Paperback £15.00.

[40] J. W. Cahn, W. Hillig, and G. Sears, "The molecular mechanism of solidification," *Acta Metallurgica*, vol. 12, no. 12, pp. 1421–1439, 1964. [Online]. Available: https://www.sciencedirect.com/science/article/pii/0001616064901300

[41] E. M. Freer, M. Sami Selim, and E. Dendy Sloan, "Methane hydrate film growth kinetics," *Fluid Phase Equilibria*, vol. 185, no. 1, pp. 65–75, 2001,

proceedings of the 14th symposium on thermophysical properties. [Online]. Available: https://www.sciencedirect.com/science/article/pii/S0378381201004575

[42] E. Sloan, "Fundamental principles and applications of natural gas hydrates," *Nature*, vol. 426, no. 6964, pp. 353–359, 2003.

[43] C. J. Taylor, K. T. Miller, C. A. Koh, and E. D. Sloan, "Macroscopic investigation of hydrate film growth at the hydrocarbon/water interface," *Chemical Engineering Science*, vol. 62, no. 23, pp. 6524–6533, 2007. [Online]. Available: https://www.sciencedirect.com/science/article/pii/S0009250907005428

[44] D. K. Staykova, W. F. Kuhs, A. N. Salamatin, and T. Hansen, "Formation of porous gas hydrates from ice powders: Diffraction experiments and multistage model," *The Journal of Physical Chemistry B*, vol. 107, no. 37, pp. 10 299–10 311, 2003. [Online]. Available: https://doi.org/10.1021/jp027787v

[45] P. Servio and P. Englezos, "Morphology of methane and carbon dioxide hydrates formed from water droplets," *AIChE Journal*, vol. 49, pp. 269 – 276, 01 2003.

[46] R. Ohmura, S. Matsuda, T. Uchida, T. Ebinuma, and H. Narita, "Clathrate hydrate crystal growth in liquid water saturated with a guest substance: Observations in a methane + water system," *Crystal Growth & Design*, vol. 5, no. 3, pp. 953–957, 2005. [Online]. Available: https://doi.org/10.1021/cg049675u

[47] D. Katsuki, R. Ohmura, T. Ebinuma, and H. Narita, "Methane hydrate crystal growth in a porous medium filled with methane-saturated liquid water," *Philosophical Magazine*, vol. 87, no. 7, pp. 1057–1069, 2007. [Online]. Available: https://doi.org/10.1080/14786430601021652

[48] W. Renpu, "Chapter 1 - basis of well completion engineering," in *Advanced Well Completion Engineering (Third Edition)*, 3rd ed., W. Renpu, Ed. Gulf Professional Publishing, 2011, pp. 1–74. [Online]. Available: https://www.sciencedirect.com/science/article/pii/B9780123858689000014

[49] M. M. Falahieh, M. Bonyadi, and A. Lashanizadegan, "Effect of different salts on the kinetic parameters of the carbon dioxide hydrate formation," *Journal of Natural Gas Science and Engineering*, vol. 100, p. 104461, 2022. [Online]. Available: https://www.sciencedirect.com/science/article/pii/S187551002200052X

[50] M. Karamoddin and F. Varaminian, "Performance of hydrate inhibitors in tetrahydrofuran hydrate formation by using measurement of electrical conductivity," *Journal of Industrial and Engineering Chemistry*, vol. 20, no. 5, pp. 3815–3820, 2014. [Online]. Available: https://www.sciencedirect.com/science/article/pii/S1226086X13007168

[51] Q. Lv, X. Zang, X. Li, and G. Li, "Effect of seawater ions on cyclopentane-methane hydrate phase equilibrium," *Fluid Phase Equilibria*, vol. 458, pp. 272–277, 2018. [Online]. Available: https://www.sciencedirect.com/science/article/pii/S0378381217304697

[52] S. Mahdavi, "Parameters affecting the wettability of glass medium in the presence of co2; a critical review," *Journal of Molecular Liquids*, vol. 333, p. 115943, 2021. [Online]. Available: https://www.sciencedirect.com/science/article/pii/S016773222100670X

[53] S. Almenningen, E. Iden, M. Fernø, and G. Ersland, "Salinity effects on pore-scale methane gas hydrate dissociation," *Journal of Geophysical Research: Solid Earth*, vol. 123, 2018.

[54] B. Tohidi, R. Anderson, M. B. Clennell, R. W. Burgass, and A. B. Biderkab, "Visual observation of gas-hydrate formation and dissociation in synthetic porous media by means of glass micromodels," *Geology*, vol. 29, no. 9, pp. 867–870, 09 2001. [Online]. Available: https://doi.org/10.1130/0091-7613(2001)029<0867:VOOGHF>2.0.CO;2

[55] B. Tohidi, J. Yang, M. Salehabadi, R. Anderson, and A. Chapoy, "Co2 hydrates could provide secondary safety factor in subsurface sequestration of co2," *Environmental Science & Technology*, vol. 44, no. 4, pp. 1509–1514, 2010, pMID: 20085250. [Online]. Available: https://doi.org/10.1021/es902450j

[56] S. Almenningen, J. Gauteplass, P. Fotland, G. L. Aastveit, T. Barth, and G. Ersland, "Visualization of hydrate formation during co2 storage in water-saturated sandstone," *International Journal of Greenhouse Gas Control*, vol. 79, pp. 272–278, 2018. [Online]. Available: https://www.sciencedirect.com/science/article/pii/S1750583618304729

[57] L. P. Hauge, J. Gauteplass, M. D. Høyland, G. Ersland, A. Kovscek, and M. A. Fernø, "Pore-level hydrate formation mechanisms using realistic rock structures in high-pressure silicon micromodels," *International Journal of Greenhouse Gas Control*, vol. 53, pp. 178–186, 2016. [Online]. Available: https://www.sciencedirect.com/science/article/pii/S1750583616303103

[58] D. Katsuki, R. Ohmura, T. Ebinuma, and H. Narita, "Formation, growth and ageing of clathrate hydrate crystals in a porous medium," *Philosophical Magazine*, vol. 86, no. 12, pp. 1753–1761, 2006. [Online]. Available: https://doi.org/10.1080/14786430500509062

[59] T. Uchida, T. Ebinuma, J. Kawabata, and H. Narita, "Microscopic observations of formation processes of clathrate-hydrate films at an interface between water and carbon dioxide," *Journal of Crystal Growth*, vol. 204, no. 3, pp. 348–356, Jul. 1999.

[60] T. Uchida, I. Y. Ikeda, S. Takeya, T. Ebinuma, J. Nagao, and H. Narita, "Co2 hydrate film formation at the boundary between co2 and water: effects of temperature, pressure and additives on the formation rate," *Journal of Crystal Growth*, vol. 237-239, pp. 383–387, 2002, the thirteenth international conference on Crystal Growth in conj unction with the eleventh international conference on Vapor Growth and Epitaxy. [Online]. Available: https://www.sciencedirect.com/science/article/pii/S002202480101822X

[61] J. Husebø, G. Ersland, A. Graue, and B. Kvamme, "Effects of salinity on hydrate stability and implications for storage of co2 in natural gas hydrate reservoirs," *Energy Procedia*, vol. 1, no. 1, pp. 3731–3738, 2009, greenhouse Gas Control Technologies 9. [Online]. Available: https://www.sciencedirect.com/science/article/pii/S1876610209008157

[62] C. Holzammer, A. Finckenstein, S. Will, and A. S. Braeuer, "How sodium chloride salt inhibits the formation of co2 gas hydrates," *The Journal of Physical Chemistry B*, vol. 120, no. 9, pp. 2452–2459, 2016, pMID: 26867107. [Online]. Available: https://doi.org/10.1021/acs.jpcb.5b12487

[63] M. Buchgraber, M. Al-Dossary, C. M. Ross, and A. R. Kovscek, "Creation of a dual-porosity micromodel for pore-level visualization of multiphase flow," *Journal of Petroleum Science and Engineering*, vol. 86-87, pp. 27–38, 2012. [Online]. Available: https://www.sciencedirect.com/science/article/pii/S0920410512000654

[64] B. Benali, T. L. Føyen, Z. P. Alcorn, M. Haugen, J. Gauteplass, A. R. Kovscek, and M. A. Fernø, "Pore-scale bubble population dynamics of co2-foam at reservoir pressure," *International Journal of Greenhouse Gas Control*, vol. 114, p. 103607, 2022. [Online]. Available: https://www.sciencedirect.com/science/article/pii/S1750583622000263

[65] Engineering ToolBox, "Refractive Index common Liquids, Solids and Gases," https://www.engineeringtoolbox.com/refractive-index-d_1264.html, 2008, [Accessed: 28. march 2023].

[66] J. Guo, P. André, M. Adam, S. Panyukov, M. Rubinstein, and J. M. DeSimone, "Solution properties of a fluorinated alkyl methacrylate polymer in carbon dioxide," *Macromolecules*, vol. 39, no. 9, pp. 3427–3434, 2006. [Online]. Available: https://doi.org/10.1021/ma052409k

[67] M. Bylov and P. Rasmussen, "Experimental determination of refractive index of gas hydrates," *Chemical Engineering Science*, vol. 52, no. 19, pp. 3295–3301, 1997. [Online]. Available: https://www.sciencedirect.com/science/article/pii/S0009250997001449

[68] J. S. Pandey, Ørjan Strand, N. von Solms, G. Ersland, and S. Almenningen, "Direct visualization of ch4/co2 hydrate phase transitions in sandstone pores," *Crystal Growth and Design*, vol. XXXX, 04 2021.

[69] B. Kvamme, A. Graue, T. Buanes, T. Kuznetsova, and G. Ersland, "Storage of co2 in natural gas hydrate reservoirs and the effect of hydrate as an extra sealing in cold aquifers," *International Journal of Greenhouse Gas Control*, vol. 1, no. 2, pp. 236–246, 2007, 8th International Conference on Greenhouse Gas Control Technologies. [Online]. Available: https://www.sciencedirect.com/science/article/pii/S1750583606000028

[70] H. Teng, A. Yamasaki, M.-K. Chun, and H. Lee, "Solubility of liquid co2in water at temperatures from 278 k to 293 k and pressures from 6.44 mpa to 29.49 mpa and densities of the corresponding aqueous solutions," *The Journal of Chemical Thermodynamics*, vol. 29, no. 11, pp. 1301–1310, 1997. [Online]. Available: https://www.sciencedirect.com/science/article/pii/S0021961497902494

[71] S. Almenningen, M. Lysyy, and G. Ersland, "Quantification of ch4 hydrate film growth rates in micromodel pores," *Crystal Growth & Design*, vol. 21, no. 7, pp. 4090–4099, 2021. [Online]. Available: https://doi.org/10.1021/acs.cgd.1c00396

[72] "Gases solubility in water," https://www.engineeringtoolbox.com/gases-solubility-water-d_1148.html, accessed: [21/06/23].

[73] S. Almenningen, M. Lysyy, and G. Ersland, "Quantification of ch4 hydrate film growth rates in micromodel pores," *Crystal Growth & Design*, vol. 21, no. 7, pp. 4090–4099, 2021. [Online]. Available: https://doi.org/10.1021/acs.cgd.1c00396

[74] P. C. Lund, Y. Shindo, Y. Fujioka, and H. Komiyama, "Study of the pseudo-steady-state kinetics of co2 hydrate formation and stability," *International Journal of Chemical Kinetics*, vol. 26, no. 2, pp. 289–297, 1994. [Online]. Available: https://onlinelibrary.wiley.com/doi/abs/10.1002/kin.550260207

[75] P. Mekala, M. Busch, D. Mech, R. S. Patel, and J. S. Sangwai, "Effect of silica sand size on the formation kinetics of co2 hydrate in porous media in the presence of pure water and seawater relevant for co2 sequestration," *Journal of Petroleum Science and Engineering*, vol. 122, pp. 1–9, 2014. [Online]. Available: https://www.sciencedirect.com/science/article/pii/S0920410514002666

[76] G. Ersland, J. Husebø, A. Graue, and B. Kvamme, "Transport and storage of co2 in natural gas hydrate reservoirs," *Energy Procedia*, vol. 1, no. 1, pp. 3477–3484, 2009, greenhouse Gas Control Technologies 9. [Online]. Available: https://www.sciencedirect.com/science/article/pii/S1876610209007826

[77] G. Zhao, M. Yang, W. Pang, G. Gong, J. nan Zheng, P. Zhang, and B. Chen, "Effects of hydrate cap on leakage prevention and capacity improvement of sub-seabed co2 sequestration," *Chemical Engineering Journal*, vol. 450, p. 138493, 2022. [Online]. Available: https://www.sciencedirect.com/science/article/pii/S1385894722039742

[78] S. Wang, M. Yang, W. Liu, J. Zhao, and Y. Song, "Investigation on the induction time of methane hydrate formation in porous media under quiescent conditions," *Journal of Petroleum Science and Engineering*, vol. 145, pp. 565–572, 2016. [Online]. Available: https://www.sciencedirect.com/science/article/pii/S0920410516302212